HOKKAIDO UNIVERSITY

Title	Study on Microcrystals and Ceramics of Ferroelectric BaTaO2N Oxynitride Perovskite
Author(s)	,
Citation	. ( ) 14024
Issue Date	2020-03-25
DOI	10.14943/doctoral.k14024
Doc URL	http://hdl.handle.net/2115/78317
Type	theses (doctoral)
File Information	Akira_HOSONO.pdf

Instructions for use

Study on Microcrystals and Ceramics of Ferroelectric BaTaO$_2$N Oxynitride Perovskite

ペロブスカイト型酸窒化物強誘電体

BaTaO$_2$N の微結晶と焼結体に関する研究

Akira Hosono

細野 新

HOKKAIDO
UNIVERSITY

A thesis submitted in partial fulfillment of
the requirements for the degree of
Doctor of Philosophy in Engineering

Hokkaido University
March 2020

Study on Microcrystals and Ceramics of

Ferroelectric BaTaO$_2$N Oxynitride Perovskite

By

Akira Hosono

Hokkaido University

2020

Doctoral Supervisor: Professor Yuji Masubuchi

Abstract

The compounds consisted of metals, oxygen, and nitrogen are called "metal oxynitrides (hereafter oxynitrides)". Oxynitrides have attracted considerable attention of scientists and industry for their excellent mechanical, optical, electrical, and catalytic properties. To date, the variety of oxynitrides increased to about 1000 thanks for the development of synthetic technics. Most of them were studied from the respects of crystallography, photoluminescence property, catalytic property, and computational approaches. This is because of the difficulty in the fabrication of single crystals and fully-densified ceramics of oxynitrides for the studies of the properties of electricity, mechanical strength, heat conductivity, and so on.

The target material of the present thesis is a perovskite-type oxynitride $BaTaO_2N$, which have been a subject of interest for its possible ferroelectricity induced by a local symmetry breaking due to its anisotropic anion ordering over centrosymmetric average structure. Sintering and microcrystal preparation of $BaTaO_2N$ were studied in this research to elucidate the emergence of ferroelectric polar phase alternation.

The present thesis is consisted of eight chapters. In **Chapter 1**, basic theories of dielectricity, sintering, crystal growth, and history of the researches of oxynitride materials are reviewed.

In **Chapter 2**, secondary harmonic generation was observed on $BaTaO_2N$ powder, which strongly supports the presence of non-centrosymmetric regions. Crystal structure of $BaTaO_2N$ was reinvestigated by Rietveld fitting of powder X-ray and neutron diffraction data using both models of non-centrosymmetric and centrosymmetric structure. The fitting results suggested the formation of tiny asymmetric domains dispersed over centrosymmetric average structure.

In **Chapter 3**, detail of thermal decomposition behavior and sinterability of $BaTaO_2N$ were studied. $BaTaO_2N$ partially released its nitrogen to be semiconducting $BaTaO_2N_{0.85}$ during high temperature sintering, similarly to $SrTaO_2N$. Its nitrogen content was recovered by post-ammonolysis of $BaTaO_2N_{0.85}$ ceramics. Relative dielectric constant of 620 was observed in the fully-annealed ceramics with relative density of 73.0% and piezoresponse signals were obtained for furtherly densified ceramic surface, although a serious current leakage occurred at the electrical voltage lower than ± 10 V.

In **Chapter 4**, thermal properties of alkaline-earth metal carbodiimides were studied in pursuit of the flux for the sintering and crystal growth of oxynitride perovskites. The melting behavior and thermal stability are discussed on a series of alkaline-earth metal carbodiimides from the views of experimental and computational approaches. $CaCN_2$, alpha-phase of $SrCN_2$, and tetragonal phase of $BaCN_2$ have their respective

melting points of 1340, 1020, and 910 °C. Only the melt of $BaCN_2$ could be maintained below its decomposition temperature of 912 °C estimated by density functional theory. This result indicated that $BaCN_2$ is a promising flux for oxynitride compounds. Afterwards $Sr_{1-x}Ba_xTaO_2N$ ceramics with relative density of about 70% was fabricated using a $BaCN_2$ additive at approximately 900 °C, which is below the decomposition temperature of $SrTaO_2N$. Microcrystal growth of A-site substituted solid solution $Sr_{1-x}Ba_xTaO_2N$ was discovered in the samples after cooling. The crystals contained a compositional gradation from Sr-rich interior to Ba-rich exterior regions. These results proved the occurrence of diffusion involving dissolution and recrystallization of oxynitrides via $BaCN_2$ flux.

In **Chapter 5**, reddish cubic microcrystals of $BaTaO_2N$ in size up to 3.1 μm were grown in a $BaCN_2$ flux. Crystalline phase identification and microstructure observation on the products disclosed that Ba-rich Ruddlesden-Popper type layered perovskites such as Ba_2TaO_3N were formed on a thin surface of $BaTaO_2N$ crystals. That is, $BaTaO_2N$ may not simply recrystallize from $BaCN_2$ solution.

In **Chapter 6**, ferroelectric properties of the $BaTaO_2N$ crystals were characterized. Piezoelectricity of micron-sized $BaTaO_2N$ crystals fabricated in **Chapter 5** was studied with a piezoresponse force microscope (PFM). Clear phase alternation of

spontaneous polarization by applied AC electrical field was observed at 120 °C and electrical voltage of 90 V. This is the first-ever evidence of the presence of ferroelectricity observed with oxynitride single crystals. Polarization direction was switched more easily at high temperature, which is a prominent characteristic of ferroelectrics.

In **Chapter 7**, liquid phase sintering of $BaTaO_2N$ with a $BaCN_2$ additive was tried using a spark plasma sintering (SPS) equipment to apply high mechanical pressure. Dissolution and precipitation of $BaTaO_2N$ via $BaCN_2$ flux, their chemical reactions at grain surface and boundaries, and uniaxial pressure of several tens of mega pascal assisted the rapid densification of $BaTaO_2N$ powder at approximately 900 °C. This procedure enabled to obtain $BaTaO_2N$ ceramics without nitrogen loss. Microstructure as well as electrical properties of the ceramic products were investigated.

In **Chapter 8**, comprehensive explanation on the crystal structure, flux growth, and ferroelectricity of perovskite-type $BaTaO_2N$ is given. Further suggestions targeting the application of oxynitride materials in the forms of ceramics and single crystals are mentioned in the last part as future perspectives.

Table of Contents

VI

Chapter 1

Perspective of Dielectric Oxynitride Perovskites

1-1. Overview of perovskite-type oxide dielectric materials

The most widely utilized inorganic materials are composed of metals and oxygen, which are metal oxides (hereafter oxides). One hot topic of their applications is electronic devices including capacitor, actuator, semiconductor, and so on. The developments of smaller size and higher device performances have been achieved in accordance with the increasing demands of higher device population on integrated circuits. Here, oxides with perovskite-type crystal structure are focused for their important electrical properties.

1-1-1. Perovskite-type structure

Ternary metal oxides named perovskite-type oxides are expressed with a chemical formula of ABO_3 where A and B are large cations like alkaline-earth or rare earth metals and smaller cations like transition metals, respectively. Their respective coordination numbers of A and B sites are twelve and six. Its crystal structure is illustrated in **Fig. 1-1**. In an ideal cubic oxide perovskite, the bond lengths (r_{A-O} and r_{B-O}) are related by the following equation;

$$\sqrt{2}r_{A-O} = 2r_{B-O} \qquad\qquad\qquad (1\text{-}1)$$

To discuss the structural deviations from ideal perovskite-type structure, a parameter called tolerance factor (t) shown in equation (1-2) is frequently used. [1]

$$t = \frac{\sqrt{2}r_{A-O}}{2r_{B-O}} \qquad\qquad\qquad (1\text{-}2)$$

The structural distortion in perovskite-type structure is usually related to the cation size. And in most cases, the t values are in the range of 0.85 – 1.05. The structure with the t value of nearly 1 means that it is stress-free and stable structure for the ideal matching of the radius balance of cation size. As the value of t deviates from 1, the structure becomes less stable due to a compressive stress and distortion by the cation size mismatch in crystalline lattices. [1] Cubic phase is maintained in the range of $0.90 < t < 1.0$ and for $t > 1.0$, the structure distorts but it is still basically a perovskite as in the case of tetragonal BaTiO$_3$ ($t = 1.06$). For smaller tolerance factors, $0.85 < t < 0.90$, the small A cation causes several different kinds of structural distortion. These distortions generally involve tilting or rotation of BO$_6$ octahedra and they sometimes cause the ferroelectricity in perovskite-type oxides.

1-1-2. Oxide dielectric materials

Dielectric materials (dielectrics) is a term that indicates electrical insulators.

They do not allow to pass the direct electrical current by the applied voltage, but each ion show some displacement from their statistical positions to form dielectric polarization. When external electrical field is applied to a dielectric material, cations displace towards the direction of the field and anions with negative charges shift to the opposite direction. Such polarization is a target of various applications for capacitors, actuators, wavelength filters, and so on. Dielectrics are divided into several categories depending on their properties as illustrated in **Fig. 1-2**.

The performances of dielectrics are evaluated with several kinds of parameters. The most important factors are relative dielectric constant (ε_r) and dielectric loss (tanδ), which mean the scale of polarization and electrical energy loss, respectively. These parameters express their potential for the application as capacitors. The performance of capacitors is described as their ability to hold the electrical energy (electrical charge Q) in the products as a function of the capacitance (C) and applied voltage (V). These parameters are related each other by the following equation. [1]

$$Q = CV \qquad\qquad (1\text{-}3)$$

The capacitance of vacuum is defined as the following function of geometrical factors

$$C_0 = \varepsilon_0 \frac{A}{d} \qquad\qquad (1\text{-}4)$$

where ε_0 is the dielectric constant of vacuum (8.854×10^{-12} F/m), A is the area of

electrodes, and d is the thickness of monolayer capacitor sample. The intrinsic

capacitance value of the dielectric sample is defined by the following equation. [1]

$$C = C_0 \frac{\varepsilon}{\varepsilon_0} = C_0 \varepsilon_r \qquad (1\text{-}5)$$

ε_r is called relative dielectric constant, which is unique to the compound. Another

parameter, dielectric loss ($\tan\delta$) is the proportion of the imaginary part (ε'') and the real

part (ε') of dielectric constants.

$$\varepsilon = \varepsilon' - i\varepsilon'' \qquad (1\text{-}6)$$

$$\tan\delta = \frac{\varepsilon''}{\varepsilon'} \qquad (1\text{-}7)$$

Smaller value of $\tan\delta$ is favorable because it exhibits the scale of energy loss mainly due

to the presence of electrically conductive nature.

1-1-3. Ferroelectricity

Among dielectrics, specific materials that can reorient their spontaneous

polarization direction by external electrical field are called ferroelectrics. Ferroelectrics

are industrially important for their applications such as ferroelectric random access

memories (FeRAM, $PbZr_{1-x}Ti_xO_3$ (PZT), $SrBi_2Ta_2O_9$ (SBT), $BiFeO_3$), capacitors ($BaTiO_3$,

PZT, $LiNbO_3$), ignition switches (PZT), and surface acoustic wave filters (SAW filters,

$LiTaO_3$). They need to have a crystallographic characteristic; non-centrosymmetric

structure with spontaneous polarization. A classical example, $BaTiO_3$ belongs to a space group of *P4mm* at room temperature and it has tetragonal symmetry with spontaneous polarization along *c*-axis at room temperature as shown in **Fig. 1-3(a)**. However, its spontaneous polarization disappears at its phase transition of 120 °C to form centrosymmetric $Pm\overline{3}m$ cubic phase (**Fig. 1-4(b)**). [1] Its dielectric constants against temperature (**Fig. 1-5**) reflect this phenomenon, which is called ferroelectric phase transition. This structural characteristic is sometimes undesirable from the view point of application because of a serious change of device performance caused by temperature. Moreover, lead-free dielectric materials are desired for the concerns of environmental pollutions after their disposals.
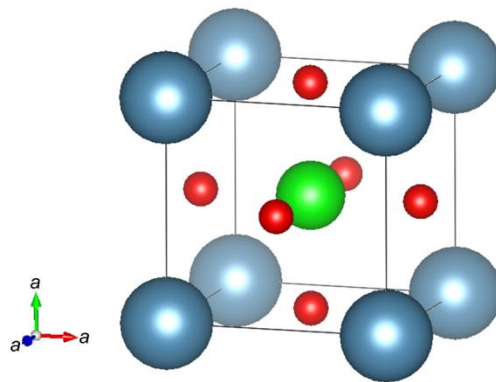
Fig. 1-1. Crystal structure model of cubic perovskite ABO_3. The blue, green, and red balls are *A*, *B*, and O, respectively. This image was drawn by the crystallographic imaging software VESTA. [3]
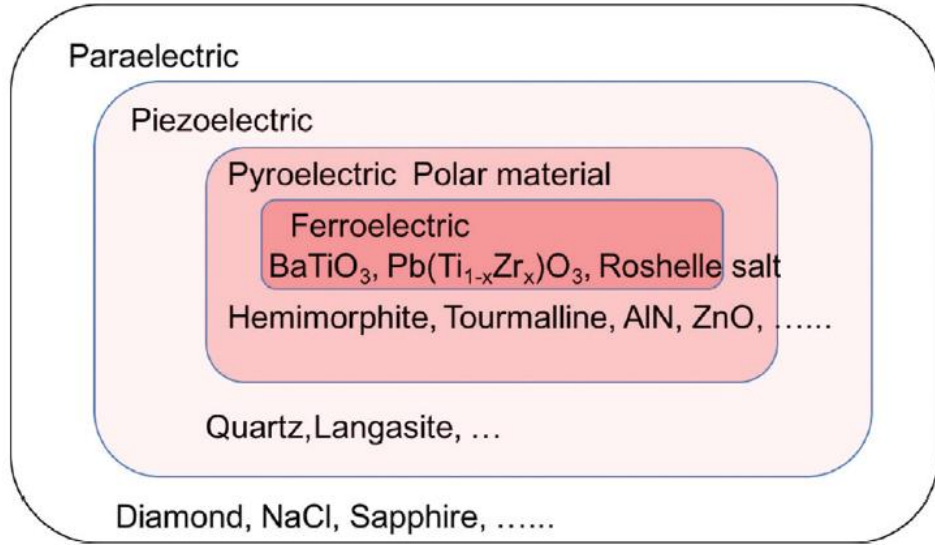
Fig. 1-2. Classification of the materials in insulators. [2]
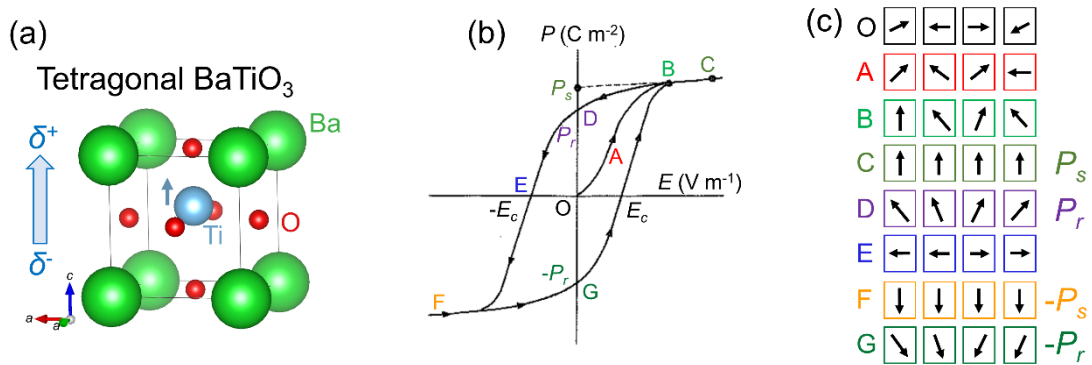
Fig. 1-3. (a) Crystal structure of tetragonal $BaTiO_3$, **(b)** polarization (P)-electrical field (E) hysteresis loop of ferroelectrics, and **(c)** a schematic image of polar directions of the domains. [1] P_s and P_r are saturated and remnant polarization, respectively. The crystal structure model was drawn by the crystallographic imaging software VESTA. [3]

6
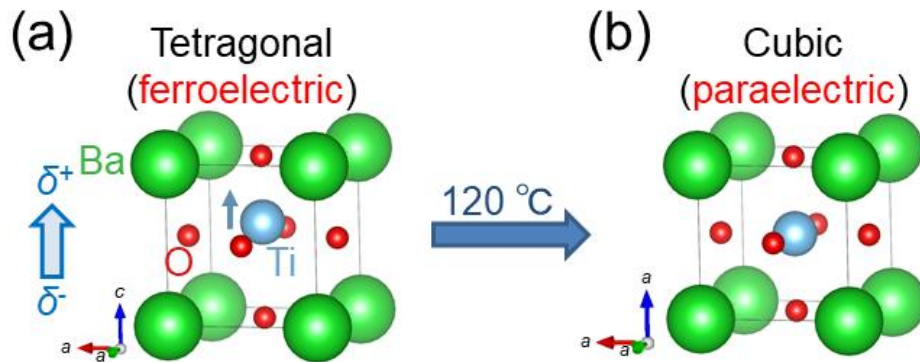
Fig. 1-4. Transformation of BaTiO₃ from **(a)** tetragonal to **(b)** cubic phase. [1] These crystal structure models were drawn by the crystallographic imaging software VESTA. [3]
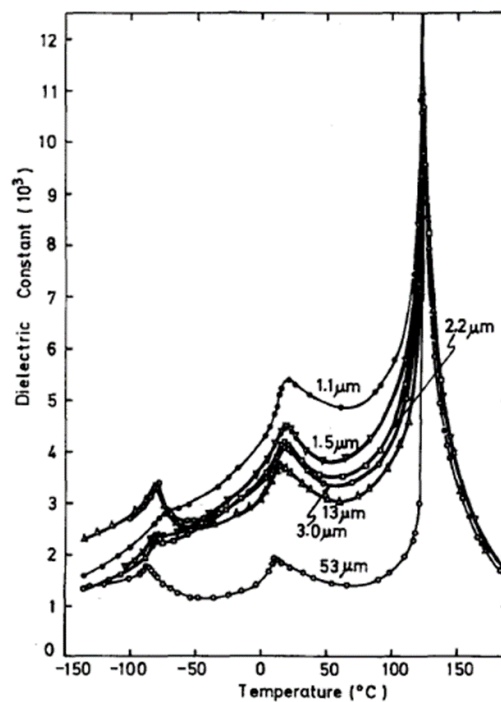
Fig. 1-5. Dielectric constants of BaTiO₃ ceramics against temperature. [4] The insets are grain size of ceramics.

1-1-4. Relaxor ferroelectrics

Relaxors are ferroelectric materials that have moderate temperature coefficients of dielectric properties. In classical ferroelectrics like BaTiO$_3$, spontaneous polarization disappears by phase transition to symmetric structure with a sharp peak in dielectric constant-temperature graphs (**Fig. 1-5**). [1,4] On the other hand, some prototypical relaxors such as Pb(Mg$_{1/3}$Nb$_{2/3}$)O$_3$ (PMN) maintain large relative dielectric constants even at high temperature without a sharp phase transition [2,5], as indicated in **Fig. 1-6**. Such materials show a huge dielectric response over wide frequency and temperature ranges. These characteristics originate from nano meter-sized polarized regions (Polar Nano Regions, PNRs) dispersed over averagely symmetric matrix as schematically depicted in **Fig. 1-7**. [2,5] PNRs are generally formed by the presence of different valence cations between neighboring crystalline cells. Chemically ordered region with Mg:Nb = 1:2 seems to be centrosymmetric, while disordering of Mg^{2+} and Nb^{5+} forms locally polarized regions. [2,5] In other words, PNRs are introduced by compositional inhomogeneity as in the crystalline lattice model of **Fig. 1-8**. [2,5]

While the most attractive characteristic of relaxors is their large dielectric constants over wide temperature and frequency ranges, several unique behaviors were reported by Burns and other researchers. [6,7] Non-linear optical effect was reported on
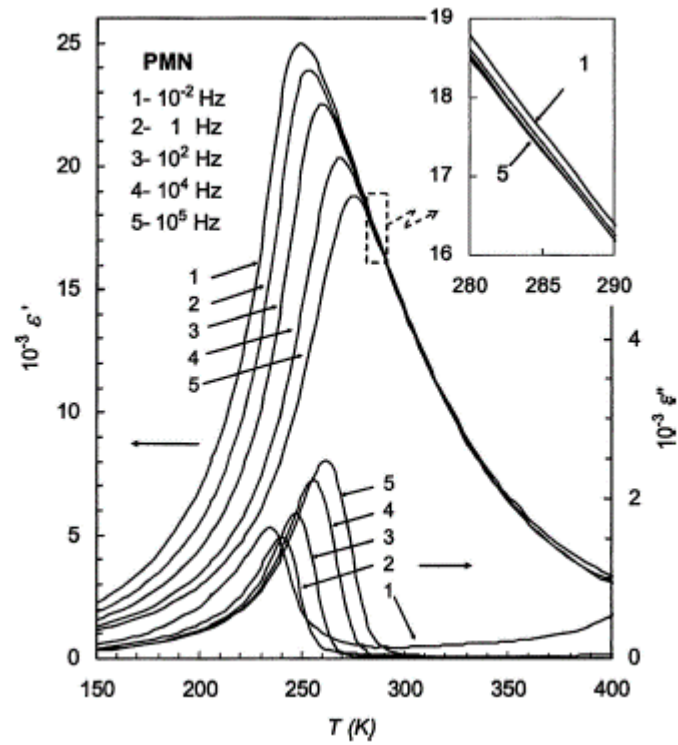
Fig. 1-6. Temperature dependences of the real and imaginary parts of the relative dielectric constants evaluated at various frequencies for a single crystal of Pb(Mg$_{1/3}$Nb$_{2/3}$)O$_3$ (PMN). [5]
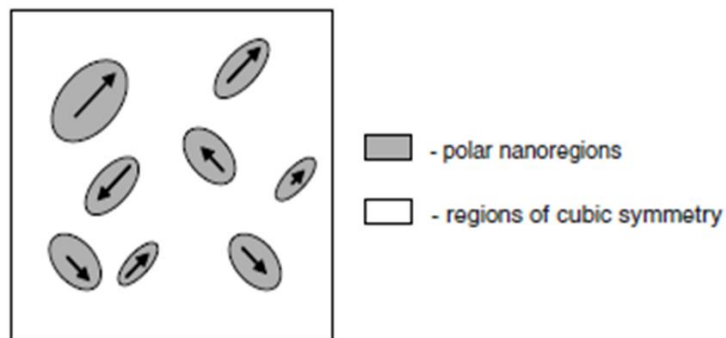
Fig. 1-7. Schematic image of PNRs (gray ellipsoids) dispersed over averagely symmetric matrix (white region). [5]
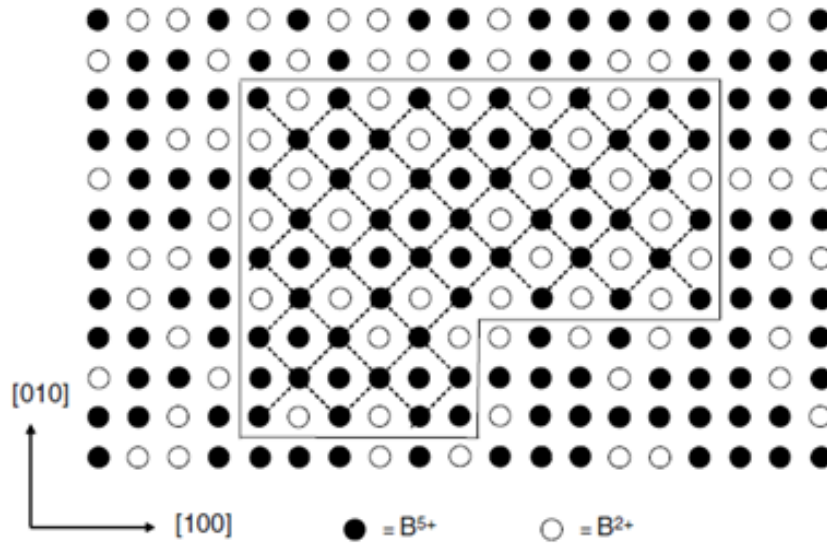
Fig. 1-8. Inhomogeneous *B*-site occupation model of Pb(Mg$_{1/3}$Nb$_{2/3}$)O$_3$ (PMN). [5] Black and white circles indicate Nb^{5+} and Mg^{2+}, respectively. For example, the average charge of the area enclosed with solid line is 4+, but there are disordering of the Nb^{5+} and Mg^{2+} cations to form PNRs.

PMN single crystals even at the temperature higher than their phase transition point in the year of 1983. [6] It was attributed to the remnant polarization of thermally robust PNRs. In addition, polar domain sizes in relaxors decrease at the elevated temperature and their polar direction can be switched by relatively low electrical voltage because smaller domains were easily reoriented by the assist of thermal fluctuations. [2,8] The upper limit of the temperature for relaxor ferroelectrics to maintain PNRs is called Burns temperature. [6]

1-2. Metal oxynitrides

To date, the most widely utilized inorganic materials are metal oxides for the easiness of synthesis and fabrication of their ceramics and bulk single crystals. On the other hand, many trials of modifying their properties have been made by substituting their oxide anions with other anions to form oxynitrides, oxyfluorides, fluoronitrides, oxyfluoronitrides, oxysulfides, oxyselenides, and oxychlorides. [9-21] Among the candidates of mixed anion inorganic compounds, the combination of oxygen and nitrogen is appropriate for the similarities in their ionic radii and electronegativities [22,23] as summarized in **Table 1-1**. Metal nitrides and oxynitrides have attracted considerable attention for their promising optical, mechanical, superconducting, dielectric, and visible light-driven photocatalytic properties. [24-29] For example, GaN, AlN, TiN, and SiAlONs are industrially important materials for their applications as blue light emitting diodes [30-33], thermal conductive substrates in electrical circuits [34-36], structural

Table 1-1. Average electronegativities and ionic radii of anionic elements. [22,23]

	B	C	N	O	F	P
Electronegativity	2.04	2.55	3.04	3.44	3.98	2.19
Ionic radii / pm	25	29	132	124	117	31
	S	Cl	As	Se	Br	I
Electronegativity	2.58	3.16	2.18	2.55	2.96	2.66
Ionic radii / pm	-	-	48	42	-	-

Coordination number is four in the ionic radii on this Table.

materials [37-44], and phosphors. [45-47] Such properties are attributed to the presence of nitrogen, which introduces higher covalency and narrower optical bandgaps compared with oxide materials. [48-50] A number of trials have been made to fabricate dense ceramics as well as single crystals of such materials for their industrial usages and evaluation of properties with high reliability. However, research field on the processing of oxynitrides have not been developed very much for the difficulty in the fabrication of highly-densified ceramics, single crystals, fine powders with uniformed particle sizes, and so on. There are some examples of the preparation of oxynitride thin films, but their chemical compositions especially nitrogen contents are not confirmed in most cases. [51-55] Hence, most of the researches on oxynitrides have been conducted on their crystal structure, fluorescence, and catalytic properties, all of them can be studied in the form of as-synthesized powder.

1-2-1. Syntheses of perovskite-type oxynitrides by ammonolysis

Over the last 30 years, a variety of oxynitride compounds with perovskite-type crystal structure have been synthesized. Many examples such as AETaO$_2$N (AE = Ca, Sr, Ba), AENbO$_2$N, LnTaON$_2$ (Ln = lanthanoid), LnTiO$_2$N, NdVO$_2$N, non-stoichiometric compound SrMo(O,N)$_3$, BaTi(O,N)$_3$, and a series of Ruddlesden-Popper type layered

perovskites have been reported. [48,50,56-70,72-74] Previously reported examples of

oxynitride perovskites are summarized in **Table 1-2**. The most widely employed their

synthetic route is the heating of their oxide precursors or oxide powder mixtures with

stoichiometric metal ratios under flowing ammonia. This method called ammonolysis is

conducted at approximately $900 - 1000\ °C$ and yellow or reddish colored powders having

decreased optical bandgaps introduced by the presence of nitrogen are obtained. It has

been suggested that gaseous ammonia partially decomposes to highly reactive radical

nitriding reagents (NH_2, NH) and molecular hydrogen, which reacts with oxide starting

materials generating water. And nitrogen is inserted to the specific position where had

been occupied by oxygen. The comprehensive study of the ammonolysis reaction

mechanism has not been established, but in the case of the formation of $BaTaO_2N$, its

nitridation process was closely investigated on the basis of the decomposition of NH_3.

[71]

1-2-2. Novel synthetic routes of oxynitride perovskites

In recent years, ammonia-free syntheses of oxynitride perovskites have been

explored by several groups. Reactions between alkaline-earth monoxides and TaON at

high temperature of 1400 °C were performed by the group of Clarke. [57] However, the

Table 1-2. Oxynitride perovskites reported until the year of 2019.

Structure type	Compound name	Note	Refs.
Perovskite	$BaTaO_2N$		56
	$SrTaO_2N$		57
	$SrTaO_2N_{0.7}$	Nitrogen defects are contained.	69
	$CaTaO_2N$		48
	$EuTaO_2N$		70
	$Ca_{1-x}Eu_xTa(O,N)_3$		70
	$Ln TaON_2$	Ln = La, Ce, Pr, Nd, Sm, Gd, Eu	58
	$LaNbON_2$		58
	$BaNbO_2N$		56
	$SrNbO_2N$		60
	$EuNb(O,N)_3$		58
	$Ln TiO_2N$	Ln = La, Nd	58,72
	$La_{1-x}Sr_xTiO_{2+x}N_{1-x}$		59
	$LaZrO_2N$		72
	$BaTi(O,N)_3$		68
	$SrW(O,N)_3$		66
	$LaW(O,N)_3$		74
	$SrMo(O,N)_3$		65,66
	$NdVO_2N$		67
	$LaV(O,N)_3$		73
Ruddlesden-Popper	Ba_2TaO_3N		57
	$Sr_{1+n}Ta_nO_{2+n}N_n$	n = 1, 2	57,61
	$Sr_{1+n}Nb_nO_{2+n}N_n$	n = 1, 2	60,61
	Ln_2AlO_3N	Ln = Nd, Sm	63,64
	$Gd_{1+x}Ca_{1-x}AlO_{4-x}N_x$		62

colors of such products are black or brown, which indicates that a number of anion defects are contained to reduce Ta^{5+} during the high temperature processes. In other works, solid state reactions of alkaline-earth carbonates and Ta_3N_5 at approximately $900 - 1100$ °C were investigated using thermogravimetry in combination with gas chromatography. [75,76] Gaseous carbon dioxide generated by the decarboxylation from metal carbonates partially oxidizes Ta_3N_5 and reaction intermediate of TaON is formed. Then alkaline-earth monoxides react with TaON to generate oxynitride perovskites. Another synthetic procedure of $SrTaO_2N$ from $Sr_2Ta_2O_7$ was performed using C_3N_4 as both of a reducing reagent for $Sr_2Ta_2O_7$ starting material and a nitrogen source. [77] Phase-pure $SrTaO_2N$ was obtained by the reaction at 800 °C. Particle sizes of $SrTaO_2N$ prepared in this process were very small (< 100 nm) and uniform because of the low temperature process compared to the conventional ammonolysis products at 1000 °C (> 100 nm). [77]

1-3. Dielectricity and crystal structure of oxynitride perovskites

In 2004, unusually high relative dielectric constant values of $BaTaO_2N$ ($\varepsilon_r \approx$ 4600) and $SrTaO_2N$ ($\varepsilon_r \approx$ 3000) over a temperature range of $180 - 300$ K were reported for their powder compacts with relative density (RD) of approximately 45% after annealing at 1050 °C in ammonia. [78] After this report, a number of trials were

performed to fabricate dense ceramics and thin films targeting the evaluation of their

intrinsic electrical properties for their applications as lead-free, environmentally friendly

dielectric materials.

1-3-1. Local symmetry breaking involving anion ordering

The emergence of large relative dielectric constant values cannot be explained

in relation to their centrosymmetric space groups (tetragonal $I4/mcm$ for SrTaO$_2$N (a =

0.569411(7) nm, c = 0.80658(2) nm) and cubic $Pm\bar{3}m$ for BaTaO$_2$N (a = 0.41128(1) nm)

determined by powder X-ray and neutron diffractions. [56,57,78] In response to this

enigma, local structure of BaTaO$_2$N was studied employing TEM, EXAFS, and neutron

pair distribution functions and the different distances in Ta-O and Ta-N bonds were

reported. [79-81] This suggests that each Ta atom slightly displaces in one direction from

its averaged centrosymmetric positions in cubic BaTaO$_2$N, making one dimensional

(linear) PNRs. [80]

Distinguishing oxygen from nitrogen by X-ray diffraction is challenging due to

their similar X-ray scattering powers. Neutron diffraction is a powerful means to identify

the positions of these elements, due to the different neutron scattering length of oxygen

(5.803 fm) and nitrogen (9.360 fm). [82] Using this approach, two independent research

groups reported local *cis*-type anisotropic configurations of nitride anions in TaO_4N_2 and

NbO_4N_2 octahedra in $SrTaO_2N$ and $SrNbO_2N$. [83,84] In addition, it was reported that

$LaTiO_2N$, $La_{1-x}Sr_xTiO_{2+x}N_{1-x}$ ($x = 0 - 0.2$), and $NdVO_2N$ perovskites have similar *cis*-type

O/N configuration in TiO_4N_2 octahedra. [67,69] Such anisotropic anion configuration is

favored in many compounds of transition metals with d^0 electron configurations. [87]

1-3-2. DFT structure optimizations on oxynitride perovskites

Density functional theory (DFT) calculations of both $SrTaO_2N$ and $BaTaO_2N$

with *cis*-type anion configuration model pointed out the formation of helical coil-like

polar Ta-N-Ta-N chains with various lengths and directions. [88] The authors of this paper

expected the presence of three-dimensional polar nano regions (PNRs) formed by polar

Ta-N-Ta-N chains and relaxor-like ferroelectric properties in these oxynitride perovskites.

[88] Such relaxor properties originate from anisotropic local structure in oxynitride

materials with homogeneous chemical compositions are quite different from the

prototypical oxide relaxors with compositional inhomogeneities shown in **Fig. 1-8**. [2,5]

Additional DFT calculations of each crystal structure of oxynitride perovskites

have been performed by several independent groups. Structure optimizations on

$CaTaO_2N$, $SrTaO_2N$, and $BaTaO_2N$ were performed by total-energy calculations and

phonon-computations. [89] Interestingly enough, all of them were determined to be stable in the space group of orthorhombic *Pnma*, unlike previous their powder neutron diffraction results (*I*4/*mcm* for SrTaO$_2$N and *Pm*$\bar{3}$*m* for BaTaO$_2$N). [56,57] Further structure optimization was performed on BaTaO$_2$N to find out that the most favored structure is non-centrosymmetric *Pmc*2$_1$ space group. [89] This result has been extended to a series of oxynitride perovskites such as *Ln*TaON$_2$ (*Ln* = La, Ce, Pr) and CaTaO$_2$N. [86] These reports propose an explanation that polar local structure is present in a variety of oxynitride perovskites which had been believed to be centrosymmetric average structure by powder diffraction data. Because of these findings, fabrication of dense ceramics or single crystals are desired to evaluate the intrinsic electrical properties in oxynitrides.

1-4. Densification processes of oxynitride perovskites

1-4-1. Overview of sintering theory

Sintering behavior of inorganic compounds is connection and consolidation of each powder particle to densify and strengthen the ceramic products. Here, the principles of the densification mechanism of inorganic compounds are briefly reviewed. The major mechanisms are surface diffusion, bulk (volumic) diffusion, dissolution-precipitation

involving liquid phase, and evaporation-condensation process. Schematic image

summarizing the diffusion procedure is depicted in **Fig. 1-9**. They are strongly related to

the diffusion phenomena of target materials. Sintering proceeds using the decrease in the

surface free energy on the interface between solid and gas phases as a driving force. The

entire process can be divided into three steps, i.e. (i) particle rearrangement to realize the

intimate packing of neighboring grains, (ii) some necking between grains by material

diffusion via vapor phase, which is called surface diffusion, (iii) boundary and the

volumic diffusions to densify the ceramics by eliminating voids towards the exterior of

the bulks. The surface energy will be minimized by filling up the voids that ideally should

be diminished to the exterior of the ceramics.

Generally, the free energy change during diffusion is expressed as the following

function of diffusion coefficient. [91,92]

$$\frac{\mathrm{d}\rho}{\mathrm{d}t} \approx \frac{\Omega_i \gamma \delta_b^m D_{eff}}{kT d^n} F(\rho)\rho \qquad (1\text{-}8)$$

Where ρ is density, t is time, Ω is atomic volume, γ is surface energy, δ_b is boundary

diffusion width, D_{eff} is effective diffusion constant, k is Boltzmann constant, T is absolute

temperature, d is grain size. Exponents m and n depend on the controlling diffusion

medium. Sintering involving diffusion of solid phase is called solid state sintering. This

process is known to proceed above 70% of the absolute melting points of the target

materials. [90] However, this procedure is not applicable to the materials with extremely high melting points like metal nitrides, oxynitrides, borides, and carbides. Such covalent bonding crystals cannot be sintered by simple heating because most of them thermally decompose during high temperature processes.

The materials difficult to sinter are densified by means of the diffusions assisted by other factors like molten solvent (liquid phase sintering) [92-103] and chemical reactions (reaction sintering). [99,102,104] The latter process is accelerated by the material transportation during chemical reactions between the starting materials in the green-compacts. As for the liquid phase sintering, fluxes that play a role of solvent for target materials to assist their rapid diffusions via dissolution and precipitation are employed. The merit of this procedure is that their sintering temperatures can be lowered if a sintering additive with a low melting point is employed.

Diffusion in liquid phase sintering is significantly rapid compared to solid state sintering. It proceeds with a series of steps; (i) wetting on the surface of solid phase with melt of sintering additive (ii) reorientation of grains (iii) dissolution and precipitation via solvent. [92] Wetting of the material surface is a key factor to supply the diffusion medium to as many grains as possible.

After the wetting and reorientation of grains, target materials diffuse via
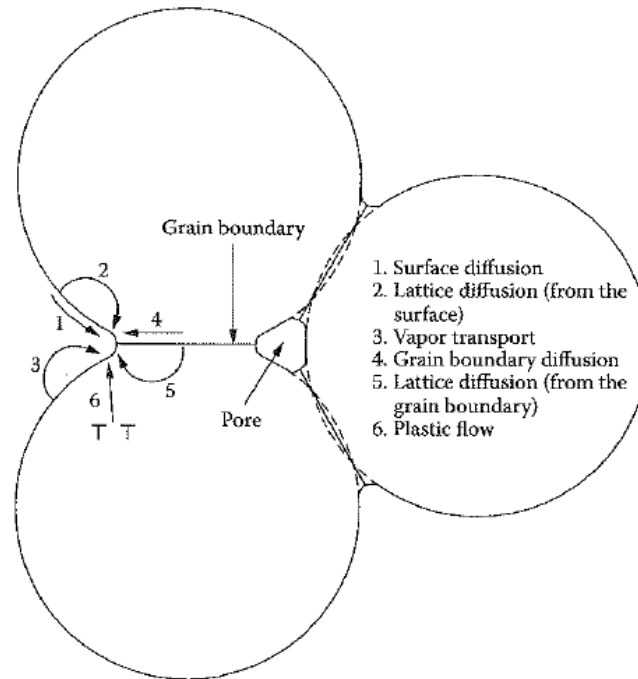
Fig. 1-9. Diffusion mechanism during sintering of powders. [91]

dissolution and precipitation. In this process, necking, fusion of tiny particles, densification of the ceramics, and grain growth proceed simultaneously. Important factor is that target materials are dissolved to the melt of a sintering additive. Three types of densification process are proposed in liquid phase sintering as illustrated in **Fig. 1-10**. These are; (a) smoothing of contacting points of solid particles, (b) dissolution of tiny particles and their reprecipitation on the surface of large grains, and (c) necking growth of grain boundaries. [92] The necking growth uses grain boundary as a material
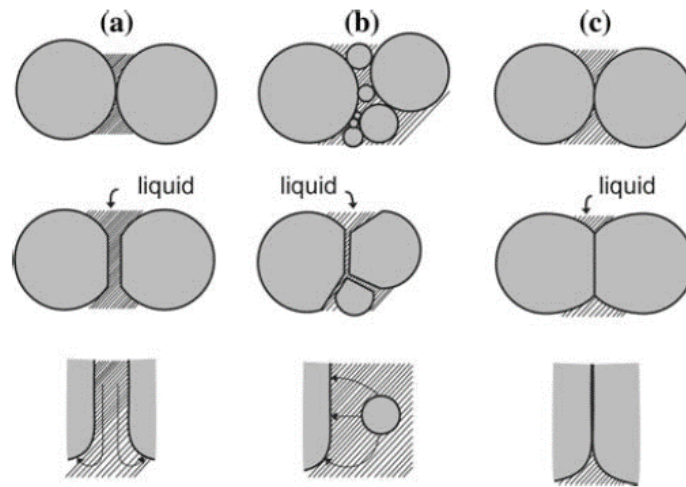
Fig. 1-10. The three mechanisms of **(a)** grain accommodation, **(b)** dissolution and reprecipitation, and **(c)** grain boundary diffusion in liquid phase sintering. [92]

source as in solid state sintering and then straight boundaries are formed.

Other sintering procedures that are effective for the materials difficult to sinter are hot press sintering [105-109], hot isostatic press sintering (HIP) [110-114], microwave sintering [104], spark plasma sintering (SPS) [115,116], and so on. These technics assist the grain growth, crack healing, densification, and lowering sintering temperatures to avoid thermal decompositions.

1-4-2. Sintering procedures of metal nitrides and oxynitrides

Conventional sintering procedures for oxide materials are not applicable to nitrides and oxynitrides due to their extremely small diffusion constants. [117] Additional approaches using additives and high pressure are necessary to assist the diffusion of such

covalent crystals. Well known examples are the fabrications of AlN [34-36,96-100,103], BN [34,42-44], Si_3N_4 [110-114,118-120], and TiN [38] ceramics and crystals. Liquid phase sintering of these nitride materials was achieved by employing the sintering additives of oxides of alkaline metals, boron, or rare earth metals as the sources of liquid phase. [92-103] The application of high pressure in hot pressing, hot isostatic pressing, and spark plasma sintering will be effective for further densification. [104-116]

Sometimes oxynitride compounds are considered as the derivatives of oxides, but their sintering is difficult owing to the high covalency of the bonds between metals and nitrogen making their diffusion constants quite small. Al_3O_3N (AlON) with spinel-type structure and SiAlON oxynitrides are well known exceptional examples that can be sintered, but in both cases sintering additives of metal oxides and nitrides to generate liquid phase at lower temperature than their decomposition points are necessary to fabricate dense ceramics, as in the cases of the abovementioned typical main-group metal nitrides. [96-102,112,113,116]

1-4-3. Flux growth of metal nitride crystals

Sigle crystal is the most desirable sample form for solid state chemistry because quite reliable information on their intrinsic properties can be obtained. Solvents for target

materials are called fluxes and their crystals are grown via dissolution and recrystallization phenomena. Crystals larger than a certain size can be utilized for the evaluations of their intrinsic electrical, mechanical, heat-conducting properties, and so on. Single crystals are obtained by a cooling or flux evaporation to supersaturate the solutions that contain target materials as solutes. [121] The most common technique for realizing supersaturation is a slow cooling of solutions when the materials solubilities of which are strongly affected by temperature. The slower cooling rate is, the higher quality and the larger crystals are. Another process, flux evaporation, is suitable for the crystals of materials that show moderate solubilities to solvents against temperature. The loss of solvents assists the condensation of the solution at constant temperature. [121]

Crystal growth of metal nitrides and oxynitrides is very challenging due to a lack of the knowledge of appropriate fluxes. To date, only a few examples of the fluxes are known. They are sodium metal or sodium azide (NaN_3) [122,123], Li_3N [124], Ca_3N_2 [36] for various nitrides of typical metals, and self-flux of Li_3BN_2 for the productions of *h*- and *c*-BN crystals. [43,44,125] Few production reports have been published for the fabrications of the crystals of oxynitrides containing transition metals due to the difficulty in maintaining their chemical compositions.

1-4-4. Densification processes of SrTaO₂N

Sintering of SrTaO₂N at high temperature

There are few reports of sintering behaviors of oxynitrides containing transition metals owing to their strong tendency to be reduced during high temperature processes. Among such compounds, thermal stability and sinterability of $SrTaO_2N$ involving its partial decomposition were studied in the group of Kikkawa. [69,126,127] $SrTaO_2N$ begins releasing a part of its nitrogen at about 950 °C in an inert atmosphere. Approximately 30% of nitrogen is lost up to 1200 °C, but its perovskite-type crystalline lattice is maintained. [69] $SrTaO_2N$ changes from orange insulator to black semiconductor reducing the oxidation state of Ta^{5+}. [69,126,127] Further decomposition behaviors strongly depend on heating atmosphere. Perovskite-type structure of $SrTaO_2N_{0.7}$ is thermally robust under nitrogen atmosphere and further decomposition is only a slight loss of SrO. [69] On the other hand, the perovskite-type phase completely decomposes to $Sr_{1.4}Ta_{0.6}O_{2.73}$, Ta_2N, and $Sr_5Ta_4O_{15}$ in helium. [69]

$SrTaO_2N$ can be sintered in nitrogen above 1400 °C losing some of its nitrogen and SrO. [69,126,127] Addition of a small amount of $SrCO_3$ to $SrTaO_2N$ was performed to compensate for the loss of SrO and phase-pure $SrTaO_2N_{0.7}$ ceramics can be sintered under 0.2 MPa of nitrogen above 1400 °C in BN crucible. [126,127] Resultant black

SrTaO$_2$N$_{0.7}$ ceramics were post-annealed in flowing ammonia to supply nitrogen for the ceramic products. Orange color and electrically insulating property were recovered by this post-ammonolysis. [126,127] SrTaO$_2$N ceramics with orange color even in their interiors were obtained only for the SrTaO$_2$N$_{0.7}$ ceramics with RD values less than 84%. [127] On the other side, only the outermost surface in a thickness of several micrometers could be re-nitrided in the case of highly densified ceramics of RD > 90%. In this case, their interiors still remained as semiconducting SrTaO$_2$N$_{0.7}$. [127,128] Electrical resistivity of the post-annealed ceramic products differs depending on the synthetic routes of the original SrTaO$_2$N powders. Zhang, who reported the sintering of SrTaO$_2$N for the first time [126], prepared the starting SrTaO$_2$N powder by the ammonolysis of Sr$_2$Ta$_2$O$_7$ precursor obtained by sol-gel synthesis using SrCl$_2$, TaCl$_5$, and citric acid. Residual carbon is suspected to have a negative influence on the insulating properties of ceramic products, which showed its high dielectric loss tanδ values larger than 0.4 even after post-ammonolysis. [126] Instead, Sun synthesized SrTaO$_2$N powder from Sr$_2$Ta$_2$O$_7$ obtained by the solid state reaction between SrO and Ta$_2$O$_5$. [127] The ceramic products showed much better electrical insulation. The post-annealed SrTaO$_2$N ceramics with RD = 83.3% had a relatively high ε_r of 450 with a low tanδ less than 0.1. These values are almost independent of frequency and temperature. [127] Piezoresponse as well as local

capacitance hysteresis loops were also observed in the scratched off surface area of post-annealed dense SrTaO$_2$N ceramics with RD > 90%. [128] The polarization signal increased by the applied voltage and its coercive electrical bias was estimated to be approximately ±8 V. Further bias to saturate the polarization could not be applied because of an electrical current leakage. So, most importantly, invention of a densification technic of highly-insulating oxynitride perovskites is desired.

Densification of SrTaO$_2$N under high pressure

Apart from the abovementioned pressureless sintering, several trials have been made to obtain oxynitride ceramics by the assist of applied pressure. Hot isostatic press (HIP) sintering has been a powerful tool to densify oxide ceramics. For nitride-based materials, it has also been utilized for Si$_3$N$_4$ ceramics by assisting their grain growth, crack healing, densification etc. [110-114] Zhang applied a glass capsule-HIP sintering to SrTaO$_2$N powder compacts under 196 MPa of Ar gas pressure at 1200, 1400, and 1600 °C for 3 h. [129] Their products were contaminated with tantalum carbide and Sr$_2$Ta$_2$O$_7$ impurities and partial nitrogen loss from SrTaO$_2$N occurred, similar to that observed during pressureless sintering under 0.2 MPa of nitrogen. [126,127]

In another work, high nitrogen pressure of 190 MPa was directly applied to SrTaO$_2$N compacts and their sintering behavior was studied. [130] Perovskite phase was

maintained up to 1450 °C for additive-free $SrTaO_2N$ and rapid grain growth to larger than 10 μm was observed. [130] However, partial loss of nitrogen was inevitable even under the pressurized nitrogen, suggesting that nitrogen-deficient phase $SrTaO_2N_{0.7}$ is more stable than $SrTaO_2N$ at high temperature. [130]

Densification of $SrTaO_2N$ with mechanical pressure of 7 GPa applied by belt-type high pressure apparatus was also tried by Masubuchi. [131] Neither grain growth nor sintering behavior were observed in the ceramic products and the maximum RD value remained 83%. [131] Surprisingly, $SrTaO_2N$ changed to black semiconductor in this high pressure treatment, indicating that anion defects are formed during this process. [131]

The above results suggest that fabrication of oxynitride perovskite ceramics avoiding their partial nitrogen loss is quite difficult due to the mismatch of their high sintering temperature and low thermal stability.

1-4-5. Electrical properties of $SrTaO_2N$ thin films

Compressively strained $SrTaO_2N$ thin films also showed ferroelectric behavior [51,54], which was observed only in tiny domains in the size of 10 – 100 nm. In addition to such inhomogeneity, they showed electrical leakage during *P-E* measurements as in the cases of ceramic specimens. [51] The author of this report proposed the *trans*-type

anion configuration model by DFT calculation [51], which is not consistent with the *cis-*

type local structure confirmed by powder neutron diffraction studies. [83,84] Self-

standing bulks such as fully-densified ceramics or single crystals of oxynitride

perovskites with high electrical insulation are much more desirable to remove such

ambiguity of their electrical properties in previous researches.

1-5. Purpose of the present research

Polarizations in thin $SrTaO_2N$ ceramic specimens mentioned above could not be

saturated because of their poor insulation. A contribution of semiconducting residue even

after post-ammonolysis is suspected on such electrical current leakage. Fabrication of

self-standing oxynitride ceramics or single crystals containing transition metals will be a

valuable work in both aspects of solid state chemistry and industry. In the present research,

$BaTaO_2N$ was selected as a main target material expecting similar sinterability and

dielectric properties to $SrTaO_2N$. The main scope of this work is sintering and crystal

growth of $BaTaO_2N$ maintaining its stoichiometry to elucidate the presence of

ferroelectricity, which has been suggested by structural studies for a decade.

This thesis is consisted of eight sections including general introduction (the

present chapter), experimental results and discussion part (**Chapters 2 – 7**), and

conclusion (**Chapter 8**). First of all, reinvestigation of the crystal structure of $BaTaO_2N$ was performed considering non-centrosymmetric structural model as a candidate. Then, thermal stability and high temperature sintering of $BaTaO_2N$ to form nitrogen-deficient $BaTaO_2N_{0.85}$ ceramics followed by a post-ammonolysis were studied to observe the large relative dielectric constants that do not depend on temperature in $BaTaO_2N$ ceramics. Afterwards thermal behaviors of alkaline-earth metal carbodiimides were investigated to find out that $BaCN_2$ has a low melting point of 910 °C and its melt is useful for the crystal growth of oxynitride perovskites. The effects of the amount of $BaCN_2$ flux and heating/cooling conditions on the crystal growth were investigated with their microstructural studies. Piezoelectricity of micron-sized $BaTaO_2N$ crystals grown in a $BaCN_2$ flux was studied to observe ferroelectric polarization phase alternation. Such behavior of $BaTaO_2N$ crystals is explained in conjunction with the theory of polar nano regions consisted of anisotropic anion ordering. In addition, $BaCN_2$ was utilized as a sintering additive of $BaTaO_2N$ and its ceramics were obtained avoiding partial decomposition in a spark plasma sintering (SPS) furnace. In the last chapter, comprehensive explanation of the densification processes, ferroelectricity, and crystal structure of $BaTaO_2N$ is given.

Chapter 1 References

[1] "*Solid State Chemistry and Its Applications 2nd Ed.*", A. R. West (Ed.), John Wiley & Sons, Ltd., United Kingdom (2014), p57.

[2] M. Itoh, "*Handbook of Solid State Chemistry*", Vol. 1, R. Dronskowski, S. Kikkawa, A. Stein (Eds.), Wiley-VCH, Weinheim, New York (2017).

[3] K. Momma, F. Izumi, "VESTA 3 for three-dimensional visualization of crystal, volumetric and morphology data", *J. Appl. Crystallogr.*, 2011, 44, 1272–1276.

[4] K. Kinoshita, A. Yamaji, "Grain-size effects on dielectric properties in barium titanate ceramics", *J. Appl. Phys.*, 1976, 47, 371–373.

[5] A. A. Bokov, Z. -G. Ye, "Recent progress in relaxor ferroelectrics with perovskite structure", *J. Mater. Sci.*, 2006, 41, 31–52.

[6] G. Burns, F. H. Dacol, "Glassy Polarization in Ferroelectric Compounds Pb (Mg$_{1/3}$Nb$_{2/3}$)O$_3$ and Pb(Zn$_{1/3}$Nb$_{2/3}$)O$_3$", *Solid State Commun.*, 1983, 48, 853–856.

[7] A. M. Pugachev, V. I. Kovalevskii, N. V. Surovtsev, S. Kojima, S. A. Prosandeev, I. P. Raevski, S. I. Raevskaya, "Broken Local Symmetry in Paraelectric BaTiO$_3$ Proved by Second Harmonic Generation", *Phys. Rev. Lett.*, 2012, 108, 247601.

[8] D. Fu, H. Taniguchi, M. Itoh, S. Koshihara, N. Yamamoto, S. Mori, "Relaxor Pb(Ma$_{1/3}$Nb$_{2/3}$)O$_3$: A Ferroelectric with Multiple Inhomogeneities", *Phys. Rev. Lett.*, 2009, 103, 207601.

[9] T. A. Kodenkandath, J. N. Lalena, W. L. Zhou, E. E. Carpenter, C. Sangregorio, A, U. Falster, W. B. Simmons, C. J. O'Connor, J. B. Wiley, "Assembly of Metal-Anion Arrays within a Perovskite Host. Low-Temperature Synthesis of New Layered Copper-Oxyhalides, (CuX)LaNb$_2$O$_7$, X = Cl, Br", *J. Am. Chem. Soc.*, 1999, 121, 10743–10746.

[10] C. -Q. Jin, X. -J. Wu, P. Laffez, T. Tatsuki, T. Tamura, S. Adachi, H. Yamauchi, N. Koshizuka, S. Tanaka, "Superconductivity at 80 K in (Sr,Ca)$_3$Cu$_2$O$_{4+\delta}$Cl$_{2-y}$ induced by apical oxygen doping", *Nature*, 1995, 375, 301–303.

[11] C. Perrin, S. Cordier, S. Ihmaine, M. Sergent, "Recent investigations on the (Me$_6$L$_{18}$)^n unit based halides and oxyhalides (Me □ Nb, Ta and L □ Cl, Br, O) with rare earths as countercations: Electronic and steric effects", *J. Alloys Comp.*, 1995, 229, 123–133.

[12] S. -T. Hong, A. W. Sleight, "Crystal Structure of New 10-Layer Perovskite-Related Oxyhalide Ba$_5$Ru$_{1.6}$W$_{0.4}$Cl$_2$O$_9$", *J. Solid State Chem.*, 1997, 132, 407–410.

[13] I. O. Troyanchuk, N. V. Kasper, O. S. Mantytskaya, E. F. Shapovalova, "HIGH-PRESSURE SYNTHESIS OF SOME PEROVSKITE-LIKE COMPOUNDS WITH A MIXED ANION TYPE", *Mater. Res. Bull.*, 1995, 30, 421–425.

[14] D. Pauwels, A. Demourgues, H. Laronze, P. Gravereau, F. Guillen, O. Isnard, A. Tressaud, "Structural features of new rare earth-based mixed anions (O, S, F) compounds: relationships between optical absorption and rare earth environment", *Solid State Sci.*, 2002, 4, 1471–1479.

[15] B. L. Chamberland, "A NEW OXYFLUORIDE PEROVSKITE, $KTiO_2F$", *Mater. Res. Bull.*, 1971, 6, 311–316.

[16] M. T. Vandenborre, E. Husson, J. L. Fourquet, "Etude spectroscopique par absorption infra-rouge et diffusion Raman de composes oxyfluores de structure pyrochlore ANb_2O_5F (A = Rb, Cs, Tl) et $RbTa_2O_5F$", *Mater. Res. Bull.*, 1982, 17, 1359–1364.

[17] J. W. Fergus, H. -P. Chen, "Structure and Conductivity of Tetragonal and Rhombohedral Lanthanum Oxyfluoride Compounds", *J. Electrochem. Soc.*, 2000, 147, 4696–4704.

[18] J. Yang, J. Liang, G. Rao, Y. Qin, Y. Shi, W. Tang, "Synthesis and superconductivity of $Nd_{0.7}Sr_{1.3}Cu(O,F)_{4-\delta}$ with $T_c = 44$ K", *Physica C*, 1996, 270, 35–40.

[19] G. S. Case, A. L. Hector, W. Levason, R. L. Needs, M. F. Thomas, M. T. Weller, "Syntheses, powder neutron diffraction structures and Mossbauer studies of some complex iron oxyfluorides: $Sr_3Fe_2O_6F_{0.87}$, Sr_2FeO_3F and $Ba_2InFeO_5F_{0.68}$", *J. Mater. Chem.* 1999, 9, 2821–2827.

[20] F. Galasso, W. Darby, "PREPARATION AND PROPERTIES OF Sr_2FeO_3F", *J. Phys. Chem.*, 1963, 67, 1451–1453.

[21] K. Ueda, H. Hosono, "Band gap engineering, band edge emission, and *p*-type conductivity in wide-gap $LaCuOS_{1-x}Se_x$ oxychalcogenides", *J. Appl. Phys.*, 2002, 91, 4768–4770.

[22] A. L. Allred, "Electronegativity values from thermochemical data", *J. Inorg. Nucl. Chem.*, 1961, 17, 215–221.

[23] R. D. Shannon, "Revised effective ionic radii and systematic studies of interatomic distances in halides and chalcogenides", *Acta Cryst.*, 1976, A32, 751–767.

[24] S. G. Ebbinghaus, H. -P. Abicht, R. Dronskowski, T. Muller, A. Reller, A. Weidenkaff, "Perovskite-related oxynitrides—recent developments in synthesis, characterization and investigations of physical properties.", *Prog. Solid State Chem.*, 2009, 37, 173–205.

[25] K. Maeda, T. Tanaka, M. Hara, N. Saito, Y. Inoue, H. Kobayashi, K. Domen, "GaN:ZnO Solid Solution as a Photocatalyst for Visible-Light-Driven Overall Water Splitting", *J. Am. Chem. Soc.*, 2005, 127, 8286–8287.

[26] K. Maeda, K. Teramura, D. Lu, T. Takata, N. Saito, Y. Inoue, K. Domen, "Photocatalyst releasing hydrogen from water", *Nature*, 2006, 440, 295.

[27] C. Pan, T. Takata, M. Nakabayashi, T. Matsumoto, N. Shibata, Y. Ikuhara, K. Domen, "A Complex Perovskite-Type Oxynitride: The First Photocatalyst for Water Splitting Operable at up to 600 nm", *Angew. Chem. Int. Ed.*, 2015, 54, 2955–2959.

[28] K. Maeda, "CO_2 reduction using oxynitrides and nitrides under visible light", *Prog. Solid State Chem.*, 2018, 51, 52–62.

[29] Y. Lee, H. Terashima, Y. Shimodaira, K. Teramura, M. Hara, H. Kobayashi, K. Domen, M. Yashima, "Zinc Germanium Oxynitride as a Photocatalyst for Overall Water Solitting under Visible Light", *Phys. Chem. C*, 2007, 111, 1042–1048.

[30] S. Nakamura, T. Mukai, M. Senoh, "*In situ* monitoring and Hall measurements of GaN grown with GaN buffer layers", *J. Appl. Phys.*, 1992, 71, 5543–5549.

[31] J. I. Pankove, J. E. Berkeyheiser, E. A. Miller, "Properties of Zn-doped GaN. I. Photoluminescence", *J. Appl. Phys.*, 1974, 45, 1280–1286.

[32] S. Nakamura, T. Mukai, M. Senoh, "Candela-class high-brightness InGaN/AlGaN double-heterostructure blue-light-emitting diodes", *Appl. Phys. Lett.*, 1994, 64, 1687–1689.

[33] I. Akasaki, "Nitride Semiconductors, –Evolution and Prospect–", *J. Cryst. Soc. Jpn.*, 2003, 30, 44–53.

[34] J. A. Sanjurjo, E. Lopez-Cruz, P. Vogl, M. Cardona, "Dependence on volume of the phonon frequencies and their effective charges of several III-V semiconductors", *Phys. Rev. B*, 1973, 28, 4579–4584.

[35] G. A. Slack, "NONMETALLIC CRYSTALS WITH HIGH THERMAL CONDUCTIVITY", *J. Phys. Chem. Sol.*, 1973, 34, 321–335.

[36] C. O. Dugger, "THE SYNTHESIS OF ALMINUM NITRIDE SINGLE CRYSTALS", *Mat. Res. Bull.*, 1974, 9, 331–336.

[37] H. P. Maruska, J. J. Tietjen, "THE PREPARATION AND PROPERTIES OF VAPOR-DEPOSITED SINGLE-CRYSTAL-LIKE GaN", *Appl. Phys. Lett.*, 1969, 15, 327–329.

[38] M. Fukuhara, T. Mitsuda, Y. Katsumura, A. Fukawa, "Sinterability and properties of $Ti(N_{1-x}, O_x)$-(V, Ta)C-Ni sintered alloys having a golden colour", *J. Mat. Sci.*, 1985, 20, 710–717.

[39] T. Mills, "THERMODYNAMIC RELATIONS IN THE CHROMIUM- NITROGEN SYSTEM", *J. Less Common Met.*, 1972, 26, 223–234.

[40] T. Mills, "THE SOLUBILITY OF NITROGEN IN SOLID CHROMIUM", *J. Less Common Met.*, 1971, 23, 317–324.

[41] T. Mills, "PRESSURE-TEMPERATURE RELATIONS IN THE CHROMIUM-NITROGEN SYSTEM", *J. Less Common Met.*, 1970, 22, 373–381.

[42] R. H. Wentorf, Jr., "Cubic Form of Boron Nitride", *J. Chem. Phys.*, 1957, 26, 956.

[43] S. Nakano, H. Ikawa, O. Fukunaga, "Synthesis of Cubic Boron Nitride by Decomposition of Magnesium Boron Nitride", *J. Am. Ceram. Soc.*, 1992, 75, 240–243.

[44] S. Nakano, H. Ikawa, O. Fukunaga, "Synthesis of cubic boron nitride using Li_3BN_2, $Sr_3B_2N_4$, and $Ca_3B_2N_4$ as solvent–catalysis", *Diamond and Related Materials*, 1993, 3, 75–82.

[45] T. Takeda, R. Xie, T. Suehiro, N. Hirosaki, "Nitride and oxynitride phosphors for white LEDs: Synthesis, new phosphor discovery, crystal structure", *Prog. Solid State Chem.*, 2018, 51, 41–51.

[46] R. -J. Xie, N. Hirosaki, "Silicon-based oxynitride and nitride phosphors for white LEDs–A review", *Sci. Technol. Adv. Mater.*, 2007, 8, 588–600.

[47] K. Takahashi, R. -J. Xie, N. Hirosaki, "Toward Higher Color Purity and Narrower Emission Band β-sialon:Eu^{2+} by Reducing the Oxygen Concentration", *Electrochem. Solid State Lett.*, 2011, 14, E38–E40.

[48] M. Jansen, H. P. Letschert, "Inorganic yellow-red pigments without toxic metals", *Nature*, 2000, 404, 980–982.

[49] W. A. Harrison, "Electronic Structure and the Properties of Solids", Dover Publications (1980), p50.

[50] R. Aguiar, D. Logvinovich, A. Weidenkaff, A. Rachel, A. Reller, S. G. Ebbinghaus, "The vast colour spectrum of ternary metal oxyniride pigments", *Dyes Pigment.*, 2008, 76, 70–75.

[51] D. Oka. Y. Hirose, T. Fukumura, K. Sasa, S. Ishii, H. Matsuzaki, Y. Sato, Y. Ikuhara, T. Hasegawa, H. Kamisaka, "Possible ferroelectricity in perovskite oxynitride $SrTaO_2N$ epitaxial thin films", *Sci. Rep.*, 2014, 4, 4987–4992.

[52] D. Oka, Y. Hirose, T. Fukumura, T. Hasegawa, "Heteroepitaxial Growth of Perovskite $CaTaO_2N$ Thin Films by Nitrogen Plasma-Assisted Pulsed Laser Deposition", *Cryst. Growth Des.*, 2014, 14, 87–90.

[53] Y. -I. Kim, W. Si, P. M. Woodward, E. Sutter, S. Park, T. Vogt, "Epitaxial Thin-Film Deposition and Dielectric Properties of the Perovskite Oxynitride $BaTaO_2N$", *Chem. Mater.*, 2007, 19, 618–623.

[54] C. L. Paven, R. Benzerga, A. Ferri, D. Fasquelle, V. Laur, L. L. Gendre, F. Marlec, F. Tessier, F. Cheviré, R. Desfeux, S. Saitzek, X. Castel, A. Sharaiha, "Ferroelectric and dielectric study of strontium tantalum based perovskite oxynitride films deposited by reactive rf magnetron sputtering", *Mat. Res. Bull.*, 2017, 96, 126–132.

[55] S. Jacq, C. L. Paven, L. L. Gendre, R. Benzerga, F. Cheviré, F. Tessier, A. Sharaiha, "Deposition and dielectric characterization of strontium and tantalum-based oxide and

oxynitride perovskite thin films", *Solid State Sci.*, 2016, 54, 22–29.

[56] F. Pors, R. Marchand, Y. Laurent, "Structural study of $BaTaO_2N$ and $BaNbO_2N$ oxynitrided perovskites", *Mat. Res. Bull.*, 1988, 23, 1447–1450.

[57] S. J. Clarke, K. A. Hardstone, C. W. Michie, M. J. Rosseinski, "High-temperature synthesis and structures of perovskite and n=1 Ruddlesden-Popper tantalum oxynitrides", *Chem. Mater.*, 2002, 14, 2664–2669.

[58] R. Marchand, F. Pors, Y. Laurent, "NOVELLES PEROVSKITES OXYNITRURES DE STOECHIOMETRIE ABO_2N (A = LANTHANIDE, B = Ti) ET $ABON_2$ (A = LANTHANIDE, B = Ta ou Nb)", *Ann. Chim. Fr.*, 1991, 16, 553–560.

[59] D. Habu, Y. Masubuchi, S. Torii, T. Kamiyama, S. Kikkawa, "Crystal structure study of dielectric oxynitride perovskites $La_{1-x}Sr_xTiO_{2+x}N_{1-x}$ (x = 0, 0.2)", *J. Solid State Chem.*, 2016, 237, 254–257.

[60] G. Tobías, D. -B. Porter, O. I. Lebedev, G. V. Tendeloo, J. R. Carvajal, A. Fuertes, "Anion Ordering and Defect Structure in Ruddlesden-Popper Strontium Niobium Oxynitrides", *Inorg. Chem.*, 2004, 43, 8010–8017.

[61] Tobías Rossell, Gerard; Fuertes Miquel, Amparo, dir.; Canadell Casanova, Enric, dir. Nuevos oxinitruros laminares de niobio y tántalo y sistemas relacionados : síntesis, cristaloquímica y estructura electrónica. Bellaterra: Universitat Autònoma de Barcelona, 2004. ISBN 8468891444. Tesi doctoral - Universitat Autònoma de Barcelona, Facultat de Ciències, Departament de Química, 2004 <https://ddd.uab.cat/record/37099> [Checked: 5 february 2020].

[62] Y. Masubuchi, T. Hata, T. Motohashi, S. Kikkawa, "Synthesis and crystal structure of K_2NiF_4-type novel $Gd_{1+x}Ca_{1-x}AlO_{4-x}N_x$ oxynitrides", *J. Alloy Compds.*, 2014, 582, 823–826.

[63] R. Marchand, Y. Laurent, J. Guyader, P. L'Haridon, P. Verdier, "Nitrides and Oxynitrides: Preparation, Crystal Chemistry and Properties", *J. Eur. Ceram. Soc.*, 1991, 8, 197–213.

[64] F. Chevire, A. Pallu, E. Ray, F. Tessier, "Characterization of Nd_2AlO_3N and Sm_2AlO_3N oxynitrides synthesized by carbothermal reduction and nitridation", *J. Alloy Compds.*, 2011, 509, 5839–5842.

[65] G. Liu, "The synthesis, structure and characterization of $SrMoO_{2.6}{}^{15}N_{0.4}$", *J. Alloy Compds.*, 1992, 187, 145–156.

[66] I. D. Fawcett, K. V. Ramanujachary, M. Greenblatt, "SYNTHESIS, STRUCTURE AND PROPERTIES OF THE OXYNITRIDES $SrWO_2N$ AND $SrMoO_{2.5}N_{0.5}$", *Mat. Res. Bull.*, 1997, 32, 1565–1570.

[67] J. Oró-Solé, L. Clark, W. Bonin, J. P. Attfield, A. Fuertes, "Anion-ordered chains in

a d^1 perovskite oxynitride: NdVO$_2$N", *Chem. Comm.*, 2013, 49, 2430–2432.

[68] T. Bräuniger, T. Müller, A. Pampel, H. -P. Abicht, "Study of Oxygen-Nitrogen Replacement in BaTiO$_3$ by ^{14}N Solid-State Nuclear Magnetic Resonance", *Chem. Mater.*, 2005, 17, 4114–4117.

[69] D. Chen, D. Habu, Y. Masusbuchi, S. Torii, T. Kamiyama, S. Kikkawa, "Partial nitrogen loss in SrTaO$_2$N and LaTiO$_2$N oxynitride perovskites", *Solid State Sci.*, 2016, 54, 2–6.

[70] T. Motohashi, Y. Hamade, Y. Masubuchi, T. Takeda, K. Murai, A. Yoshiasa, S. Kikkawa, "Structural phase transition in the perovskite-type tantalum oxynitride, Ca$_{1-x}$Eu$_x$Ta(O,N)$_3$", *Mat. Res. Bull.*, 2009, 44, 1899–1905.

[71] M. R. Brophy, S. M. Pilgrim, W. A. Schulze, "Synthesis of BaTaO$_2$N Powders Utilizing NH$_3$ Decomposition", *J. Am. Ceram. Soc.*, 2011, 94, 4263–4268.

[72] S. J. Clarke, B. P. Guinot, C. W. Michie, M. J. C. Calmont, M. J. Rosseinsky, "Oxynitride Perovskites: Synthesis and Structures of LaZrO$_2$N, NdTiO$_2$N, and LaTiO$_2$N and Comparison with Oxide Perovskites", *Chem. Mater.*, 2002, 14, 288–297.

[73] P. Antoine, R. Assabaa, P. L'Haridon, R. Marchand, Y. Laurent, "Transport Properties of the New Perovskite-type LaVO$_{3-x}$N$_x$ Oxynitrides", *Mat. Sci. Eng.*, 1989, B5, 43–46.

[74] P. Antoine, R. Marchand, Y. Laurent, "ON THE ELECTRICAL PROPERTIES OF THE PEROVSKITES LnWO$_x$N$_{3-x}$", *Mat. Res. Bull.*, 1988, 23, 953–957.

[75] S. -K. Sun, T. Motohashi, Y. Masubuchi, S. Kikkawa, "Direct Synthesis of SrTaO$_2$N from SrCO$_3$/Ta$_3$N$_5$ involving CO evolution", *J. Eur. Ceram. Soc.*, 2014, 34, 4451–4455.

[76] S. -K. Sun, Y. Masubuchi, T. Motohashi, S. Kikkawa, "Direct Synthesis of nearly single-phase BaTaO$_2$N and CaTaO$_2$N powders", *J. Eur. Ceram. Soc.*, 2015, 35, 3289–3294.

[77] Y. Masubuchi, M. Tadaki, S. Kikkawa, "Synthesis of the Perovskite SrTaO$_2$N Using C$_3$N$_4$ for Both Reduction and Nitridation", *Chem. Lett.*, 2018, 47, 31–33.

[78] Y. -I. Kim, P. M. Woodward, C. -W. Tai, "Characterization of the Structural, Optical, and Dielectric Properties of Oxynitride Perovskites AMO$_2$N(A = Ba, Sr, Ca ; M = Ta, Nb)", *Chem. Mater.*, 2004, 16, 1267–1276.

[79] K. Page, M. W. Stoltzfus, Y. -I. Kim, T. Proffen, P. M. Woodward, A. K. Cheetham, R. Seshadri, "Local atomic ordering in BaTaO$_2$N studied by neutron pair distribution function analysis and density function theory", *Chem. Mater.*, 2007, 19, 4037–4042.

[80] R. L. Withers, Y. Liu, P. M. Woodward, Y. I. Kim, "Structurally frustrated polar nanoregions in BaTaO$_2$N and the relationship between its high dielectric permittivity and that of BaTiO$_3$", *App. Phys. Lett.*, 2008, 92, 102907.

[81] B. Ravel, Y. I. Kim, P. M. Woodward, C. M. Fang, "Role of local disorder in the

dielectric response of BaTaO$_2$N", *Phys. Rev. B*, 2006, 73, 184121.

[82] V. F. Sears, "Neutron scattering lengths and cross sections", *Neutron News*, 1992, 3, 26–37.

[83] Y. -R. Zhang, T. Motohashi, Y. Masubuchi, S. Kikkawa, "Local anionic ordering and anisotropic displacement in dielectric perovskite SrTaO$_2$N", *J. Ceram. Soc. Jpn.*, 2011, 119, 581–586.

[84] M. Yang, J. Oró-Solé, J. A. Rodgers, A. B. Jorge, A. Fuertes, J. P. Attfield, "Anion order in perovskite oxynitrides", *Nat. Chem.*, 2011, 3, 47–52.

[85] J. P. Attfield, "Principles and Applications of Anion Order in Solid Oxynitrides", *Cryst. Growth Des.*, 2013, 13, 4623–4629.

[86] S. H. Porter, X. Huang, P. M. Woodward, "Study of Anion Order/Disorder in RTaN$_2$O (R = La, Ce, Pr) Perovskite Nitride Oxides", *Cryst. Growth Des.*, 2014, 14, 117–125.

[87] K. Tatsumi, R. Hoffmann, "Bent *Cis* d^0 MoO$_2$$^{2+}$ vs. Linear *Trans* d^{0}f^0 UO$_2$$^{2+}$: A Significant Role for Nonvalence 6p Orbitals in Uranyl", *Inorg. Chem.*, 1980, 19, 2656–2658.

[88] Y. Hinuma, H. Moriwake, Y. Zhang, T. Motohashi, S. Kikkawa, I. Tanaka, "First principles study on relaxor-type ferroelectric behavior without chemical inhomogeneity in BaTaO$_2$N and SrTaO$_2$N", *Chem. Mater.*, 2012, 24, 4343–4349.

[89] H. Wolff, R. Dronskowski, "First-Principles and Molecular-Dynamics Study of Structure and Bonding in Perovskite-Type Oxynitrides *AB*O$_2$N (*A* = Ca, Sr, Ba; *B* = Ta, Nb)", *J. Comput. Chem.*, 2008, 29, 2260–2267.

[90] Z. Shen, M. Nygren, "Microstructural Prototyping of Ceramics by Kinetic Engineering: Applications of Spark Plasma Sintering", *Chem. Rec.*, 2005, 5, 173–184.

[91] "*Sintering of Ceramics*", M. N. Rahaman (Ed.), CRC Press, Florida (2008) pp. 46, 67.

[92] R. M. German, P. Suri, S. J. Park, "Review: liquid phase sintering", *J. Mater. Sci.*, 2009, 44, 1–39.

[93] G. R. Terwilliger, F.F. Lange, "Pressureless sintering of Si$_3$N$_4$", *J. Mat. Sci.*, 1975, 10, 1169–1174.

[94] E. B. Pickens, R. W. Trice, "Pressureless sintering of silicon nitride/boron nitride laminate composites", *J. Mater. Sci.*, 2005, 40, 2101–2103.

[95] F. L. Riley, "Silicon Nitride and Related Materials", *J. Am. Ceram. Soc.*, 2000, 83, 245–265.

[96] E. A. Maguire, T. M. Hartnett, R. L. Gentilman, "Method of Producing Aluminum Oxynitride Having Improved Optical Characteristics", United States Patent Number

4686070 (1984).

[97] R. L. Gentilman, E. A. Maguire, L. E. Dolhert, "Transparent Aluminum Oxynitride and Method of Manufacture", United States Patent Number 4520116 (1985).

[98] I. U. Kim, V. L. Richards, "High-Temperature Electrical Conductivity of Aluminum Oxynitride Spinel", *J. Am. Ceram. Soc.*, 1985, 68, C210–212.

[99] N. D. Corbin, "Aluminum Oxynitride Spinel: A Review", *J. Eur. Ceram. Soc.*, 1989, 5, 143–154.

[100] J. W. McCauley, P. Pater, M. Chen, G. Glide, E. Strassburger, B. Paliwal, K. T. Ramesh, D. P. Dandekar, "AlON: A brief history of its emergence and evolution", *J. Eur. Ceram. Soc.*, 2009, 29, 223–236.

[101] G. X. Cao, R. Metselaar, "α'-Sialon Ceramics: A Review", *Chem. Mater.*, 1991, 3, 242–252.

[102] S. Bandyopadhyay, G. Rixecker, F. Aldinger, S. Pal, K. Mukherjee, H. S. Maiti, "Effect of Reaction Parameters on γ-AlON Formation from Al_2O_3 and AlN", *J. Am. Ceram. Soc.*, 2002, 85, 1010–1012.

[103] K. Komeya, H. Inoue, A. Tsuge, "Effect of Various Additives on Sintering of Aluminum Nitride", *Yogyo-Kyokai-Shi*, 1981, 89, 330–336.

[104] J. Cheng, D. Agrawal, R. Roy, "Microwave synthesis of aluminum oxynitride", *J. Mat., Sci. Lett.*, 1999, 18, 1989–1990.

[105] R. W. Trice, J. W. Halloran, "Investigation of the Physical and Mechanical Properties of Hot-Pressed Boron Nitride/Oxide Ceramic Composites", *J. Am. Ceram. Soc.*, 1999, 82, 2563–2565.

[106] M. Mitomo, "Pressure sintering of Si_3N_4", *J. Mater. Sci.*, 1976, 11, 1103–1107.

[107] G. E. Gazza, "Hot-Pressed Si_3N_4", *J. Am. Ceram. Soc.*, 1973, 56, 662.

[108] G. G. Deeley, J. M. Herbert, N. C. Moore, "DENSE SILICON NITRIDE", *Powder Metallurgy*, 1961, 4, 145–151.

[109] X. Su, P. Wang, W. Chen, B. Zhu, Y. Cheng, D. Yan, "Translucent α-Sialon Ceramics by Hot Pressing", *J. Am. Ceram. Soc.*, 2004, 87, 730–732.

[110] H. F. Priest, G. L. Priest, G. E. Gazza, "Sintering of Si_3N_4 Under High Nitrogen Pressure", *J. Am. Ceram. Soc.*, 1977, 60, 81.

[111] I. Iturriza, J. Echeberria, I. Gutierrez, F. Castro, "Densification of silicon nitride ceramics under sinter-HIP conditions", *J. Mat. Sci.*, 1990, 25, 2539–2548.

[112] T. Ekstöm, P. O. Olsson, "β-Sialon Ceramics Prepared at 1700 °C by Hot Isostatic Pressing", *J. Am. Ceram. Soc.*, 1989, 72, 1722–1724.

[113] T. Ekstöm, P. O. Olsson, "O'-Sialon Ceramics Prepared by Hot Isostatic Pressing", *J. Eur. Ceram. Soc.*, 1993, 12, 165–176.

[114] I. Tanaka, G. Pezzotti, T. Okamoto, Y. Miyamoto, M. Koizumi, "Hot Isostatic Press Sintering and Properties of Silicon Nitride without Additives", *J. Am. Ceram. Soc.*, 1989, 72, 1656–1560.

[115] M. J. Li, L. M. Zhang, Q. Shen, T. Li, M. Q. Yu, "Microstructure and properties of spark plasma sintered AlN ceramics", *J. Mater. Sci.*, 2006, 41, 7934–7938.

[116] D. Salamon, Z. Shen, P. Pavol, Sajgalik, "Rapid formation of α-sialon during spark plasma sintering: Its origin and implications", *J. Eur. Ceram. Soc.*, 2007, 27, 2541–2547.

[117] H. Nakajima, M. Koiwa, "Duffusion in Titanium", *ISIJ International*, 1991, 31, 757–766.

[118] K. Hirao, T. Nagaoka, M. E. Brito, S. Kanzaki, "Microstructure Control of Silicon Nitride by Seeding with Rodlike β-Silicon Nitride Particles", *J. Am. Ceram. Soc.*, 1994, 77, 1857–1862.

[119] A. Tsuge, K. Nishida, M. Komatsu, "Effect of Crystallizing the Grain-Boundary Glass Phase of the High-Temperature Strength of Hot-Pressed Si_3N_4 Containing Y_2O_3", *J. Am. Ceram. Soc.*, 1975, 58, 323–326.

[120] A. V. Virkar, "Thermodynamic and Kinetic Effects of Oxygen Removal on the Thermal Conductivity of Aluminum Nitride", *J. Am. Ceram. Soc.*, 1989, 72, 2031–2042.

[121] D. Klimm, "*Handbook of Solid State Chemistry*", Vol. 2, R. Dronskowski, S. Kikkawa, A. Stein (Eds.), Wiley-VCH, Weinheim, New York (2017).

[122] H. Yamane, M. Shimada, S. J. Clarke, F. J. DiSalvo, "Preparation of GaN Single Crystals Using a Na Flux", *Chem. Mater.*, 1997, 9, 413–416.

[123] H. Yamane, F. J. DiSalvo, "Sodium flux synthesis of nitrides", *Prog. Solid State Chem.*, 2018, 51, 27–40.

[124] G. Wang, J. Jian, W. Yuan, X. Chen, "Growth of GaN Single Crystals Using Ca-Li_3N Composite Flux", *Cryst. Growth Des.*, 2006, 6, 1157–1160.

[125] M. Kagamida, H. Kanda, M. Akaishi, A. Nukui, T. Osawa, S. Yamaok, "Crystal growth of cubic boron nitride using Li_3BN_2 solvent under high temperature and pressure", *J. Cryst. Growth*, 1989, 94, 261–269.

[126] Y. -R. Zhang, T. Motohashi, Y. Masubuchi, S. Kikkawa, "Sintering and Dielectric Properties of Perovskite $SrTaO_2N$ Ceramics" *J. Eur. Ceram. Soc.*, 2012, 32, 1269–1274.

[127] S. -K. Sun, Y. -R. Zhang, Y. Masubuchi, T. Motohashi, S. Kikkawa, "Additive sintering, postannealing, and dielectric properties of $SrTaO_2N$", *J. Am. Ceram. Soc.*, 2014, 97, 1023–1027.

[128] S. Kikkawa, S. -K. Sun, Y. Masubuchi, Y. Nagamine, T. Shibahara, "Ferroelectric response induced by *cis*-type anion ordering in $SrTaO_2N$ oxynitride perovskite", *Chem. Mater.*, 2016, 28, 1312–1317.

[129] Y. -R. Zhang, Y. Masubuchi, T. Motohashi, S. Kikkawa, K. Hirota, "Hot isostatic press sintering and dielectric properties of $SrTaO_2N$ ceramics", *Ceram. Int.*, 2013, 39, 3377–3380.

[130] A. Hosono, Y. Masubuchi, S. Kikkawa, "Sintering behavior of dielectric $SrTaO_2N$ under high pressure of nitrogen", *Ceram. Int.*, 2017, 43, 2737–2742.

[131] Y. Masubuchi, F. Kawamura, T. Taniguchi, S. Kikkawa, "High pressure densification and dielectric properties of perovskite-type oxynitride $SrTaO_2N$", *J. Eur. Ceram. Soc.*, 2015, 35, 1191–1197.

Chapter 2

Reinvestigation of the Crystal Structure of BaTaO₂N

2-1. Introduction

Space group of $BaTaO_2N$ has been reported to be centrosymmetric $Pm\bar{3}m$ ($a =$ 0.41128 nm) based on powder neutron diffraction. [1,2] On the other hand, some deviations from centrosymmetric structure to form one-dimensional PNRs were suggested by TEM, EXAFS, and neutron pair distribution functions. [3-5] Furthermore, DFT calculations in combination with molecular dynamic calculations indicated that *cis*-type anisotropic anion configuration in TaO_4N_2 octahedra are favored in $BaTaO_2N$. [6] In such structural model, three-dimensional polar clockwise and anti-clockwise coil-like helical Ta-N-Ta-N chains in various directions and lengths are believed to behave as PNRs to originate relaxor-like ferroelectric properties. [6] Another first principle study indicated that crystal structure with *Pnma* space group is favorable among $Pm\bar{3}m$, *I4/mcm*, and *Pnma* for $BaTaO_2N$ and furtherly optimized structure is non-centrosymmetric orthorhombic *Pmc*2₁ with *cis*-type nitrogen configuration. [7] By summing up the above reports, tiny regions with non-centrosymmetric structure composed of polar Ta-N-Ta-N chains may be dispersed over $Pm\bar{3}m$ average structure in $BaTaO_2N$. Analysis of a powder diffraction profile of $BaTaO_2N$ considering the presence of *Pmc*2₁ region will provide an important suggestion regarding the presence of non-centrosymmetric parts in average

centrosymmetric structure.

In the present chapter, secondary harmonic generation (SHG) measurement was conducted to obtain several clues indicating the breaking of centrosymmetry, which is consistent with the presence of ferroelectricity. Additionally, Rietveld fitting of the powder neutron diffraction profile of BaTaO$_2$N was also performed based on both of $Pm\overline{3}m$ and $Pmc2_1$ structural models.

2-2. Experimental

Reddish powder of BaTaO$_2$N was obtained by the ammonolysis of the mixture of BaCO$_3$ and Ta$_2$O$_5$ (99.9%, FUJIFILM Wako Pure Chemical) with a molar ratio of 1.03 : 1 as mentioned in the previous publication. [8] Both of the starting materials were mixed in an agate mortar with an ethanol. The mixture on an alumina boat was heated under flowing ammonia (99.9%, Sumitomo Seika) with a total duration at 930 °C of 60 h. Starting with slightly Ba-rich composition was effective to avoid the formation of Ta$_3$N$_5$ impurity probably due to a slight loss of BaO by the reaction with alumina. Chemical composition was studied with X-ray fluorescent spectroscopy (XRF, SEA6000VX-SII, Hitachi) for Ba and Ta molar ratios and the combustion analysis for oxygen and nitrogen contents (EMGA-620W, Horiba) using Gd$_2$O$_3$ (99.9%, FUJIFILM Wako Pure Chemical)

after calcination at 1000 °C and Si_3N_4 (JCRM R004, Ceramic Society of Japan) as references. The crystalline phase and composition of the synthesized powder were confirmed to be pure $BaTaO_2N$.

A spectroscopic analysis of secondary harmonic generation (SHG) by the $BaTaO_2N$ aggregates was performed to elucidate the presence of a non-centrosymmetric structure. The excitation source was an acousto-optically Q-switched Nd:YAG laser (T40-X30S-106Q, Spectra Physics) with a 1064 nm wavelength, an average power of 0.6 mW and a pulse width of 30 ns at a repetition rate of 4 kHz. The laser beam was focused by a lens with a 150 mm focal length on the surface of an aggregate of as-prepared $BaTaO_2N$ powder or microcrystals (prepared with 46 mol% $BaCN_2$ flux by keeping at 910 °C for 30 min and subsequent cooling at 1.8 °C/h. More detail is explained in the crystal growth section of **Chapter 5**). This technique purposely used a low excitation power to avoid thermal decomposition of the $BaTaO_2N$ during irradiation and to allow data accumulation over a long time span of 4 h.

Powder neutron diffraction was performed on approximately 10 g of $BaTaO_2N$ powder obtained by the ammonolysis. Neutron diffraction data was obtained at beamline BL20 (iMATERIA) at the Japan Proton Accelerator Research Complex (J-PARC) and analyzed using the *Z*-Rietveld software (Windows Ver. 1.0.2.0). Preliminary assessment

of XRD profile fitting was conducted for the data obtained with a Cu Kα radiation over

an angular range $2\theta = 10 - 120°$ with a scanning speed of 0.2°/min using either structural

models of $Pm\overline{3}m$ or $Pmc2_1$ space groups. [1,7,9] Lattice parameters were calculated using

a Rietveld program RIETAN-FP. [10]

2-3. Results and discussion

SHG assessments were performed for $BaTaO_2N$ aggregates to confirm the

presence of non-centrosymmetric structure. In these trials, a 1064 nm laser beam with a

diameter of approximately 100 μm was irradiated to the surface of the $BaTaO_2N$ powder

at 30 °C, to avoid the partial loss of nitrogen from the crystals as a result of laser heating.

In response, a weak secondary harmonic wave at 532 nm was observed (**Fig. 2-1(a)**),

confirming the presence of non-centrosymmetric regions in the $BaTaO_2N$ crystals. This

result demonstrates that local symmetry was disturbed by the co-presence of oxygen and

nitrogen atoms in the reported centrosymmetric $Pm\overline{3}m$ crystal structure. SHG was

observed on both of the as-prepared $BaTaO_2N$ powder and microcrystals.

Preliminary assessments of the powder XRD profile fitting of $BaTaO_2N$ are

performed using Rietveld refinement. Two types of structural models of $BaTaO_2N$

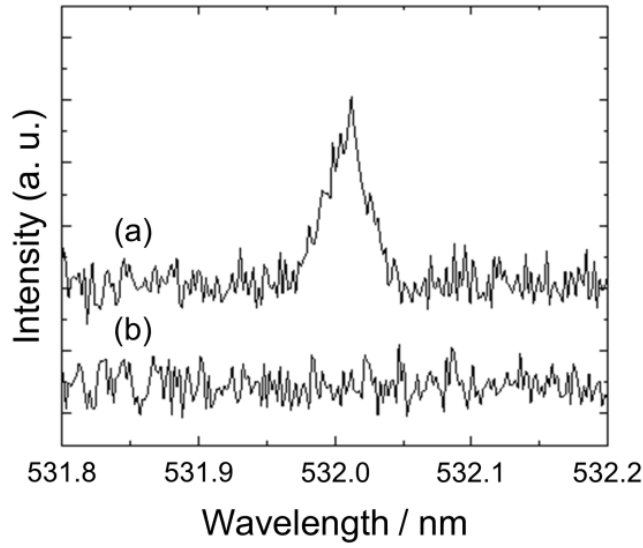perovskite were proposed according to the powder neutron diffraction and DFT

Fig. 2-1. SHG spectra acquired from **(a)** BaTaO$_2$N microcrystal aggregate and **(b)** reference amorphous silicon dioxide powder at room temperature.

structure optimizations. [1,7] One is centrosymmetric, cubic $Pm\bar{3}m$ model [1] and another one is non-centrosymmetric orthorhombic $Pmc2_1$ space group model with the *cis*-type nitrogen configurations in TaO$_4$N$_2$ octahedra. [7] In the present study, structural model of $Pmc2_1$ phase was constructed by using a data for CaTaO$_2$N with $Pmc2_1$ space group suggested in Ref. 9. Each structure model and structural data are presented in **Fig. 2-2** and **Table 2-1**, respectively. It should be noted that only the lattice parameters were refined in this process. Neutron diffraction profile fitting was subsequently performed assuming that the BaTaO$_2$N powder is a mixture of $Pm\bar{3}m$ and $Pmc2_1$ phases. The weight ratios of these two phases were changed to improve the fitting convergence. The variance values (s^2) against the phase ratios are plotted in **Fig. 2-3** and the minimum value was

45

Table 2-1. Structural parameters of BaTaO$_2$N calculated with powder XRD profile.

Space group			$Pm\bar{3}m$		
a / Å			4.11144(10)		
α / °			90		
V / Å^3			69.4995(28)		
Z			1		
R_{wp} / %			8.6		
s			1.3		

Atom	Site	x	y	z	Occ.
Ba	1a	0.00000	0.00000	0.00000	1.000
Ta	1b	0.50000	0.50000	0.50000	1.000
O	3c	0.50000	0.50000	0.00000	0.667
N	3c	0.50000	0.50000	0.00000	0.333

Space group			$Pmc2_1$		
a / Å			8.21719(30)		
b / Å			5.81897(23)		
c / Å			5.81404(29)		
α / °			90		
β / °			90		
γ / °			90		
V / Å^3			278.0017(204)		
Z			4		
R_{wp}			7.8		
s			1.2		

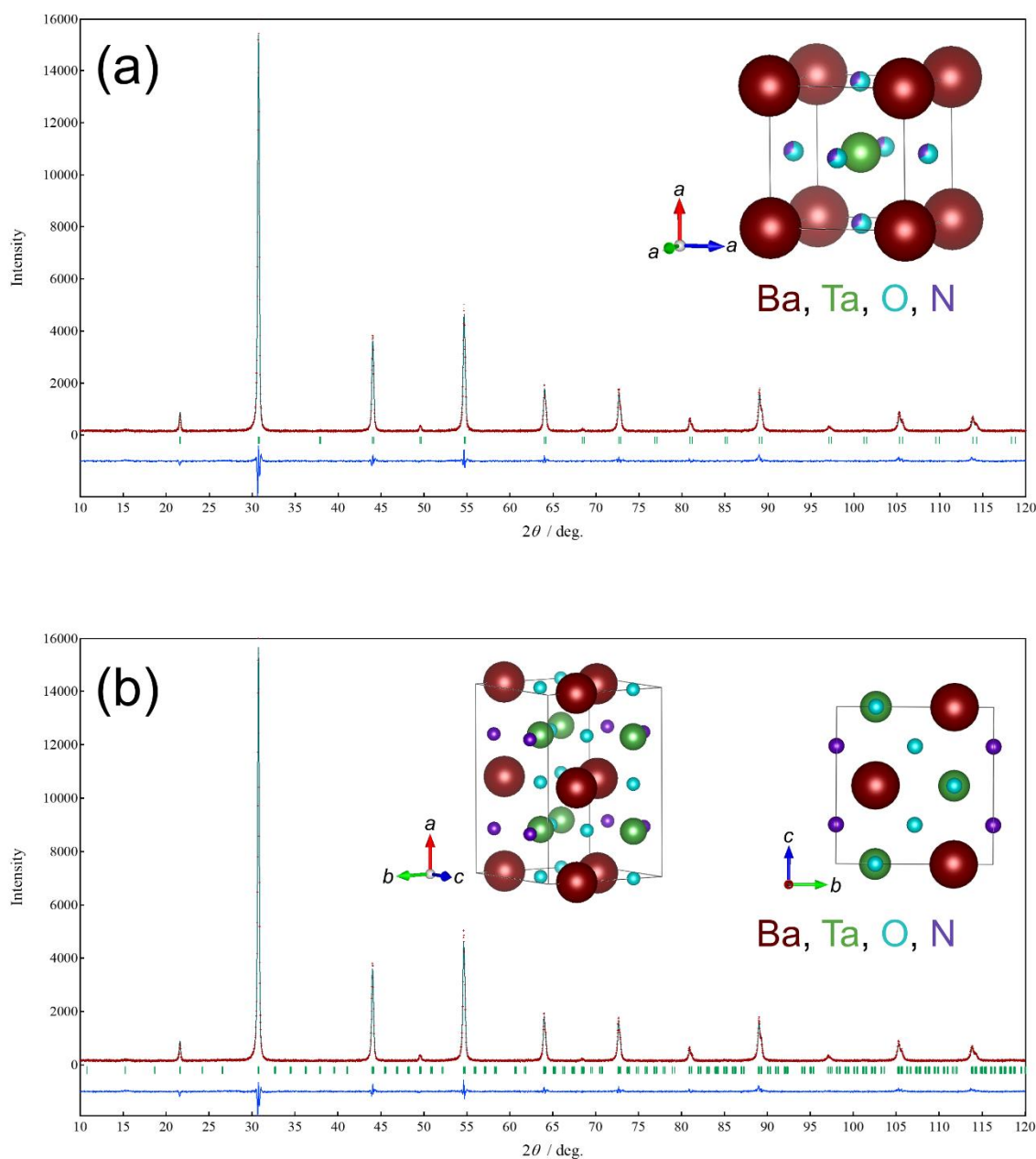| Atom	Site	x	y	z	Occ.
Ba	2a	0.00000	0.25010	0.50000	1.000
Ba	2b	0.50000	0.75000	1.00000	1.000
Ta	4c	0.75000	0.75000	0.50000	1.000
O	2a	0.00000	0.75000	0.50000	1.000
O	2b	0.50000	0.25000	0.00000	1.000
O	4c	0.75000	0.50000	0.25000	1.000
N	4c	0.75000	1.00000	0.25000	1.000

Fig. 2-2. Rietveld profile fitting results of powder XRD data of BaTaO$_2$N calculated with **(a)** $Pm\bar{3}m$ and **(b)** $Pmc2_1$ space group with *cis*-type anion configuration models. Red dots, green line, green vertical bars, and blue lines are observed and calculated intensity, Bragg positions, and the residual errors, respectively. The insets are crystal structure models drawn using the VESTA software package. [11] Brown, green, blue, and purple balls indicate Ba, Ta, O, and N, respectively.
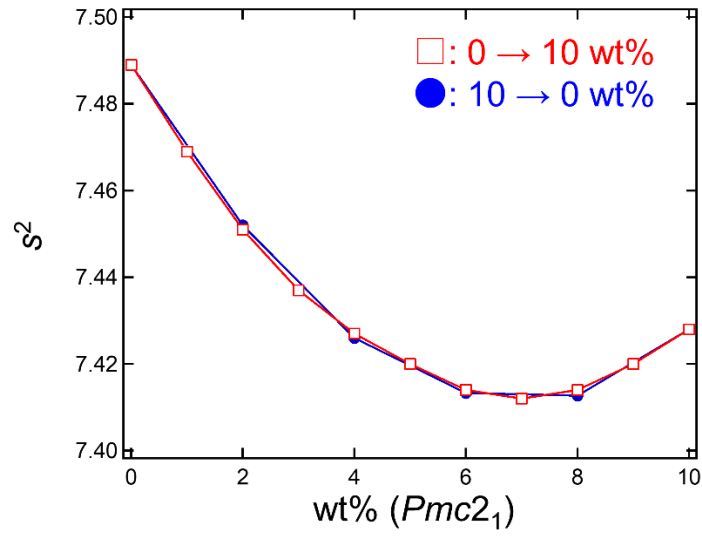
47

Fig. 2-3. Variance values (s^2) of the profile fitting as functions of the weight ratio of BaTaO$_2$N with $Pmc2_1$ space group. The content of $Pmc2_1$ phase was changed from 0 to 10 wt% and *vice versa*.
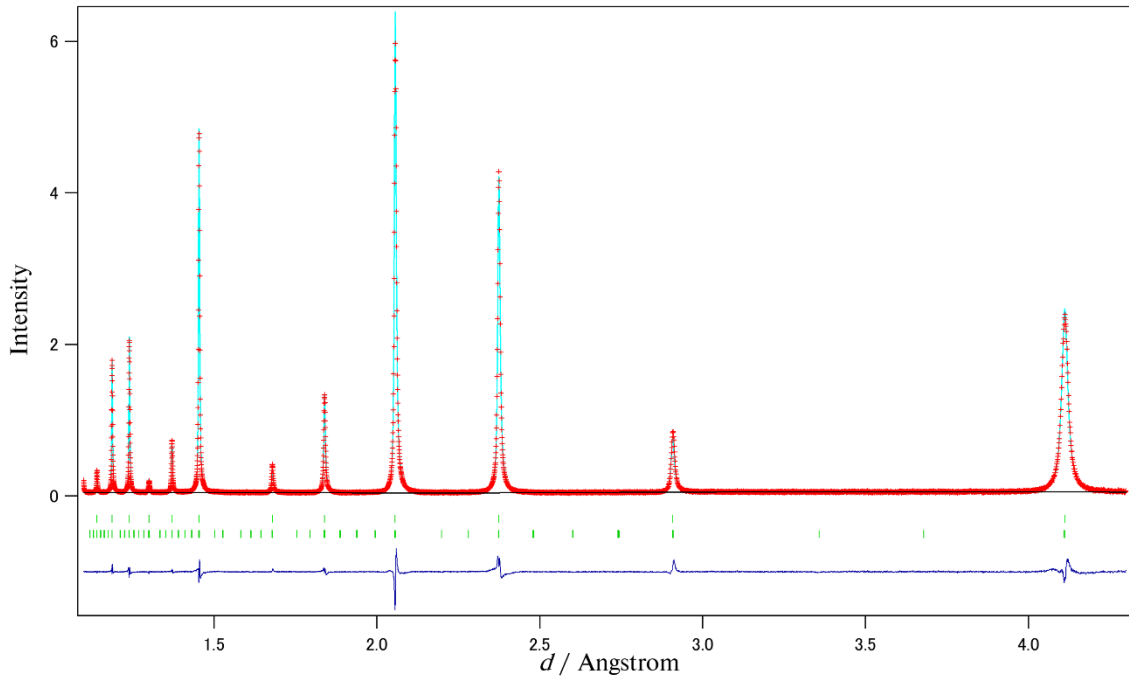

Fig. 2-4. Rietveld refinement result of the powder neutron profile for BaTaO$_2$N powder. The weight ratio of $Pm\bar{3}m$ and $Pmc2_1$ is 93 : 7. Red crosses and light blue line indicate the observed intensity and simulated profile, respectively. Upper and lower green vertical bars indicate Bragg positions for $Pm\bar{3}m$ and $Pmc2_1$ models, respectively.

48

obtained with 7 wt% of $Pmc2_1$ phase. The fitted profile with 7 wt% of $Pmc2_1$ phase is shown in **Fig. 2-4** and such non-centrosymmetric regions are considered to behave as PNRs without compositional inhomogeneity. The real structure of $BaTaO_2N$ may belong to polar $Pmc2_1$ space group, but the connections of most of the polar *cis*-type Ta-N-Ta-N linkage can be partly disturbed in $BaTaO_2N$, only to be detected as $Pm\bar{3}m$ "average" structure. This is the reason why the apparent structure of $BaTaO_2N$ had been identified as $Pm\bar{3}m$ space group in the diffraction measurements.

2-4. Conclusion

The presence of non-centrosymmetric region in $BaTaO_2N$ was confirmed by SHG measurements. Better profile fitting was achieved by assuming that $BaTaO_2N$ powder is a mixture of 93 wt% of $Pm\bar{3}m$ and 7 wt% of $Pmc2_1$ phases, compared with the calculation assuming the single phase of $Pm\bar{3}m$ space group. This indicates that the trace of polar regions was detected in powder neutron diffraction, which is consistent with the emergence of SHG. However, most part is detected as centrosymmetric average structure in diffraction studies, as in the previous reports.

Chapter 2 References

[1] F. Pors, R. Marchand, Y. Laurent, "Structural study of $BaTaO_2N$ and $BaNbO_2N$ oxynitrided perovskites", *Mat. Res. Bull.*, 1988, 23, 1447–1450.

[2] Y. -I. Kim, P. M. Woodward, C. -W. Tai, "Characterization of the Structural, Optical, and Dielectric Properties of Oxynitride Perovskites AMO_2N(A = Ba, Sr, Ca ; M = Ta, Nb)", *Chem. Mater.*, 2004, 16, 1267–1276.

[3] K. Page, M. Stoltzfus, Y. -I, Kim, T. Proffen, P. M. Woodward, A. K. Cheetham, R. Seshadri, "Local atomic ordering in $BaTaO_2N$ studied by neutron pair distribution function analysis and density function theory", *Chem. Mater.*, 2007, 19, 4037–4042.

[4] R. L. Withers, Y. Liu, P. M. Woodward, Y. I. Kim, "Structurally frustrated polar nanoregions in $BaTaO_2N$ and the relationship between its high dielectric permittivity and that of $BaTiO_3$", *App. Phys. Lett.*, 2008, 92, 102907.

[5] B. Ravel, Y. I. Kim, P. M. Woodward, C. M. Fang, "Role of local disorder in the dielectric response of $BaTaO_2N$", *Phys. Rev. B*, 2006, 73, 184121.

[6] Y. Hinuma, H. Moriwake, Y. Zhang, T. Motohashi, S. Kikkawa, I. Tanaka, "First principles study on relaxor-type ferroelectric behavior without chemical inhomogeneity in $BaTaO_2N$ and $SrTaO_2N$", *Chem. Mater.*, 2012, 24, 4343–4349.

[7] H. Wolff, R. Dronskowski, "First-Principles and Mollecular-Dynamics Study of Structure and Bonding in Perovskite-Type Oxynitrides ABO_2N (A = Ca, Sr, Ba; B = Ta, Nb)", *J. Comput. Chem.*, 2008, 29, 2260–2267.

[8] M. R. Brophy, S. M. Pilgrim, W. A. Schulze, "Synthesis of $BaTaO_2N$ Powders Utilizing NH_3 Decomposition", *J. Am. Ceram. Soc.*, 2011, 94, 4263–4268.

[9] S. H. Porter, Z. Huang, P. M. Woodward, "Study of Anion Order/Disorder in $RTaN_2O$ (R = La, Ce, Pr) Perovskite Nitride Oxides", *Cryst. Growth Des.*, 2014, 14, 117–125.

[10] F. Izumi, K. Momma, "Three-dimensional visualization in powder diffraction", *Solid State Phenom.*, 2007, 130, 15–20.

[11] K. Momma, F. Izumi, "VESTA 3 for three-dimensional visualization of crystal, volumetric and morphology data", *J. Appl. Crystallogr.*, 2011, 44, 1272–1276.

Chapter 3

High Temperature Sintering, Post-ammonolysis, and Electrical Properties of Perovskite-type BaTaO₂N

3-1. Introduction

Oxynitride perovskites such as $SrTaO_2N$ and $BaTaO_2N$ are promising lead-free

dielectric materials. [1-4] As mentioned in the last chapter, a clear SHG signal and neutron

diffraction profile fitting for $BaTaO_2N$ powder indicate the presence of non-

centrosymmetric structure. Further study on this compound is necessary to disclose more

detail of its dielectricity especially ferroelectric behaviors. However, fabrication of high-

density oxynitride ceramics keeping stoichiometric composition is known to be difficult

in general. Sintering of $SrTaO_2N$ was performed by high temperature process [2,3] and

its thermal behavior was studied in a nitrogen atmosphere in relation to its sintering

conditions. [2,5] $SrTaO_2N$ begins releasing approximately 30% of its nitrogen at 950 °C

even under nitrogen atmosphere to form a nitrogen deficient perovskite $SrTaO_2N_{0.7}$ and

loses a trace amount of SrO during sintering at 1400 °C. [2,3,5] Addition of a small

amount of $SrCO_3$ was necessary to maintain the perovskite-type phase of $SrTaO_2N_{0.7}$

during the high temperature sintering. $SrTaO_2N$ changes from orange insulator to black

semiconductor during sintering due to a partial reduction of Ta^{5+}. [2,3,5] Post-annealing

of $SrTaO_2N_{0.7}$ ceramics in NH_3 flow is effective to recover the original nitrogen contents

of SrTaO$_2$N. The sintered SrTaO$_2$N$_{0.7}$ ceramics with RD $\leq$ 84% completely recovered their nitrogen contents and electrically insulating property after annealing. The post-annealed SrTaO$_2$N ceramics with RD = 83.3% had high relative dielectric constant (ε_r) of 450 with a low dielectric loss of less than 0.1 at 100 Hz, almost independent of frequency and temperature. [2] However, the interior of the well-sintered ceramics with RD = 95.1% exhibited semiconducting behavior and a black color, even after post-ammonolysis. [2,4]

Atomic force microscopy (AFM)-based technique has enabled to evaluate electrical properties of nano-sized materials. Piezoresponse force microscopy (PFM) has been used to explore nanoscale ferro/piezoelectric phenomena over the past two decades. The imaging mechanism of PFM is based on the detection of the electromechanical response between a small tip and a ferroelectric surface. [6,7] Piezoresponse as well as ferroelectric hysteresis were observed for the clacked off surface of the dense SrTaO$_2$N ceramics with RD > 95% in a thickness of approximately 8 μm, although current leakage was inevitable at high voltages. [4]

Higher relative dielectric constant values of BaTaO$_2$N compared to SrTaO$_2$N are suggested by the investigations on their porous bulks with RD $\approx$ 45% [1], but further detail is still unclear. The thermal behavior and sinterability of the BaTaO$_2$N should be investigated, to obtain densified ceramics in order to investigate its dielectric properties.

In the present chapter, thermal stability of $BaTaO_2N$ powder in both He and N_2 atmospheres is investigated using TG-MS in comparison with that of $SrTaO_2N$. $BaTaO_2N$ mixed with a small amount of $BaCO_3$ was sintered in nitrogen atmosphere and post-ammonolysis was then applied to recover the stoichiometric composition. The ceramics were characterized in their crystalline phases, microstructure, and dielectric properties. PFM measurements were also applied on the thin specimens sliced from the dense $BaTaO_2N$ ceramics with RD > 90% after their post ammonolysis. The piezoelectric behaviors are discussed in relation to their chemical compositions and microstructure.

3-2. Experimental

Ceramics fabrication

Phase-pure $BaTaO_2N$ perovskite powder was synthesized as mentioned in **Chapter 2**. X-ray diffraction (XRD) with Cu Kα radiation at 40 kV and 40 mA (Ultima IV, Rigaku) was used for phase identification. The data were collected over the 2θ angular range of 10 – 90°, with each step of 0.02° and scanning speed of 10°/min.

Thermal stability of $BaTaO_2N$ powder was studied by using TG-DTA-MS (STA2500-QMS403 Aeolos, Netzsch) in helium or nitrogen flow at 200 mL/min. The sample chamber was evacuated to 10 Pa prior to the measurements. Approximately 40

mg of the sample was heated in an alumina crucible to 1400 °C at a rate of 20 or 5 °C/min.

Excess $BaCO_3$ powder (2.5 – 5.0 wt%) was mixed with the reddish $BaTaO_2N$

powder product as in the previous reports of the sintering of $SrTaO_2N$. [2,3] Mixtures

containing different amounts of $BaCO_3$ additive were uniaxially pressed into pellets with

a diameter of 5.9 mm at 46 MPa and then cold isostatically pressed at 150 MPa. These

green-compacts were placed in a BN crucible and sintered at 1350, 1400, or 1450 °C for

different holding times under 0.2 MPa of N_2 gas pressure (> 99.999% purity, AIR WATER

Inc.) in a carbon furnace (High Multi 5000, Fuji Dempa Kogyo). The heating rates were

20 °C/min below 1200 °C and 10 °C/min at higher temperature. After holding at the

desired temperature, the samples were cooled down to room temperature in the furnace.

After cooling, the ceramic surfaces were polished with a sandpaper with SiC particle size

of 2 – 3 μm, and the relative densities were measured using a water vacuum penetration

technique in combination with Archimedes method. [2] The crystalline phases present on

the polished surface were studied using XRD. The $BaTaO_2N$ ceramics lost approximately

15 at% of nitrogen and changed to black $BaTaO_2N_{0.85}$ during sintering. The color change

was assumed to be induced by the partial reduction of Ta^{5+} in $BaTaO_2N$ because of its

partial loss of nitrogen, as is observed in $SrTaO_2N$. [2,3,5] The black ceramics were

electrically semiconducting and did not show dielectric properties.

The as-sintered $BaTaO_2N_{0.85}$ ceramics were post-annealed at 1000 – 1030 °C in an NH_3 flow of 100 mL/min. The fracture surfaces of ceramics sintered at 1350 and 1400 °C for 3 h was studied by scanning electron microscope (SEM, JSM-6390 LVS, JEOL) and field emission SEM (FE-SEM, JSM-6500F, JEOL).

Chemical analyses were conducted for each fabrication process. X-ray fluorescent spectroscopy (XRF, SEA6000VX-SII, Hitachi) was used for Ba and Ta molar ratios, and the oxygen and nitrogen contents were determined by combustion oxygen/nitrogen analyzer (EMGA-620W, Horiba) using Gd_2O_3 (99.9%, FUJIFILM Wako Pure Chemical) after calcination at 1000 °C and Si_3N_4 (JCRM R004, Ceramic Society of Japan) as references.

Electrical property measurements

Ag pasted electrodes (4922N, DuPont) were applied on the surfaces of the fully-annealed $BaTaO_2N$ ceramics with RD = 73.0 and 59.5%. Dielectric behaviors were investigated with an LCR meter (4274A, Hewlett Packard) in the frequency range of 10^2 – 10^5 Hz and with an impedance/material analyzer (E4991A / 16453A, Agilent) in the range of 3×10^6 – 10^8 Hz at temperatures of 30 – 150 °C. Effects of electrodes had been confirmed to be insignificant between the pasted Ag and the sputter-deposited Pt on the sintered pellets with RD ~ 75% in the previous study. [3]

PFM measurements were conducted on the post-annealed $BaTaO_2N$ ceramics with RD of approximately 94.6%, which was obtained by a sintering at 1400 °C for 8 h. The sample recovered its original red color of stoichiometric $BaTaO_2N$ on its outermost surface from black by the post-ammonolysis in NH_3. The post-annealed ceramics was sliced into two pieces by a diamond cutter. The specimens were fixed on a conductive ceramic block and then polished by a lapping sheet (Lapping Film, 3M) in order to reduce their thickness to less than 20 μm, which is appropriate to obtain a sufficient electrical field for observing a piezoresponse. Appearance of the polished slice was observed using an optical microscope (SZ61, Olympus). Microstructure of the specimens was observed by SEM (JSM-7001F, JEOL) and STEM (Titan G2, FEI). The STEM sample was prepared using a focused ion beam (FIB) of gallium (Nova200i NanoLab, FEI).

The conductive ceramic block with the lapped $BaTaO_2N$ specimen was attached on a 10×10 mm^2 copper plate of AFM apparatus observation by a conductive silver paste (DOTITE, Fujikura). Both AFM and PFM measurements were performed by using a scanning microscope (E-sweep with NanoNavi Probe Station, SII Nano Technology). A Rh-coated silicon cantilever (Si-DF3-R (100), SII Nano Technology) with a stiffness of 1.7 N/m was employed for the measurement in a resonance frequency of 27 kHz. PFM measurement was performed at the driving AC electric field frequency of 5 kHz and the

applied AC field amplitude of 1 – 10 V. The domain poling was performed by applying

biases of -10 and 10 V to each measurement area.

3-3. Results and discussion

Thermal stability and sintering of BaTaO$_2$N

The thermal stability of BaTaO$_2$N powder in a helium atmosphere was

investigated at a heating rate of 20 °C/min. A slight initial weight loss due to the

desorption of adsorbed water and carbon dioxide was observed below 750 °C and a small

amount of nitrogen (0.88 wt%) was released, starting around 800 °C as confirmed by the

TG-MS results shown in **Fig. 3-1**. The above weight loss in wt% corresponds to 16 at%

of the theoretical nitrogen content of BaTaO$_2$N. Another, larger nitrogen release began

around 1150 °C as the sample began to decompose. A mixture of mainly Ta$_2$N (JCPDS

26-985) and β-Ba$_4$Ta$_2$O$_9$ (JCPDS 32-80) with an unknown impurity in a trace amount

were observed after the thermal analysis up to 1550 °C as in the XRD profiles of **Fig. 3-**

2. The decomposition at higher temperatures was strongly suppressed in a nitrogen

atmosphere and thermally robust nitrogen-deficient perovskite BaTaO$_2$N$_{0.85}$ still

remained as a main phase. These thermal behaviors are very similar, and the observed

temperature, especially that of the first nitrogen loss, was slightly lower than that of

57

SrTaO$_2$N (950 °C). [5] Additional TG measurement with a slow heating at 5 °C/min was conducted to determine more precise decomposition temperature of BaTaO$_2$N. The result shown in **Fig. 3-3** indicates that BaTaO$_2$N begins releasing its nitrogen at 920 °C. The lower thermal stability of BaTaO$_2$N may be related to the lower lattice enthalpy of the barium compounds than that of the strontium homologues. [8-10] The perovskite-type structure remained even after the first nitrogen loss and the cubic lattice parameter was a = 0.4107(3) nm, compared to 0.4112(2) nm before the nitrogen loss. Nitrogen was selected for the sintering atmosphere of the BaTaO$_2$N compacts because the decomposition of the perovskite-type structure is suppressed.

The green-compacts were sintered in a BN crucible using a BaTaO$_2$N powder bed. The sintering was performed at 1350 or 1400 °C for 1 – 8 h, similar to the conditions used in previous SrTaO$_2$N research [2,3], by changing the amount of BaCO$_3$ additive. All of the sintered bodies were black or brown in color. The crystalline phases observed on the ceramic surface were studied by XRD. A rock-salt type TaO impurity appeared with BaTaO$_2$N$_{0.85}$ perovskite in ceramics prepared without BaCO$_3$ additive, as shown in **Fig. 3-4(a)**. This impurity disappeared, and phase-pure BaTaO$_2$N$_{0.85}$ was obtained in ceramics sintered with 2.5 wt% of BaCO$_3$, as shown in **Fig. 3-4(b)**. Another impurity, Ba$_5$Ta$_4$O$_{15}$, appeared in ceramics sintered with 5 wt% of BaCO$_3$, as shown in **Fig. 3-4(c)**. Thus, the
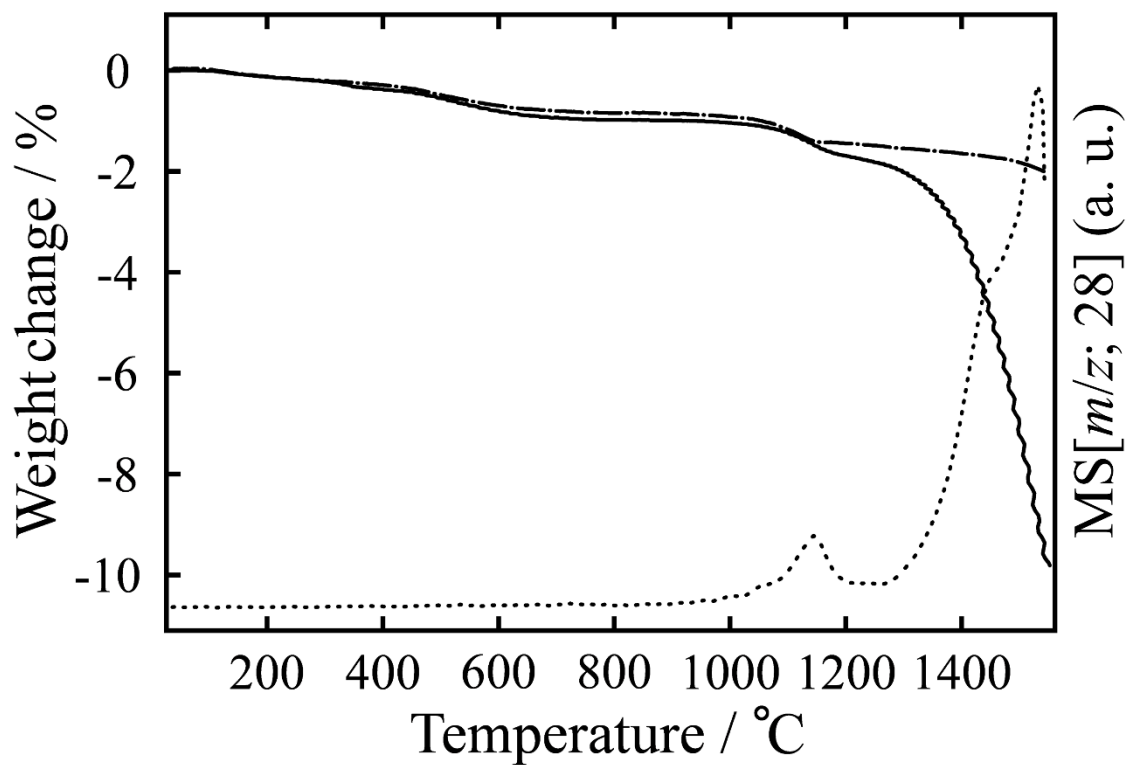
Fig. 3-1. Weight loss of BaTaO$_2$N oxynitride perovskite powder during heating in a helium (solid line) or nitrogen (dot-dashed line) atmosphere and nitrogen evolution detected in mass spectrometer (helium atmosphere, broken line). Heating rate in both atmospheres is 20 °C/min.
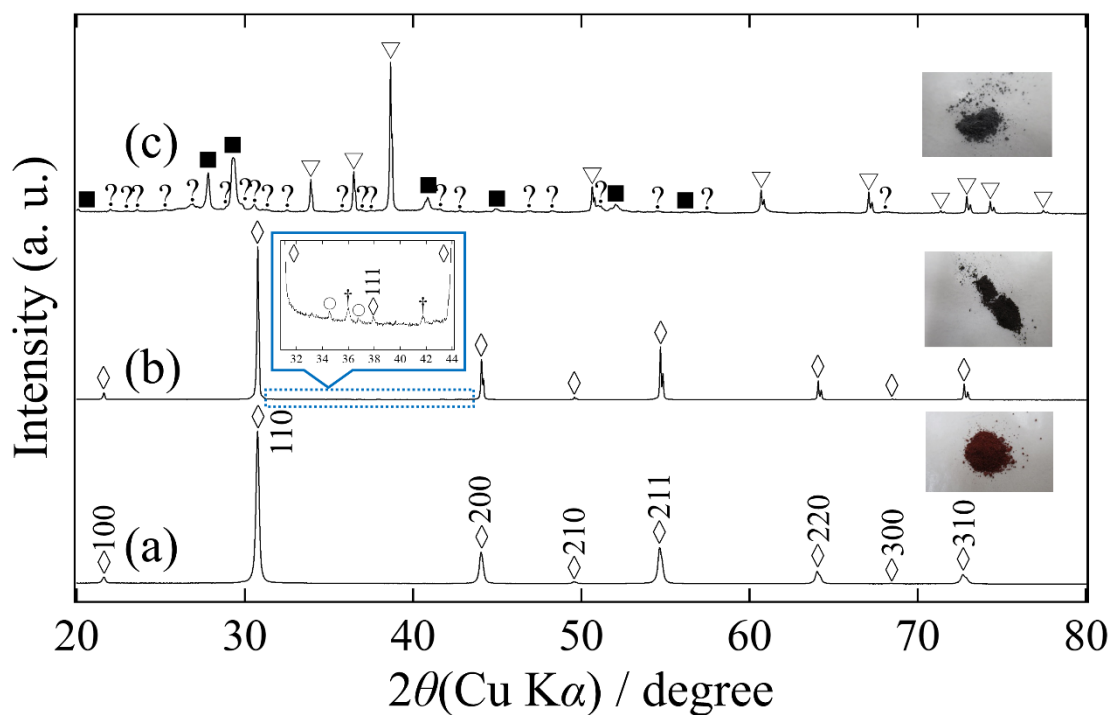
Fig. 3-2. Powder XRD profiles and photographs of **(a)** as-prepared BaTaO$_2$N, **(b** and **c)** samples after TG measurements up to 1550 °C under nitrogen and helium atmospheres, respectively. Diamonds, circles, daggers, squares, inverse triangles, and question marks indicate BaTaO$_2$N(ICSD 202763), θ-TaN(ICSD 76455), δ-TaN(ICSD 76456), β-Ba$_4$Ta$_2$O$_9$(JCPDS 32-80), Ta$_2$N(JCPDS 26-985), and unknown phases, respectively.
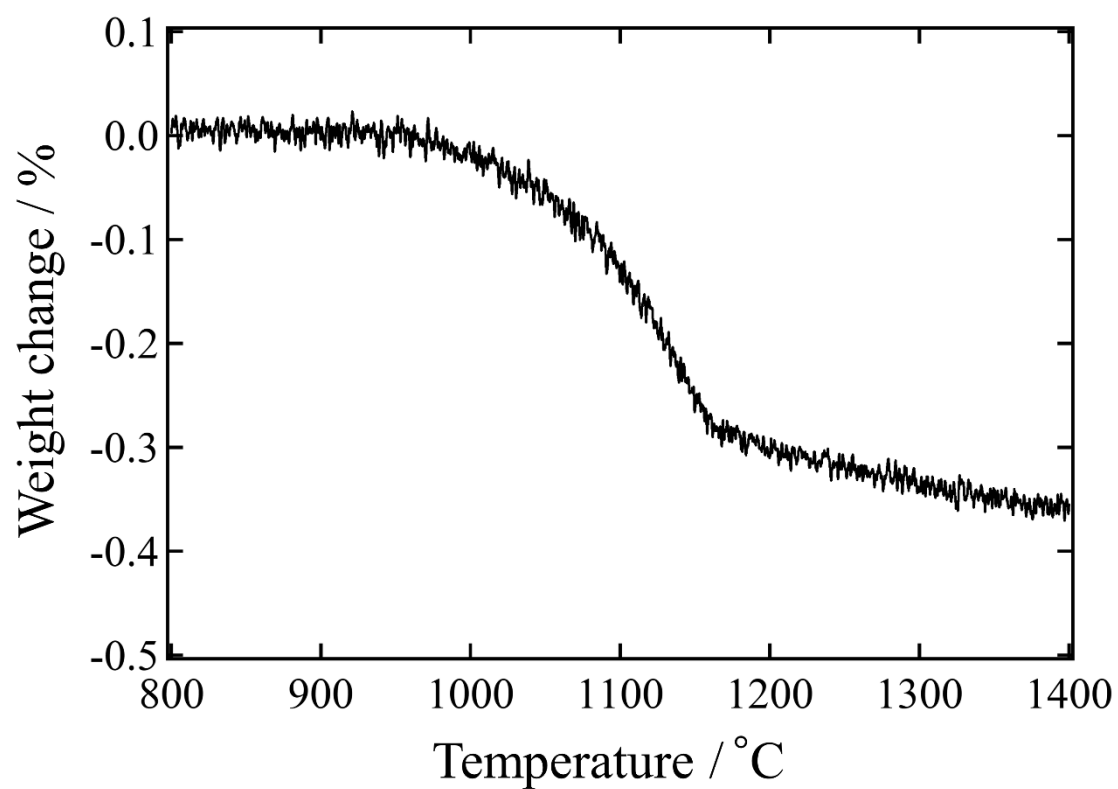
Fig. 3-3. TG curve of BaTaO$_2$N under flowing nitrogen at a heating rate of 5 °C/min.

2.5 wt% BaCO$_3$ additive enabled the production of phase-pure BaTaO$_2$N$_{0.85}$ ceramics

under the present sintering conditions. Further densification occurred with increases in

the sintering temperature and duration. The RD was only 59.4% after sintering at 1350

°C for 3 h, and reached 93% after 1400 °C for 6 h, as summarized in **Table 3-1**. A sintering

temperature of 1450 °C was necessary to obtain SrTaO$_2$N ceramics with RD > 90%. [2]

On the contrary BaTaO$_2$N can densify at lower temperatures than SrTaO$_2$N probably

because the diffusion of BaTaO$_2$N was assisted by its partial decomposition reaction that

begins slightly lower temperature than SrTaO$_2$N. [5]

SEM images of the fracture surfaces of each BaTaO$_2$N$_{0.85}$ ceramics are depicted

in **Fig. 3-5**. The grains were grown to several hundred nanometers in size, and some grain

necking was observed in ceramics sintered at 1350 °C for 3 h as shown in **Fig. 3-5(b)**.

The grains grew furtherly and the voids became smaller in ceramics sintered at a higher

temperature of 1400 °C for 3 h as depicted in **Fig. 3-5(c)**. These voids might have been

formed due to the partial release of nitrogen during sintering. On the other hand, they are

useful in post-annealing process under flowing ammonia to recover the partially lost

nitrogen. Voids shrank in size and the microstructure of the ceramics became denser by

the long duration at 1400 °C as in the images of **Fig. 3-5 (d – f)**.

The BaTaO$_2$N$_{0.85}$ ceramics sintered at 1400 °C for 3 h were post-annealed in

ammonia at 1000 – 1030 °C. The black as-sintered ceramics became red during the post-ammonolysis and the electrical conductivity decreased, changing from semiconductor to insulator in a manner similar to that of the annealing of $SrTaO_2N$ ceramics. [2-4] A trace amounts of $Ba_5Ta_4O_{15}$ impurity in the as-sintered $BaTaO_2N_{0.85}$ ceramics prepared with 2.5 wt% $BaCO_3$ at 1400°C for 3 h disappeared after post-ammonolysis, and the annealed product was phase-pure stoichiometric $BaTaO_2N$ according to XRD profiles of the ground sample as shown in **Fig. 3-6**. The cubic lattice parameter expanded slightly from $a =$ 0.4109(1) nm to $a = $ 0.4113(2) nm in the ceramics processed by post-annealing, probably because of the recovery in the nitrogen stoichiometry of the $BaTaO_2N$. The latter value is comparable to $a =$ 0.4112(1) nm observed in the as-prepared $BaTaO_2N$ powder and a reference value (0.41128 nm). [12]

The crystallinity was considerably improved by the sintering because of the much higher temperature of 1400 °C, compared to the preparation temperature of 930 °C. The nitrogen content slightly decreased by the sintering process but it was recovered in the post-ammonolysis, although the barium, tantalum, and oxygen contents almost unchanged by these processes as shown in **Table 3-2**.
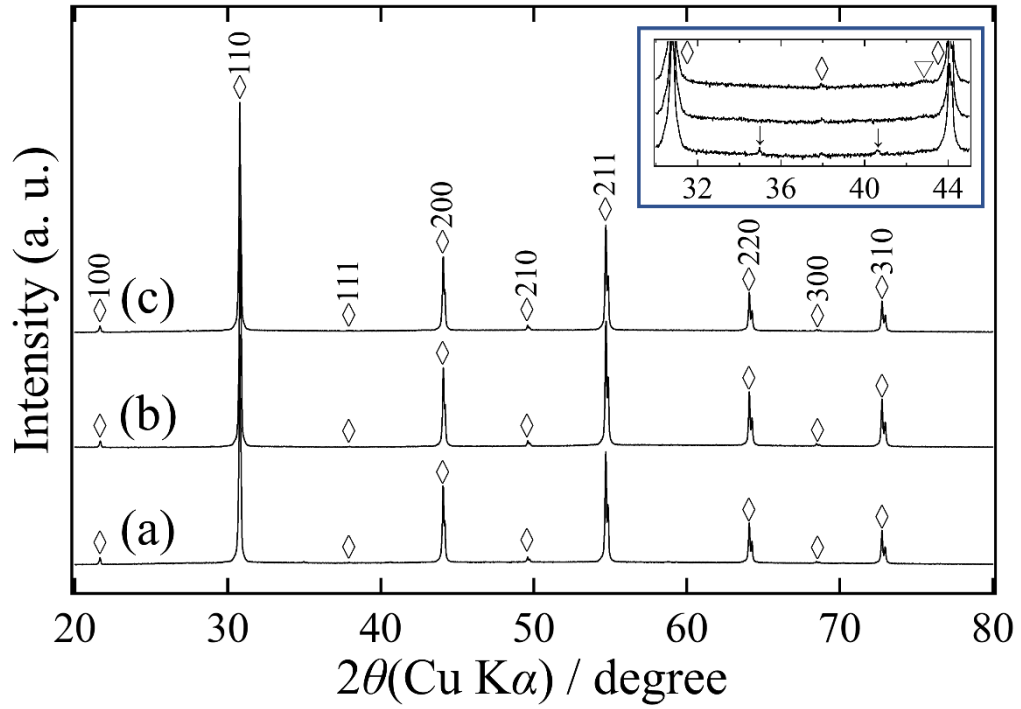
Fig. 3-4. X-ray diffraction patterns for the polished surface of BaTaO$_2$N ceramics sintered at 1400 °C for 6 h with **(a)** 0 wt%, **(b)** 2.5 wt%, and **(c)** 5.0 wt% of BaCO$_3$ additive. The inset is an expansion around the diffraction angle of 2θ = 30 – 45°. Diamonds, inverse triangles, and arrows represent diffractions for BaTaO$_2$N$_{0.85}$ (BaTaO$_2$N, ICSD 202763), Ba$_5$Ta$_4$O$_{15}$ (JCPDS 18-195), and TaO (ICSD 105549), respectively.
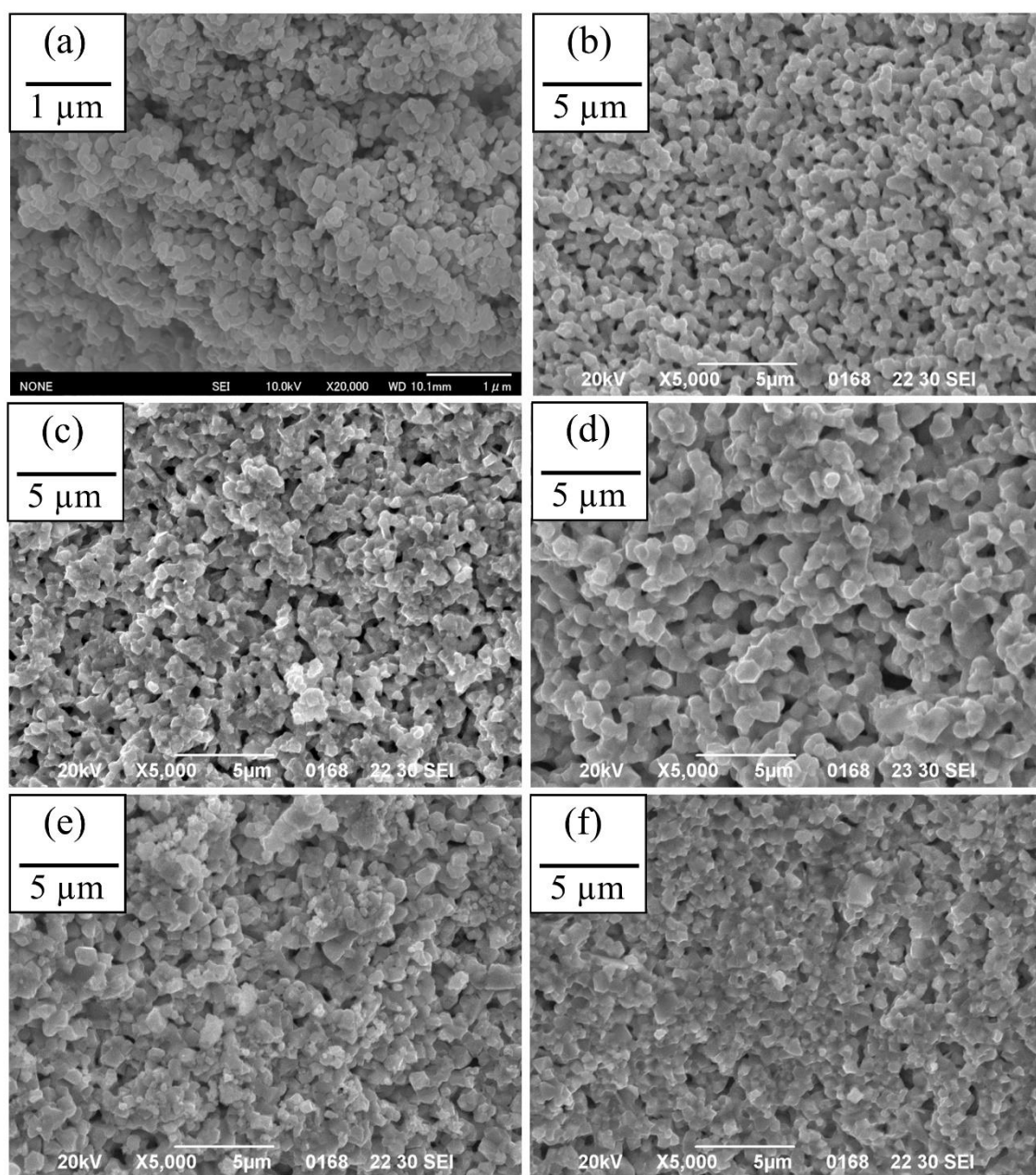
Fig 3-5. SEM micrographs of the fracture surfaces of **(a)** green-powder compact of BaTaO$_2$N and as-sintered BaTaO$_2$N$_{0.85}$ ceramics fabricated with 2.5 wt% of BaCO$_3$ sintered **(b)** at 1350 °C for 3 h and **(c)** – **(f)** at 1400 °C for 3, 4, 5, 6 h, respectively.

Table 3-1. Relative densities and crystalline phases of $BaTaO_2N$ ceramics.

Amount of BaCO$_3$ additive	Heating condition	Relative density (RD) / %		Crystalline phases	RD of SrTaO$_2$N$_{0.7}$ ceramics / % [2]
		as-sintered	Annealed		
5 wt%	1450 °C-4 h	86.8	-	BaTaO$_2$N$_{0.85}$	-
5 wt%	1450 °C-3 h	84.0	-	BaTaO$_2$N$_{0.85}$	-
2.5 wt%	1450 °C-3 h	88.7	-	BaTaO$_2$N$_{0.85}$/TaO	94.5
3 wt%	1400 °C-8 h	94.6	-	BaTaO$_2$N$_{0.85}$	-
2.5 wt%	1400 °C-8 h	90.0	-	BaTaO$_2$N$_{0.85}$/TaO	-
0 wt%	1400 °C-6 h	89.8	-	BaTaO$_2$N$_{0.85}$/TaO	-
5.0 wt%	1400 °C-6 h	92.0	-	BaTaO$_2$N$_{0.85}$/Ba$_5$Ta$_4$O$_{15}$	-
2.5 wt%	1400 °C-6 h	93.0	-	BaTaO$_2$N$_{0.85}$	84.0
2.5 wt%	1400 °C-5 h	87.6	-	BaTaO$_2$N$_{0.85}$	80.6
2.5 wt%	1400 °C-4 h	80.1	-	BaTaO$_2$N$_{0.85}$	-
2.5 wt%	1400 °C-3 h	74.6	73.0	BaTaO$_2$N$_{0.85}$/Ba$_5$Ta$_4$O$_{15}$	61.6
2.5 wt%	1400 °C-1 h	powder	-	BaTaO$_2$N$_{0.85}$/Ba$_5$Ta$_4$O$_{15}$	-
2.5 wt%	1350 °C-3 h	59.4	59.0	BaTaO$_2$N$_{0.85}$	59.5

The full recovery of the red color and chemical composition was difficult for the ceramics sintered for longer time in order to obtain higher RD values. The outer surface returned to red color and the interior remained black in ceramics with RD > 75%. Photographs of the fracture surfaces of the post-annealed $BaTaO_2N$ ceramics are depicted in **Fig. 3-7**. The residual black regions in a total sample volume increased with an increasing of RD. As for the dense ceramics with RD = 93.0%, the recovered outermost surface was observed as a layer in the cross-section image, the thickness of which was approximately 7 μm.

Dielectric properties of $BaTaO_2N$ ceramics

Electrical conductivity was estimated before and after post-annealing using Cole-Cole plots for $BaTaO_2N$ ceramics sintered at 1400 °C for 3 h. As-sintered $BaTaO_2N_{0.85}$ ceramics showed an arc of a semicircle in these plots, as depicted in **Fig. 3-8**. An electrical resistance of less than 1 MΩ cm was predicted by extrapolating the arc. The value is comparable to the one reported for $BaTaO_2N$ by Kim et al. [1] and slightly larger than those for $SrTaO_2N$ ceramics before annealing. [2,3] This extrapolation was impossible for post-annealed ceramics, suggesting insulating property. ε_r value was 620 at 10^2 Hz and decreased slightly to 320 at 10^8 Hz in post-annealed ceramics sintered at 1400 °C for 3 h with RD = 73.0%, as shown in **Fig. 3-9**. Lower ε_r values of 120 and 80
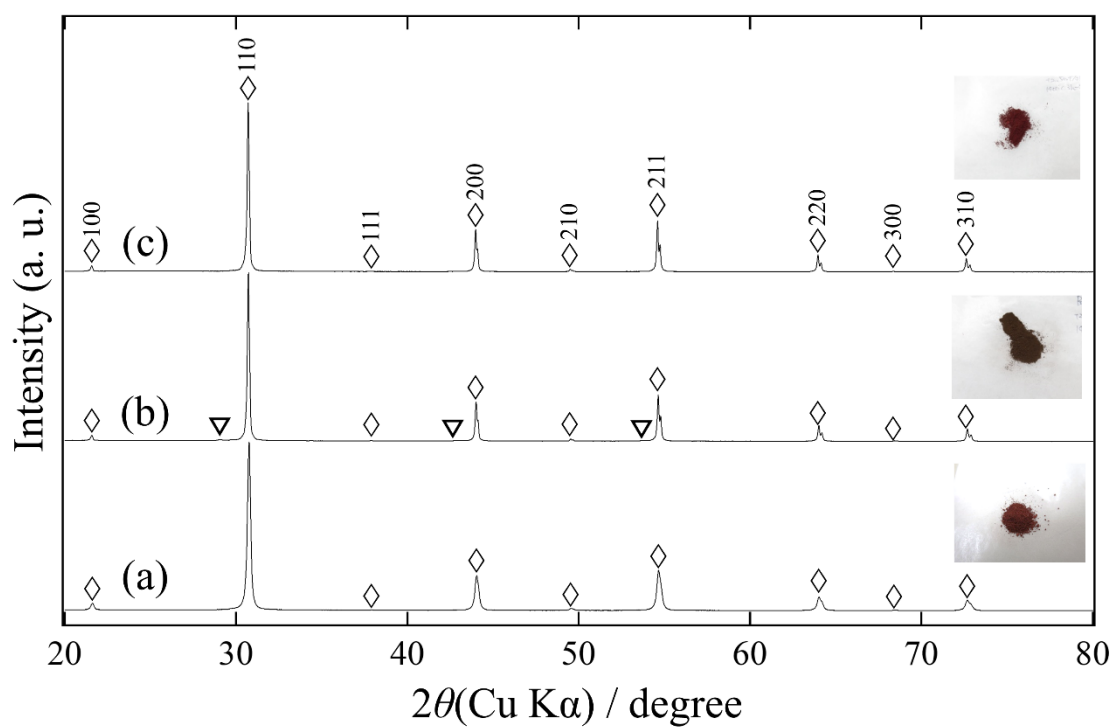
Fig. 3-6. Powder XRD profiles and photographs of **(a)** as-prepared $BaTaO_2N$, **(b)** ground as-sintered $BaTaO_2N_{0.85}$ ceramics fabricated at 1400 °C for 3 h with 2.5 wt% of $BaCO_3$, and **(c)** homogeneously post-annealed $BaTaO_2N$ ceramics. Diamonds and triangles indicate $BaTaO_2N$ (ICSD 202763) and $Ba_5Ta_4O_{15}$ (JCPDS 18-195), respectively.

Table 3-2. Elemental contents of BaTaO$_2$N samples at various processing steps. The ceramics were sintered with 2.5 wt% BaCO$_3$ at 1400 °C for 3 h.

	Ba / wt%	Ta / wt%	O / wt%	N / wt%
As-prepared powder	38.5(1)	50.0(2)	8.0(3)	3.5(1)
As-sintered ceramic	38.8(1)	49.2(2)	9.0(4)	3.0(1)
Post-annealed ceramic	38.5(1)	49.4(2)	8.8(3)	3.3(1)
Theoretical value	37.7	49.7	8.8	3.8

RD	Photograph	Color of interior
93.0%		Black
73.0%		Red
59.0%		Red

Fig. 3-7. Photographs of the fracture surfaces of the post-annealed $BaTaO_2N$ ceramics.

were obtained for the respective frequencies in post-annealed ceramics sintered at 1350 °C for 3 h with lower RD = 59.4%. These ceramics were well annealed and more homogeneous, even in their interiors, due to the high porosity. The dielectric loss was less than 0.4 for well-annealed ceramics sintered at 1400°C for 3 h with a relatively high RD = 73%. It is comparable to the reported value of less than 0.1 for $SrTaO_2N$. [2] ε_r values were 620 – 320 for $BaTaO_2N$ and 300 – 80 for $SrTaO_2N$ in the same frequency range. [2] Larger ε_r values were observed in the present $BaTaO_2N$ than in $SrTaO_2N$. Electronic contribution is suspected for the very large ε_r values of more than thousand in the preliminary experiments of $BaTaO_2N$ bulks. [1]

The temperature dependence of dielectric properties of post-annealed $BaTaO_2N$ ceramics sintered at 1400 °C for 3 h with RD = 73.0% was also investigated at temperatures up to 150 °C. The values did not change by the temperature very much, as shown in **Fig. 3-10**.

Piezoelectricity of BaTaO$_2$N ceramic specimen

Piezoresponse was studied on the $BaTaO_2N$ ceramic obtained by sintering at 1400 °C for 8 h and successive post-ammonolysis. XRD of the ceramic surface confirmed that the sintered body was phase-pure $BaTaO_2N$ belonging to the space group of $Pm\bar{3}m$ with $a = 0.4117(1)$ nm (see **Fig. 3-11**), which is comparable to the lattice parameter of

ICSD 202763 ($a = 0.41128$ nm). [12]

Only the surface was recovered to an original red color from black of the electrically conductive as-sintered dense ceramics during the post ammonolysis. Color was purple at rim of the thinner surface slice and dark purple in its thicker inside as shown in **Fig. 3-12**. Both topological and piezoresponse measurements were performed in two regions of a squared area of the thin specimen. Microstructure of the region **A** in **Fig. 3-12** was porous and low in density. There was no piezoresponse due to the porous nature of specimen. Microstructure was relatively dense in the region **B**, which was slightly interior of the slice, and piezoresponse slightly appeared as represented in **Fig. 3-13**. The area where did not show piezoresponse is porous probably due to the decomposition of a small amount of Ruddlesden-Popper type Ba_2TaO_3N impurity formed by the reaction of BaO and $BaTaO_2N$ during sintering. [11]

Some of the post-annealed ceramics had higher densities in its exterior sides along diameter than interiors just below its outermost surface as shown in **Fig. 3-14(a)**. Necking was more pronounced between grains in the former part to have much higher density and less porosity than the latter. STEM image showed that grains in size of less than 500 nm were closely packed each other in the former and there were many vacancies between the relatively grown grains in the latter as depicted in **Fig. 3-15**. No response
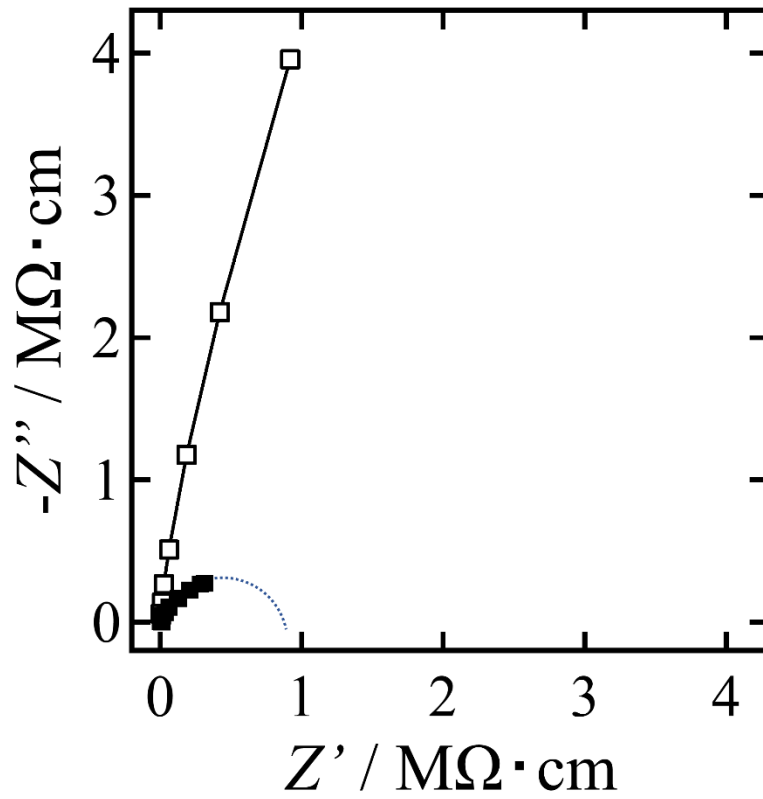
Fig. 3-8. Complex impedance spectra for post-annealed $BaTaO_2N$ ceramics sintered at 1400 °C for 3 h (open square) and just-sintered $BaTaO_2N_{0.85}$ ceramics (filled square). The measurements were conducted at a frequency range from 10^2 to 10^5 Hz at room temperature.
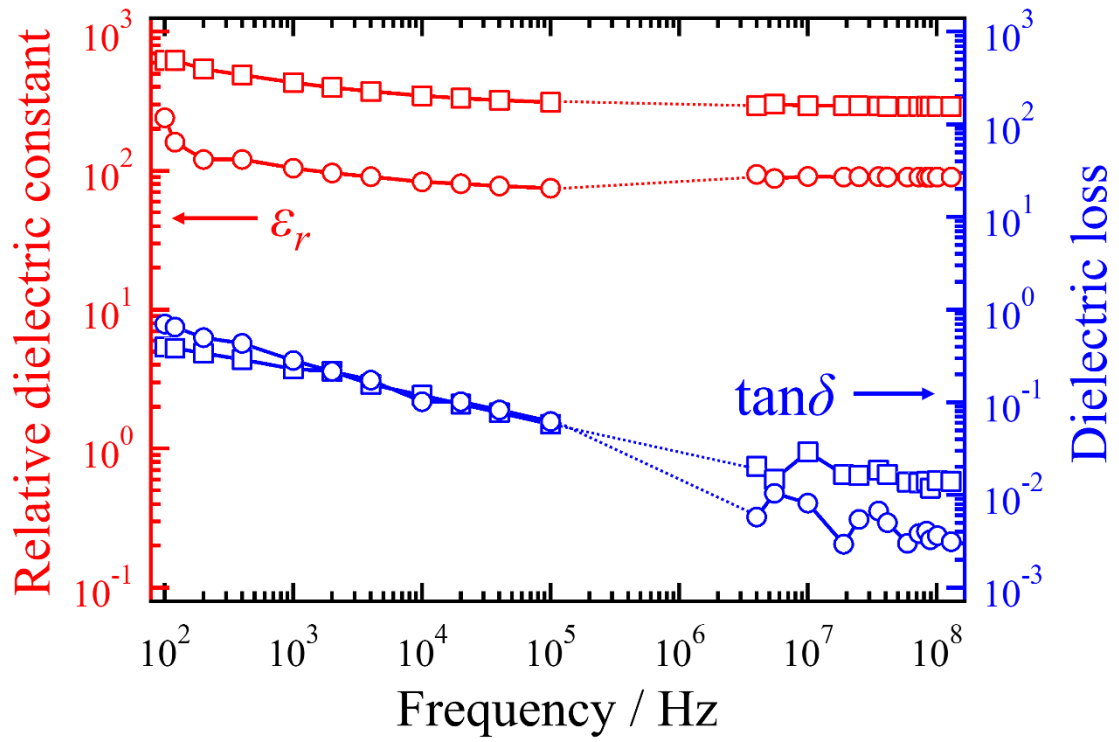
Fig. 3-9. Room temperature relative dielectric constants (red) and losses (blue) as functions of frequency for the post-annealed $BaTaO_2N$ ceramics sintered at 1400 °C for 3 h (open square). Open circles represent the values for post-annealed $BaTaO_2N$ ceramics sintered at 1350 °C for 3 h. The error bars are smaller than the symbols.
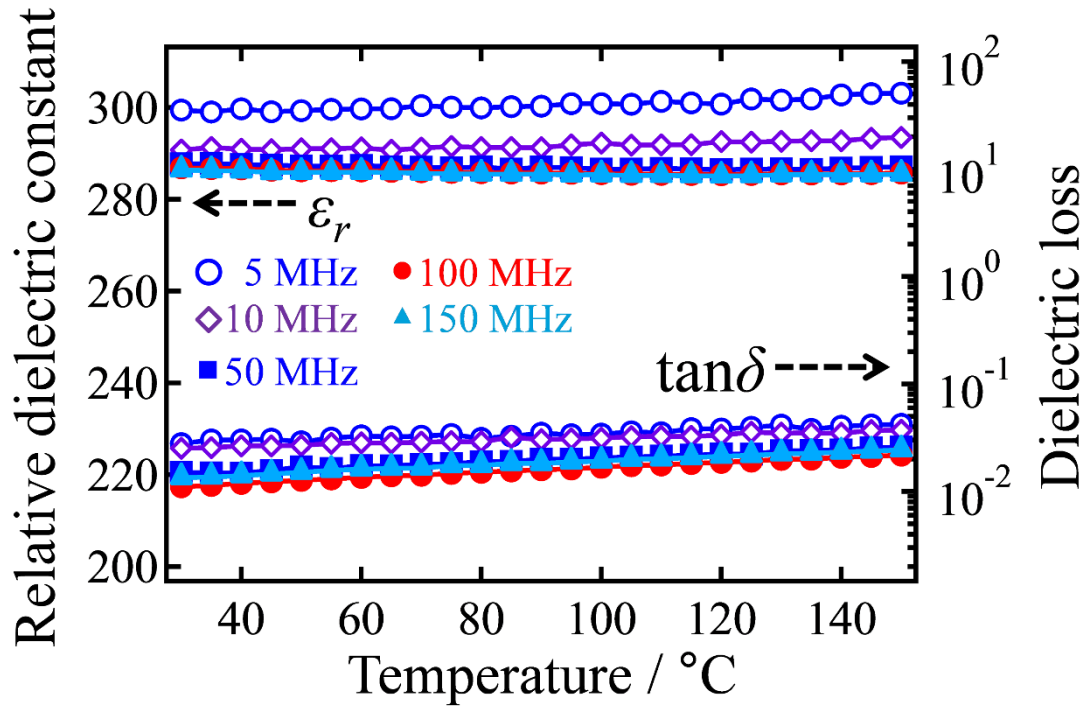
Fig. 3-10. Relative dielectric constant and loss values as functions of temperature for post-annealed BaTaO$_2$N ceramics sintered at 1400 °C for 3 h at various frequencies. The error bars are smaller than the symbols.
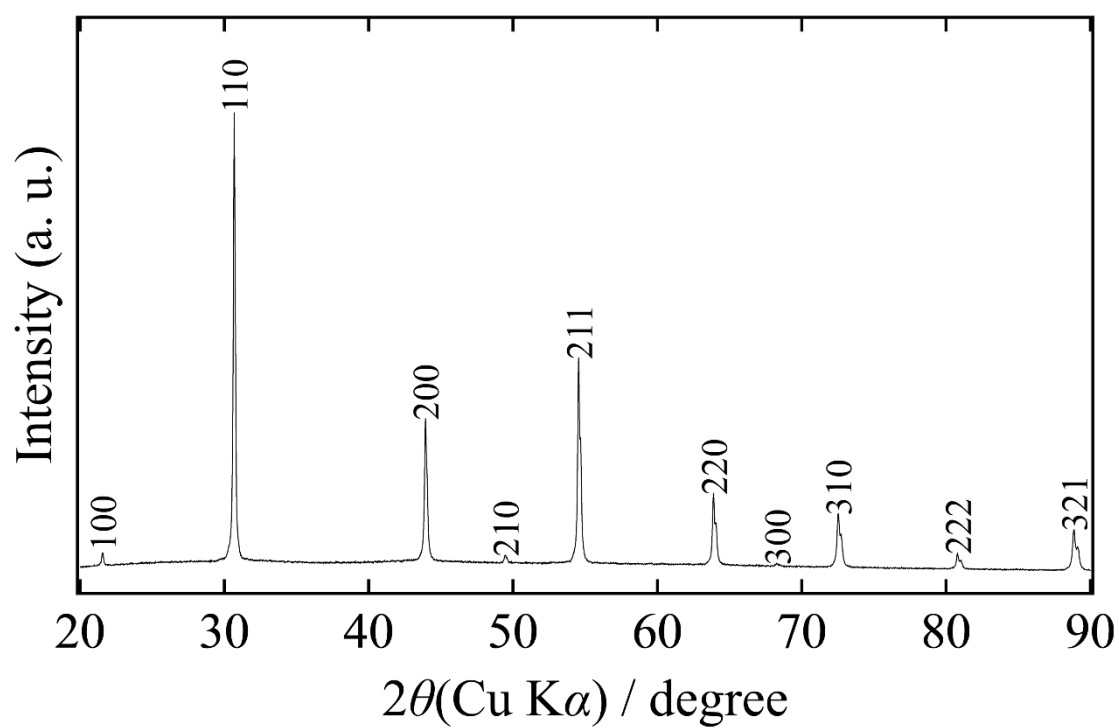
Fig. 3-11. XRD pattern of an annealed BaTaO$_2$N ceramic surface used for PFM measurements.
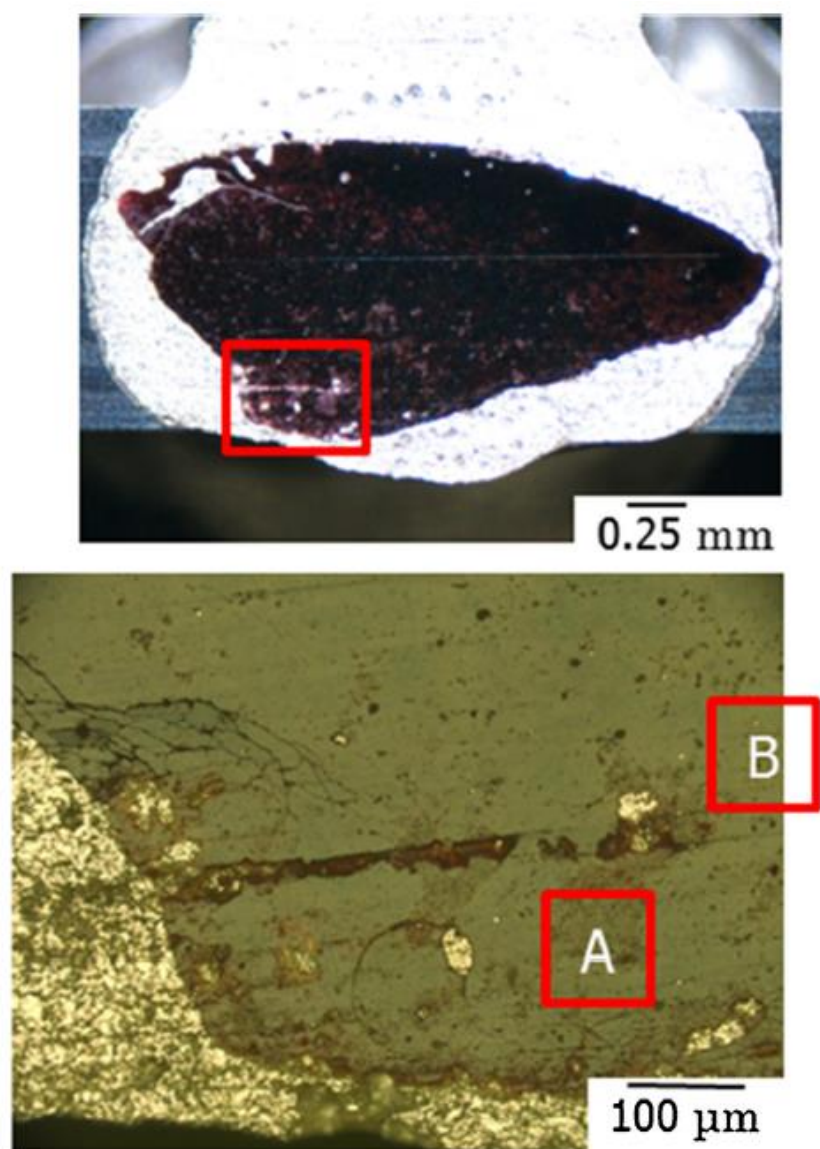
Fig. 3-12. Optical micrographs of a thin surface slice of an annealed $BaTaO_2N$ ceramics. PFM specimens **A** and **B** were prepared from the area indicated by the red square in the upper image.
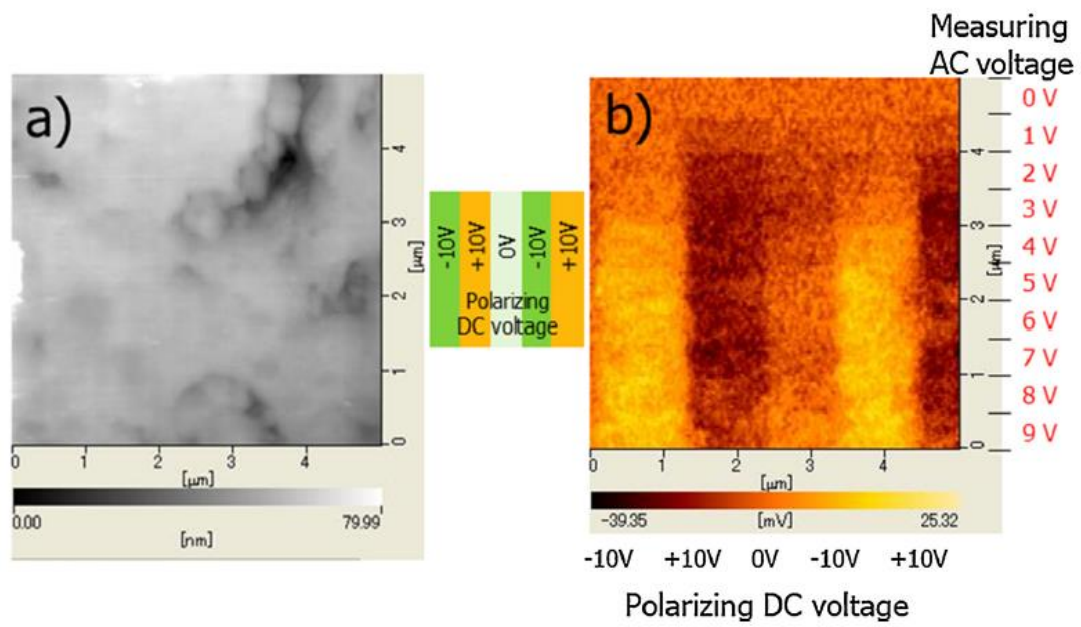
Fig. 3-13. Topographic **(a)** and PFM **(b)** images of region **B** in **Fig. 3-12**. DC biases of ±10 V were applied alternately in a vertical stripe pattern in the center.
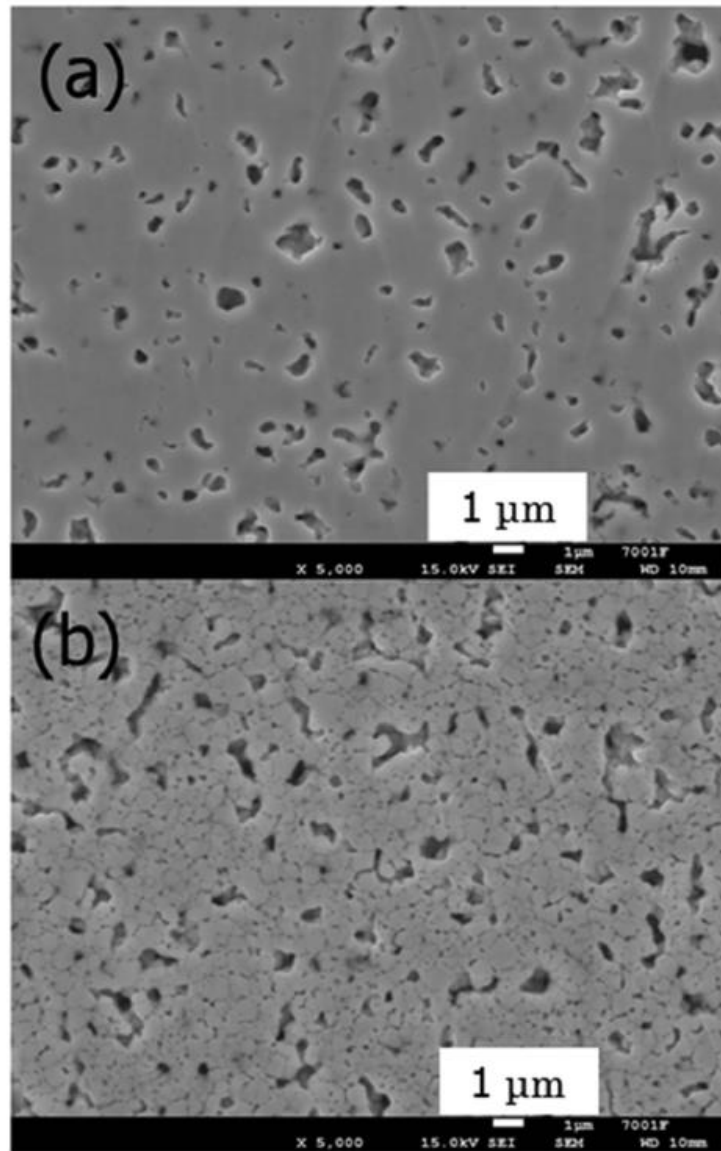
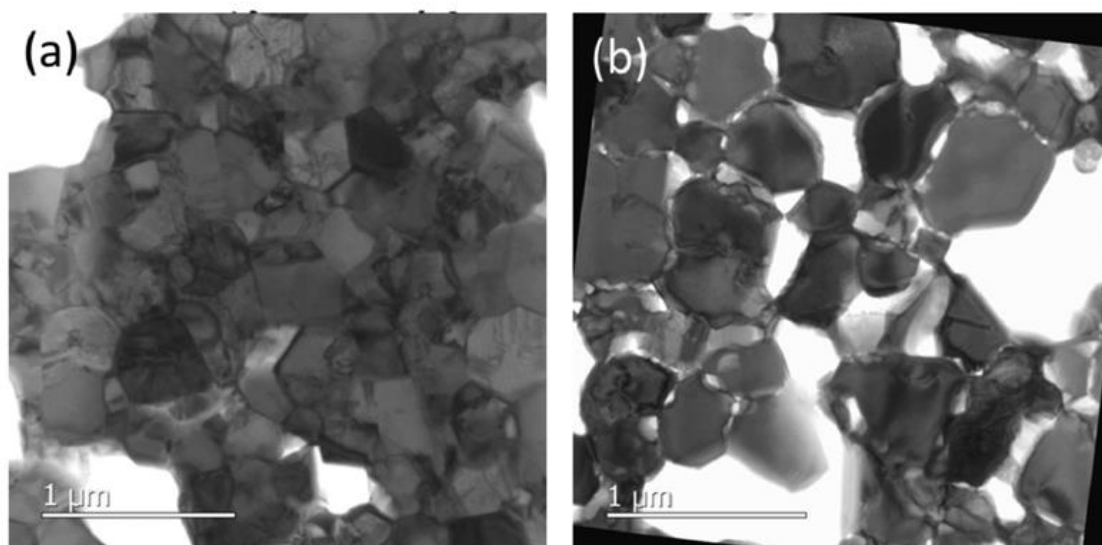**Fig. 3-14.** SEM micrographs on **(a)** the perimeter and **(b)** central area of the annealed BaTaO$_2$N ceramics.

Fig. 3-15. STEM images on **(a)** the perimeter and **(b)** central area of the annealed BaTaO$_2$N ceramics.

was observed on a specimen from the latter part in PFM measurement. A specimen from the dense part clearly showed polarized patterns in an applied bias voltage between -10 V and +10 V as represented in **Fig. 3-16**. The piezoresponse was most clear at the voltage between ±4 V and 7 V, and it was continuously observed even at ±9 V. It had been reported that the response was most clear in the lower voltages of ±3 – 4 V and became less clear at ±8 V on $SrTaO_2N$ ceramics. [4] The clear response was observed at higher voltage in $BaTaO_2N$ than in $SrTaO_2N$. The present response observed at an applied voltage of ±6 V gradually disappeared with time similarly to the case of $SrTaO_2N$. The response amplitude in 15 min decreased to almost a half in 150 min as shown in **Fig. 3-17**. This may be because the polarization is not saturated at the poling voltage of ±10 V.

The piezoresponse contrast was strongest at voltages between ±4 and 7 V and continued to be observed even at ±9 V. This behavior was quantified by plotting the contrast against the measuring voltage (see **Fig. 3-18**). The contrast was defined as the difference between the average responses in the positively and negatively poled regions. It increased up to a measuring voltage of ±7 V and then decreased slightly, owing to the elapsed measuring time. Similar PFM measurements could not be made while decreasing the measuring voltage, presumably because current leakage occurred, similarly to the case for $SrTaO_2N$. [4] There was no apparent change in the topographic images taken
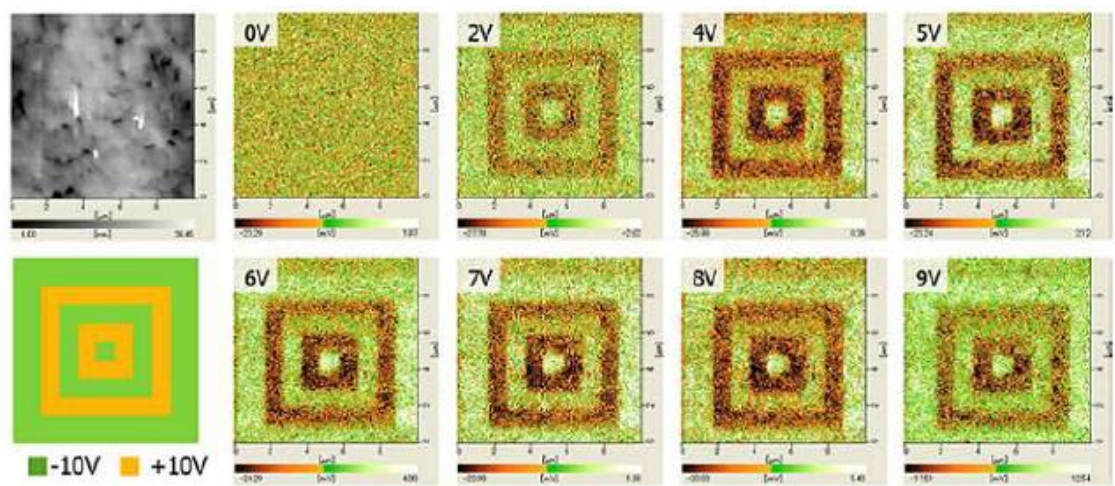
Fig. 3-16. AFM topograph (upper left) and PFM images taken at various voltages. These were polarized by applying DC biases of ±10 V according to the pattern shown in the lower leftmost image.
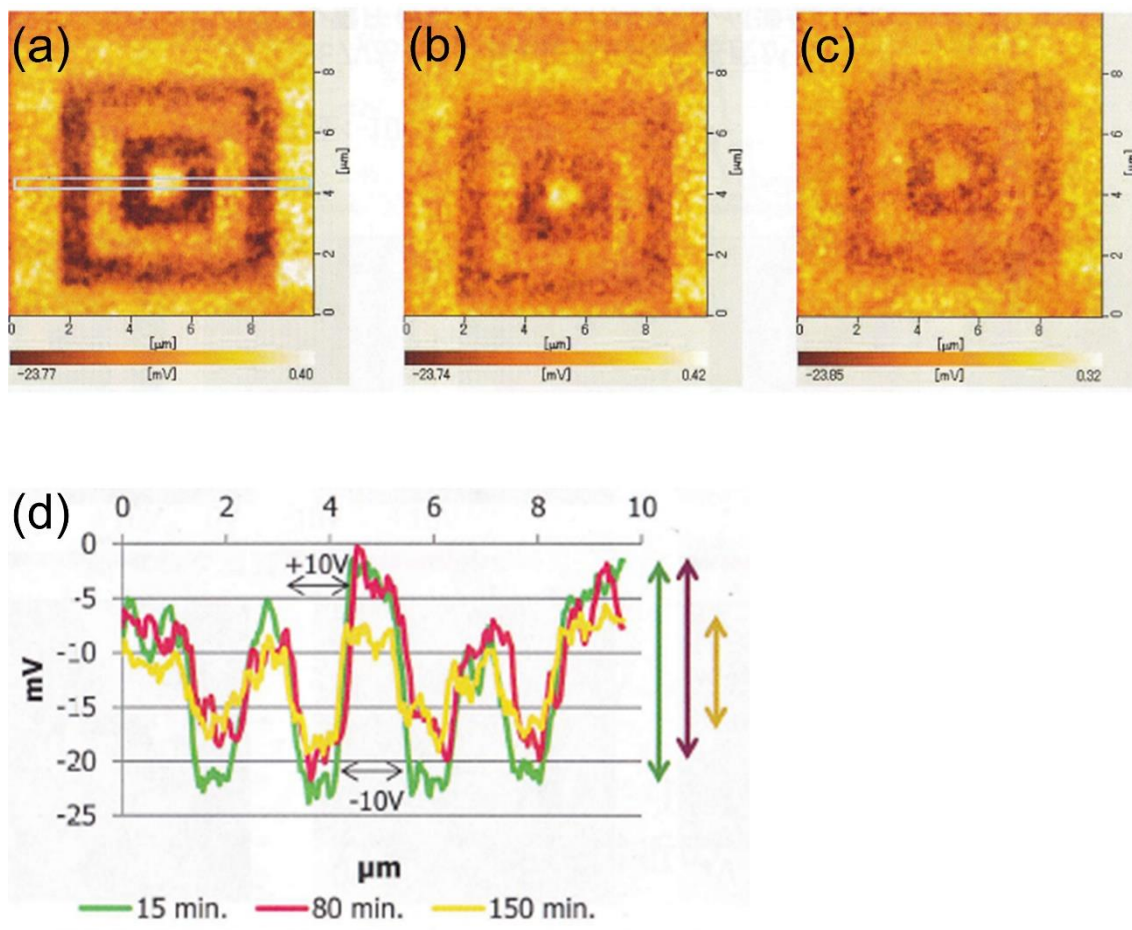
Fig. 3-17. AFM images scanned **(a)** 15, **(b)** 80, and **(c)** 150 min after initial polarization. **(d)** is the AFM signals taken at the area indicated with gray square in **(a)**.
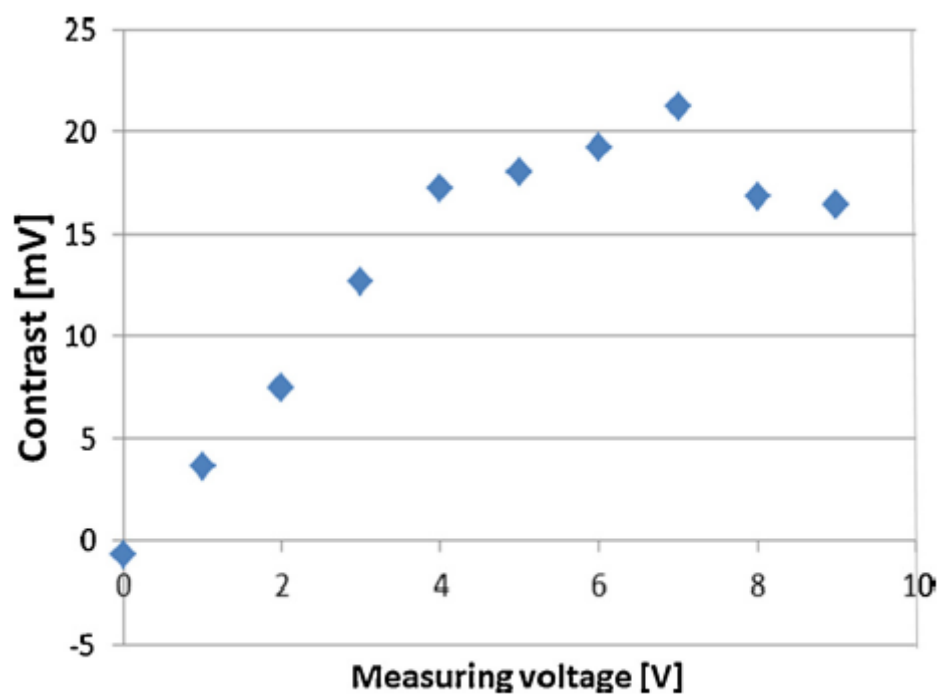
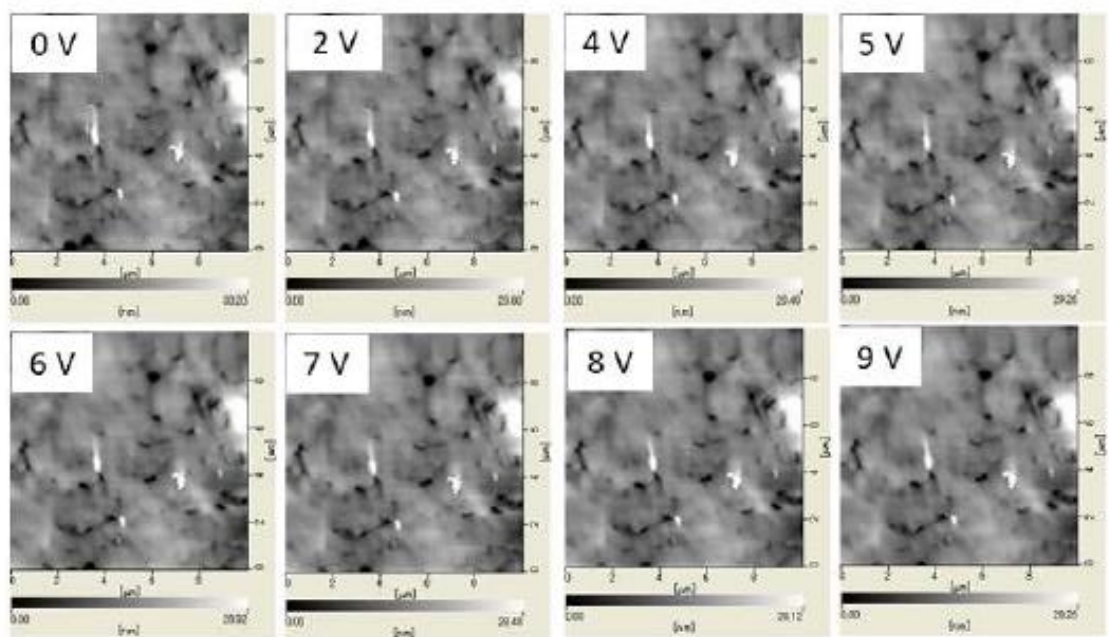**Fig. 3-18.** Quantified PFM contrast against measuring voltage.

Fig. 3-19. Topographic images taken at increasing measuring voltages during PFM.

during PFM measurements (see **Fig. 3-19**). The abovementioned decrease in contrast is not due to wear of the conductive coating on the tip. It has previously been reported that the PFM contrast for $SrTaO_2N$ was strongest at $\pm 3 - 4$ V, weakening at ± 8 V. [4] At higher voltages (± 7 V), a clearer contrast was observed on $BaTaO_2N$ compared to $SrTaO_2N$, possible suggesting a higher coercivity.

Current leakage occurred at ± 1 V in its *P-E* measurement using Pt-deposited electrode in size of $15 \times 15 \times 0.6$ μm^3 probably because of its slightly conductive nature even after post-ammonolysis. $BaTaO_2N$ ceramics or crystals with higher electrical insulation are desired for further investigation on their ferroelectric properties enabling to apply higher electrical voltages for polarization saturation.

3-4. Conclusion

Thermal decomposition behavior of $BaTaO_2N$ powder synthesized by ammonolysis of the $BaCO_3$ and Ta_2O_5 mixture was similar to $SrTaO_2N$ and it was sintered above 1350 °C. Both of the addition of $BaCO_3$ and post-ammonolysis were necessary to obtain phase-pure $BaTaO_2N$ ceramics by compensating for the partial loss of barium and nitrogen during sintering. Stoichiometric $BaTaO_2N$ ceramics with RD = 73.0% had relative dielectric constants of 620 at 10^2 Hz and 320 at 10^8 Hz, slightly higher than the

values reported for $SrTaO_2N$. These values were relatively unaffected in the applied frequency and temperature, up to 150 °C. The dielectric loss was less than 0.1 at higher frequency range than 10 kHz and it was nearly independent of frequency and temperature.

Clear piezoresponse was observed at the applied voltage between ±4 – 7 V on the surface slice of dense $BaTaO_2N$ ceramics with RD > 90%, which is consistent with the results of SHG and structural reinvestigations mentioned in the last chapter. Piezoresponse was slightly present on another thin slice prepared from inside of the electrically conductive ceramics. This poor electrical insulation disturbed the elucidation of ferroelectricity. Its outermost surface did not show any piezoresponse because high porosity was easily induced due to the more hygroscopic nature of $BaTaO_2N$ than $SrTaO_2N$. Further target is the fabrication of stoichiometric and dense oxynitride perovskite ceramics or, more desirably, grain boundary-free single crystals to make it possible to investigate their intrinsic electrical properties by enabling to apply higher electrical voltage to the samples.

Chapter 3 References

[1] Y. -I. Kim, P. M. Woodward, K. Z. Baba-Kishi, C. W. Tai, "Characterization of the Structural, Optical, and Dielectric Properties of Oxynitride Perovskites AMO_2N (A = Ba, Sr, Ca; M = Ta, Nb)", *Chem. Mater.*, 2004, 16, 1267–1276.
[2] S. -K. Sun, Y. -R. Zhang, Y. Masubuchi, T. Motohashi, S. Kikkawa, "Additive

sintering, postannealing, and dielectric properties of SrTaO$_2$N", *J. Am. Ceram. Soc.* , 2014, 97, 1023–1027.

[3] Y. -R. Zhang, T. Motohashi, Y. Masubuchi, S. Kikkawa, "Sintering and Dielectric Properties of Perovskite SrTaO$_2$N Ceramics", *J. Eur. Ceram. Soc.*, 2012, 32, 1269–1274.

[4] S. Kikkawa, S. -K. Sun, Y. Masubuchi, Y. Nagamine, T. Shibahara, "Ferroelectric response induced by *cis*-type anion ordering in SrTaO$_2$N oxynitride perovskite", *Chem. Mater.*, 2016, 28, 1312–1317.

[5] D. Chen, D. Habu, Y. Masusbuchi, S. Torii, T. Kamiyama, S. Kikkawa, "Partial nitrogen loss in SrTaO$_2$N and LaTiO$_2$N oxynitride perovskites", *Solid State Sci.*, 2016, 54, 2–6.

[6] S. V. Kalinin, D. A. Bonnell, "Imaging mechanism of piezoresponse force microscopy of ferroelectric surface", *Phys. Rev. B*, 2002, 65, 125408/1–11.

[7] D. A. Bonnell, S. V. Kalinin, A. L. Kholkin, A. Gruverman, "Piezoresponse Force Microscopy: A Window into Electromechanical Behavior at the Nanoscale", *MRS Bulletin*, 2009, 34, 648–657.

[8] Fig. EC-131, ACerS-NIST Phase Equilibria Diagrams. Originally from W. Wong-Ng, R. S. Roth, B. H. Toby, J. Y. Chan, J. Dillingham, T. A. Canderah, National Institute of Standards and Technology, Gaitherburg, Maryland; Private comm. (2002).

[9] Fig. 92-002, ibid. Originally from L. M. Kovba, L. N. Lykova, M. V. Paromova, L. M. Lopato, A. V. Shevchenko, Zh. Neorg. Khim., 1977, 22, 2845–2847.

[10] "*Shriver & Atkins Inorganic Chemistry*", P. Atkins, T. Overton, J. Rourke, M. Weller, F. Armstrong (Eds.), Oxford University Press, United Kingdom (2005).

[11] S. J. Clarke, K. A. Hardstone, C. W. Michie, M. J. Rosseinski, "High-temperature synthesis and structures of perovskite and n=1 Ruddlesden-Popper tantalum oxynitrides", *Chem. Mater.*, 2002, 14, 2664–2669.

[12] F. Pors, R. Marchand, Y. Laurent, "Structural study of BaTaO$_2$N and BaNbO$_2$N oxynitrided perovskites", *Mat. Res. Bull.*, 1988, 23, 1447–1450.

Chapter 4

Melting Behavior of Alkaline-Earth Metal Carbodiimides for the Preparation of $Sr_{1-x}Ba_xTaO_2N$ ($x = 0.04 - 0.23$) Microcrystals

4-1. Introduction

In the last chapter, thermal stability, sinterability, and dielectricity of $BaTaO_2N$ were studied. It partially releases its nitrogen during high temperature sintering to become electrically conductive. Post-ammonolysis is required to recover their stoichiometric compositions. Large relative dielectric constants $\varepsilon_r = 290 - 620$ and piezoresponse were observed for the annealed ceramics, but a serious current leakage made it impossible to apply high electrical voltage to elucidate the emergence of ferroelectricity. Fabrication of oxynitride ceramics and crystals avoiding their thermal decomposition is necessary to obtain highly-insulating samples. $SrTaO_2N$ and $BaTaO_2N$ begin releasing a part of their nitrogen at 950 and 920 °C, respectively. [1] This nitrogen release from $SrTaO_2N$ could not be suppressed during the sintering even under 190 MPa nitrogen. [2] The purpose of the present chapter is sintering or crystal growth of oxynitride materials at the temperatures below their nitrogen releasing. Liquid phase sintering and flux growth are very sensible strategies to solve this problem and fluxes with melting points lower than the nitrogen releasing points of oxynitride perovskites are desirable.

Fluxes have been employed to grow various oxide crystals. For example, single

crystals of $BaTiO_3$, $BaTa_2O_6$, $BaFe_{12}O_{19}$, $Sr_2Ta_2O_7$, and $SrTiO_3$ were grown with fluxes

mainly containing B_2O_3, PbO, Na_2O, $SrCl_2$, and KF, respectively. [3-7] In this process,

the material of interest is partially soluble to the flux and the molten flux contains one of

the constituents of the crystals and needs to be entirely removed from the product.

There have been only several reports regarding the flux growth of oxynitride

crystals. As for oxynitride perovskites, $BaTaO_2N$ and $LaTiO_2N$ submicron crystals were

synthesized using KCl and K_2MoO_4 as the fluxes and cubic microcrystals reflecting the

euhedral form of the perovskite-type structure were obtained. [11,12] It should be noted

that residual potassium was detected in the product even after the removal of flux by

evaporation. Ammonothermal method was employed to grow micron-sized oxynitride

perovskite crystallites such as ABO_2N (A = Sr, Ba, B = Nb, Ta) [13], LnTaON$_2$ (Ln = La,

Ce, Pr, Nd, Sm, Gd) [14], and $LaNbON_2$ [15]. However, there is no reports on the

electrical properties of such crystals. Moreover, some contamination of the mineralizer

like NaN_3 and NaOH is concerned. In other cases, many researches on the preparations

of nitride crystals and oxynitride powders have been conducted in the groups of DiSalvo

and Jansen by using Na metal and sodium azide (NaN_3). [8-10] 100 μm-sized single

crystals of Ba_3ZnN_2O, Ba_4GaN_3O, and Sr_4GaN_3O have been grown by the reactions of a

Na flux with several metals and oxides at 750 °C in a nitrogen atmosphere. [16-18] Most

of sodium evaporated during the synthetic processes and the residual sodium was completely removed by washing the product with liquid ammonia to obtain pure oxynitride single crystals. [16] Fluxes with rich nitrogen contents are beneficial to obtain single crystals of nitrides and oxynitrides.

The author focused on metal carbodiimides as the candidates of the flux for the crystal growth and sintering of oxynitride perovskites. Metal carbodiimides are composed of metal cations and symmetric $[N=C=N]^{2-}$ anionic units, which is distinguished from asymmetric cyanamide anions $[N–C\equiv N]^{2-}$. Solid-state research on metal carbodiimides and cyanamides has a long history, and a large number of syntheses have been reported up to the present day, including alkaline metals (Li, Na, K, Cs) [19-22], alkaline-earth metals (Ca, Sr, Ba) [23,24], typical main-group elements (Mg, Si, Tl, Pb) [23,25-27], transition metals (Cr, Mn, Fe, Co, Ni, Cu, Zn, Y, Ag, Cd) [26,28-34], and also rare earth metals (Pr, Nd, Sm, Eu, Gd, Tb, Dy, Ho, Er, Tm, Yb). [33,35] In recent years, ternary metal carbodiimides such as $SrZn(CN_2)_2$ and $LiM(CN_2)_2$ (M = Al, In, Yb) were also synthesized. [36,37] Most of them, especially thermally unstable metal carbodiimide compounds, have been effectively synthesized by the metathesis reactions between metal halides and carbodiimides. [28,29,31-33,35,37] Ammonolysis reaction was also applied on metal carbonates. [38-40] This route can be applied in the cases the starting materials

of alkaline-earth metal carbonates are stable up to the nitridation temperature by ammonia (c.a. 500 °C).

Alkaline-earth metal carbodiimides $CaCN_2$, $SrCN_2$, and $BaCN_2$ have been investigated on their crystal structures. [23,24,40,41] The alkaline-earth metal cations are coordinated by several nitrogen atoms in their carbodiimide anion units. $SrCN_2$ has two polymorphs as shown in **Fig. 4-1**. β-type low temperature rhombohedral phase of $SrCN_2$, which is isomorphic to $CaCN_2$ [24,41], transforms to α-type high temperature orthorhombic phase [41] at approximately 630 °C according to *in-situ* XRD study conducted in argon atmosphere. However, thermal behavior of $SrCN_2$ above 800 °C has not been reported yet. Rhombohedral $BaCN_2$ (*r*-$BaCN_2$, **Fig. 4-2(a)**) was synthesized by the reaction of barium nitride with melamine at 740 °C. [23] Tetragonal $BaCN_2$ polymorph (*t*-$BaCN_2$, **Fig. 4-2(b)**) was recently obtained by the ammonolysis of $BaCO_3$ at 900 °C and its crystal structure and optical properties were studied. [40] Each Ba^{2+} ion in *r*-$BaCN_2$ is coordinated by six nitrogen atoms forming significantly distorted BaN_6 octahedra. [23] For *t*-$BaCN_2$, the coordination number of Ba^{2+} is eight, resulting in a symmetric BaN_8 square-antiprism. [40]
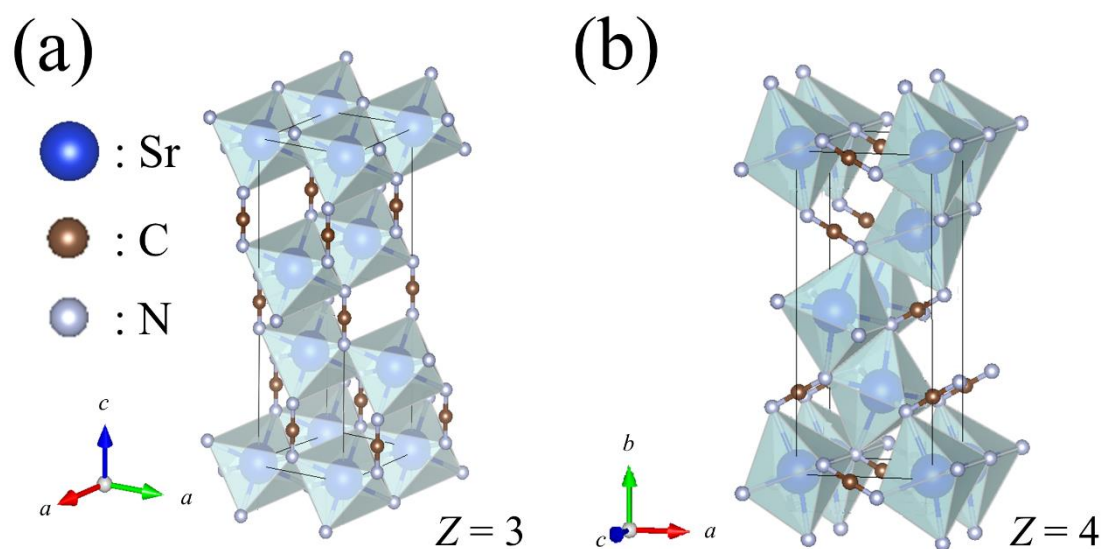
Fig. 4-1. Crystal structures of **(a)** β- and **(b)** α-SrCN$_2$. [41] The structure models were drawn with a crystallographic imaging software VESTA. [42]
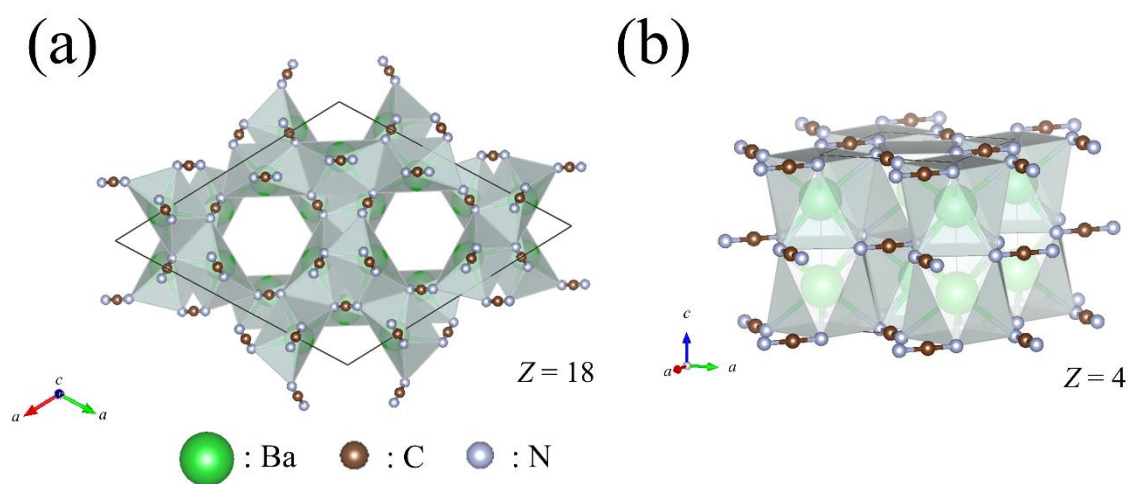

Fig. 4-2. Crystal structures of **(a)** r- and **(b)** t-BaCN$_2$. [23,40] The structure models were drawn with a crystallographic imaging software VESTA. [42]

Interestingly enough, the thermodynamical stability of the $BaCN_2$ polymorphs has not been investigated. This is not surprising since precise thermogravimetry on the metal carbodiimides is not so easy because they thermally decompose around their melting points. Also, their high reactivity against oxygen and humidity also makes any such measurement quite difficult. On the other side, density functional theory (DFT) calculations are useful to get a first clue as regards the thermal properties of unstable and reactive materials. [41]

In this chapter, thermochemical studies were performed experimentally and then total-energy was calculated on a series of alkaline-earth metal carbodiimides. Their melting behaviors were discussed in relation to their thermal decomposition around their melting points. The stabilities of r- and t-$BaCN_2$ were also compared based on their theoretical Gibbs free energies as derived from the quasi-harmonic phonon simulations. Furthermore, $SrTaO_2N$ was heated with various quantities of molten $BaCN_2$ at approximately 900 °C, which is about 50 °C below the nitrogen release temperature of $SrTaO_2N$. [1] After cooling, the dielectric properties, crystalline phases, chemical compositions, and microstructure of the resulting solids were investigated.

4-2. Experimental

Syntheses and thermal studies of metal carbodiimides

$CaCN_2$, α-$SrCN_2$, and t-$BaCN_2$ powders were synthesized by ammonolysis of their respective carbonates. [38-40] In each case, more than 100 mg of the carbonate powder (99.9%, FUJIFILM Wako Pure Chemical) was heated on an alumina boat under a flowing ammonia (50 mL/min) in an alumina tube furnace at about 600 °C for $CaCN_2$ and 900 °C for both of α-$SrCN_2$ and t-$BaCN_2$ with a duration of 10 h. Chemical compositions of the ammonolysis products α-$SrCN_2$ and t-$BaCN_2$ were confirmed with inductively coupled plasma atomic emission spectroscopy (ICP-AES, ICPE9000, Shimadzu) for metal element contents in combination with combustion CHN analysis (MICROCORDER JM10, J-Science Lab.) for carbon and nitrogen contents. Chemical formulas for the metal carbodiimides were determined as $SrC_{1.01}N_{2.02}$ and $BaC_{0.99}N_{1.99}$, respectively. The obtained white $CaCN_2$ powder contained 18 wt% of CaO as a secondary phase as shown in the XRD profile **Fig. 4-10(a)** discussed in the latter part of this chapter. The amount of $CaCN_2$ and CaO were estimated using Rietveld calculation. [43] Preparation of phase-pure $CaCN_2$ was challenging because both of the ammonolysis reaction and decarboxylation of $CaCO_3$ on an alumina ceramics start at similar temperature range (approximately 550 °C and 610 °C [44]). Nitridation of $CaCO_3$ at only

95

550 °C did not proceed very much and not realistic heating time will be necessary to increase phase purity of $CaCN_2$ in the products. Crystalline phases of powder products were identified using X-ray diffraction (XRD, Ultima IV, Rigaku) with Cu Kα radiation over the 2θ range of 10 to 90° with a step size of 0.02° and a scanning rate of 10°/min.

Thermal behaviors were investigated on more than 10 mg of the samples of the metal carbodiimides using thermogravimetry in combination with differential thermal analysis (TG-DTA, STA 2500, Netzsch). The sample chamber was evacuated to about 3 Pa prior to the measurement, after which nitrogen gas (> 99.999%, Airwater Inc.) was introduced. The temperature was raised at a rate of 10 °C/min to 1000 or 1100 °C under a 200 mL/min of nitrogen flow. To reduce background noise, the DTA analysis for t-$BaCN_2$ was conducted with a hand-made alumel-chromel thermocouple (Nilaco) under a flowing nitrogen, using α-Al_2O_3 (99%, High Purity Chemicals) as a reference. In addition, approximately 100 mg of each metal carbodiimide powder was uniaxially pressed into a pellet with a diameter of 5.9 mm at about 46 MPa to study their melting behaviors. This process was conducted in a glove box filled with a dry nitrogen to avoid their reaction with moisture and oxygen in air. Each pellet on an alumina boat was heated in an alumina tube furnace under a flowing nitrogen at 800, 900, 1000, 1100, 1330, or 1350 °C for 5 h.

Computational studies

DFT calculations were carried out employing the program VASP (*Vienna ab initio simulation package*) [45] in order to obtain optimized structures and electronic total energies. Plane-wave basis sets with an energetic cut-off of 500 eV were used. Exchange and correlation were treated following the generalized gradient approximation. [46] To account for van-der-Waals like interactions, the D3 method of Grimme was applied. [47] All the unit cells were allowed to change their volumes and shapes during the relaxation process but keeping the initial symmetry.

Phonon computations were conducted using the program PHONOPY [48] based on the Hellmann-Feynman forces calculated using VASP. The supercells for the force calculations were set up by multiplying the unit cells in each direction such that the lattice parameters of the supercells were well above 1 nm. Thermodynamic potentials were obtained in the framework of the quasi-harmonic approximation following the procedure described in Refs. 49 and 50. The calculations were conducted for the crystal structures of all the alkaline-earth metal carbodiimides, alkaline-earth metals, graphite, and crystalline nitrogen. [23,40,41,51-58]

Preparation of $Sr_{1-x}Ba_xTaO_2N$ microcrystals

Phase-pure orange $SrTaO_2N$ perovskite powder was obtained by ammonolysis of the $Sr_2Ta_2O_7$ precursor obtained by solid state reaction of $SrCO_3$ and Ta_2O_5 (FUJIFILM Wako Pure Chemical, 99.9%), using a previously reported procedure. [59] $SrTaO_2N$ powder was mixed with t-$BaCN_2$ at its concentrations of 5, 10, 30, or 50 wt% in a glovebox filled with a dry nitrogen. About 200 mg of each mixture was uniaxially pressed into a pellet in a diameter of 5.9 mm at approximately 46 MPa. Then they were heated under flowing nitrogen at around 900 °C and were kept at this temperature for 5, 10, 30, or 50 h. Both heating and cooling were conducted at a rate of 200 °C/h. Reddish solids were obtained after cooling. Weight losses during annealing were small enough to be ignored. Fracture surface of each product was polished with 1000-grit sandpaper having SiC particle sizes in the range of 2 to 3 μm. The polished surface was etched with 1 M citric acid for 2 days to remove excess solidified $BaCN_2$ and soluble impurities on the surface, after which the surface was washed with distilled water and hexane (96%, FUJIFILM Wako Pure Chemical). The microstructures of the etched surface were observed using scanning electron microscope (SEM, JSM-6390 LVS, JEOL). Afterwards, grown up crystals were separated from the solids by their washing in 1 M nitric acid for one day. They were then washed with distilled water to remove the residual acid. Orange-

red perovskite crystals were obtained by their filtration using filter paper with pore diameters smaller than 110 μm (Toyo Roshi K. K.).

Characterization of the $Sr_{1-x}Ba_xTaO_2N$ microcrystals

Crystalline phases of the solid surface and the orange-red powder products obtained by filtration were identified with XRD of Cu Kα radiation. Lattice parameters were refined for the √2×√2×2 tetragonal superlattice of a primitive perovskite cell using the XRD data obtained from 2θ values of 10° – 120° measured with a 0.02° step size and a count time of 5.0 sec. The Rietveld calculations [43] were employed for lattice parameter calculations.

The solid products contained oxynitride perovskite $Sr_{1-x}Ba_xTaO_2N$ as their main crystalline phase, together with a trace amount of residual $BaCN_2$. The electrical properties of the solid fabricated using 30 wt% of $BaCN_2$ at 900 °C for 30 h were studied under nitrogen atmosphere using an LCR meter (4274A, Hewlett Packard) over a frequency range of $10^2 – 10^5$ Hz at room temperature. Ag paste (4922N, Du Pont) was applied to the polished flat surfaces of the solid product as electrodes.

X-ray fluorescence spectroscopy (XRF, SEA 6000, Hitachi) was used for the analyses of cations, and combustion analyzer (EMGA-620W, Horiba) was employed for the oxygen/nitrogen contents using Si_3N_4 and Gd_2O_3 as references. Nitrogen content of

Si_3N_4 was certificated to be 38.5 wt% by Ceramic Society of Japan. Commercially available Gd_2O_3 (99.9%, FUJIFILM Wako Pure Chemical) was used after its calcination up to 1000 °C to remove its adsorbates. CHN analyses were also performed to determine carbon contents. An electron probe micro analyzer (EPMA, JXA-8530F, JEOL) was used for preliminary compositional analyses. ICP-AES was employed to analyze the acidic solutions after removing the powder product by filtration.

The microstructures of both the solid products and the powders after washing in acidic solution were examined by using SEM, scanning transmission electron microscope (STEM, HD-2000, Hitachi), and transmission electron microscope (TEM, JEM-2010, JEOL). Thin specimens for STEM and TEM observations were obtained using a focused gallium ion beam (FIB, JIB-4600F/HKD, JEOL). Each sample was mounted on a molybdenum grid with a trace amount of epoxy resin after which tungsten was deposited on the sample surface prior to slicing. Elemental distributions in the grains were determined with energy dispersive X-ray spectroscopy (EDX, JEM-2010F, JEOL) attached to TEM.

4-3. Results and discussion

Melting and thermal decomposition of α-SrCN$_2$

Powder XRD patterns of the as-prepared α-SrCN$_2$ and its annealing products are depicted in **Fig. 4-3**. Single phase of white α-SrCN$_2$ powder was obtained by ammonolysis reaction of SrCO$_3$. Thermal behavior of α-SrCN$_2$ was examined using TG-DTA under flowing nitrogen. The α-SrCN$_2$ showed a large endothermic peak starting at 1020 °C without weight loss, as shown in DTA graph of **Fig. 4-4**. The shoulder of the lower temperature region (indicated with an asterisk) is attributed to melting of α-SrCN$_2$ and the larger endothermic peak may be due to the melting of Sr metal. After the melting, a slight weight loss began at 1070 °C. The black annealed product after TG-DTA measurement contained SrC$_2$ and Sr(OH)$_2$ as the main phases. SrC$_2$ was generated by the decomposition beginning at slightly higher temperature than the melting point of SrCN$_2$. Sr(OH)$_2$ may have been generated due to the hydrolysis reaction of SrCN$_2$ or the decomposition products such as strontium metal after taking out from furnace.

Melting behavior and polymorphism of BaCN$_2$

Crystal structure of BaCN$_2$ prepared by ammonolysis is tetragonal phase. [40] An endothermic DTA peak was observed at 910 °C on the t-BaCN$_2$ upon heating under N$_2$, as depicted in **Fig. 4-5**. This sample also showed a slight weight loss less than 0.3%

above 910 °C, which is either due to a thermal decomposition of a residual $BaCO_3$ or a slight vaporization of $BaCN_2$. These data confirm that t-$BaCN_2$ melts at a temperature slightly below the nitrogen release from oxynitride perovskites such as $SrTaO_2N$ and $BaTaO_2N$. Decomposition of $BaCN_2$ to a mixture of BaC_2 and Ba metal was not observed below 1000 °C. Its decomposition temperature could not be determined because molten $BaCN_2$ gradually evaporated during experiments.

The Gibbs energies were calculated for both the rhombohedral and tetragonal phases of $BaCN_2$. t-$BaCN_2$ was more stable than the r- phase by approximately 20 kJ/mol over the entire temperature range of -273.15 to 1227 °C (0 to 1500 K) as shown in **Fig. 4-6**. Because the rhombohedral phase with distorted BaN_6 octahedra [23] is less stable than the tetragonal phase [40], only the more stable t-$BaCN_2$ was taken into account in the following discussion.

White solidified product after annealing and cooling of t-$BaCN_2$ at a rate of 10 °C/min contained r-$BaCN_2$ as shown in **Figs. 4-7(a)** and **(b)**. The transformation mechanism between these crystal structures is still unclear. Several XRD peaks of $Ba(OH)_2$ were detected in the annealed product. $Ba(OH)_2$ was formed probably because of the reaction of BaO generated by thermal decomposition of residual $BaCO_3$ in the as-prepared $BaCN_2$ after taking out from furnace. Simple hydrolysis reaction of $BaCN_2$
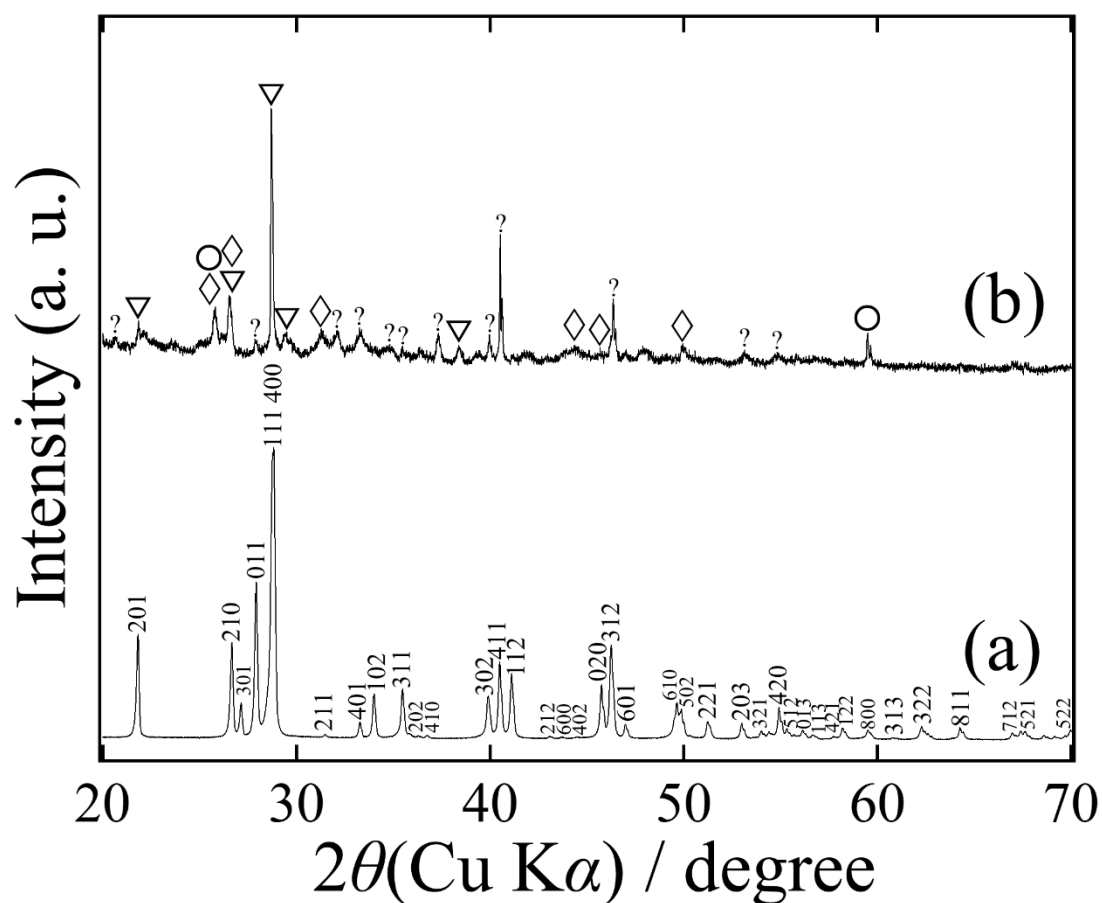
Fig. 4-3. XRD patterns of **(a)** α-SrCN$_2$ powder and **(b)** its annealed sample. α-SrCN$_2$ was annealed at approximately 1100 °C for 5 h. Indexed diffraction peaks shown in **(a)** are α-SrCN$_2$ (JCPDS 51-541). Inverse triangles, diamonds, circles, and question marks indicate Sr(OH)$_2$ (ICSD 26029), graphite (ICSD 53781), SrC$_2$ (JCPDS 3-0542), and unknown phases, respectively.
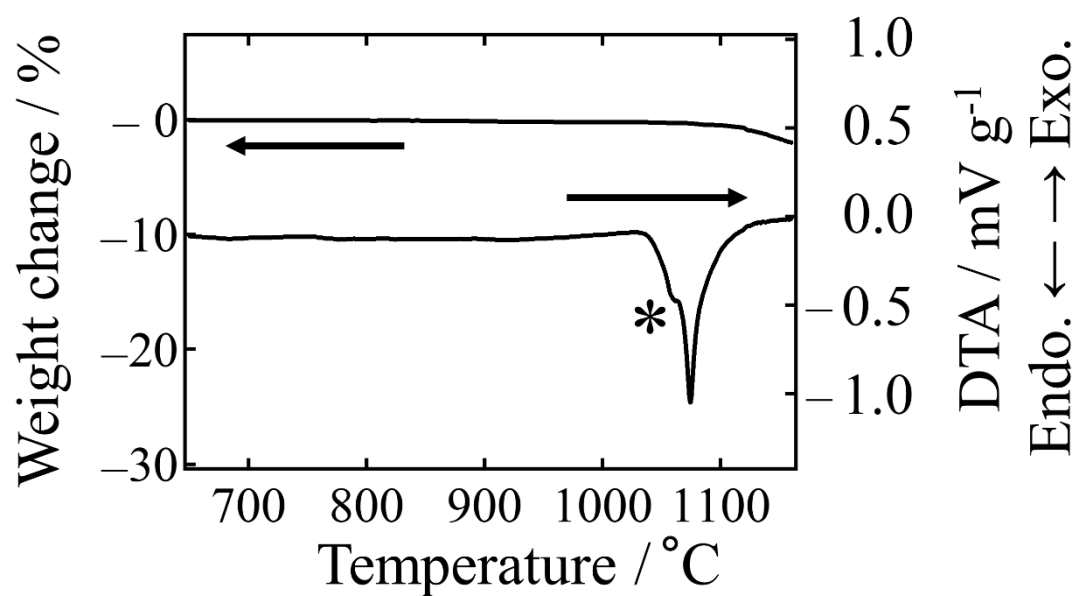
Fig. 4-4. TG-DTA curves obtained from α-SrCN$_2$ under a nitrogen flow. Asterisk indicates the endothermic event associated with melting.
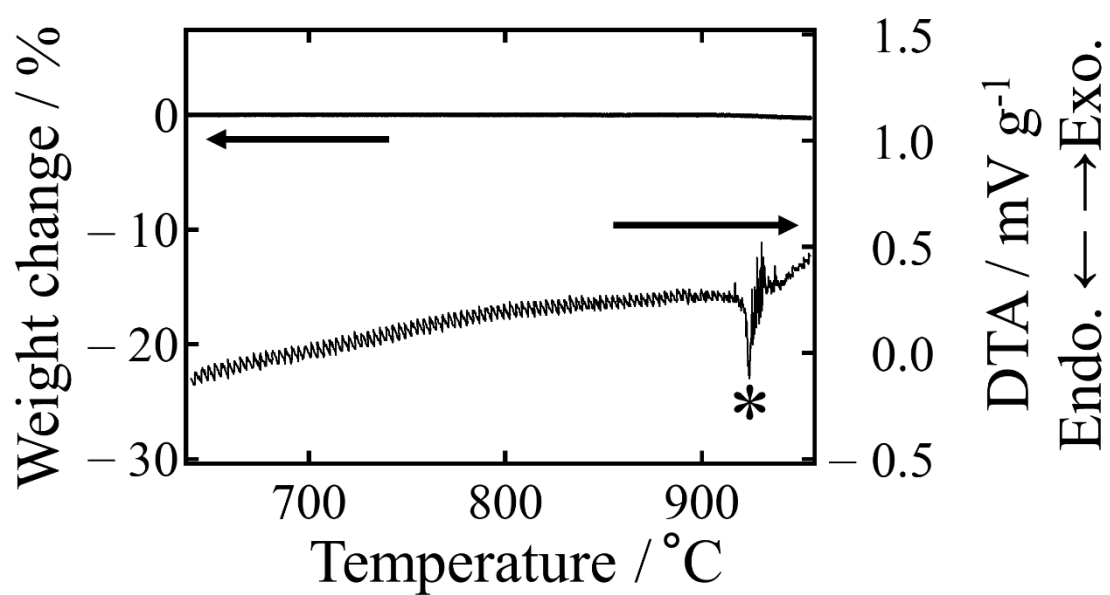
Fig. 4-5. TG-DTA curves obtained from *t*-BaCN$_2$ under a nitrogen flow. Asterisk indicates the endothermic event associated with melting.
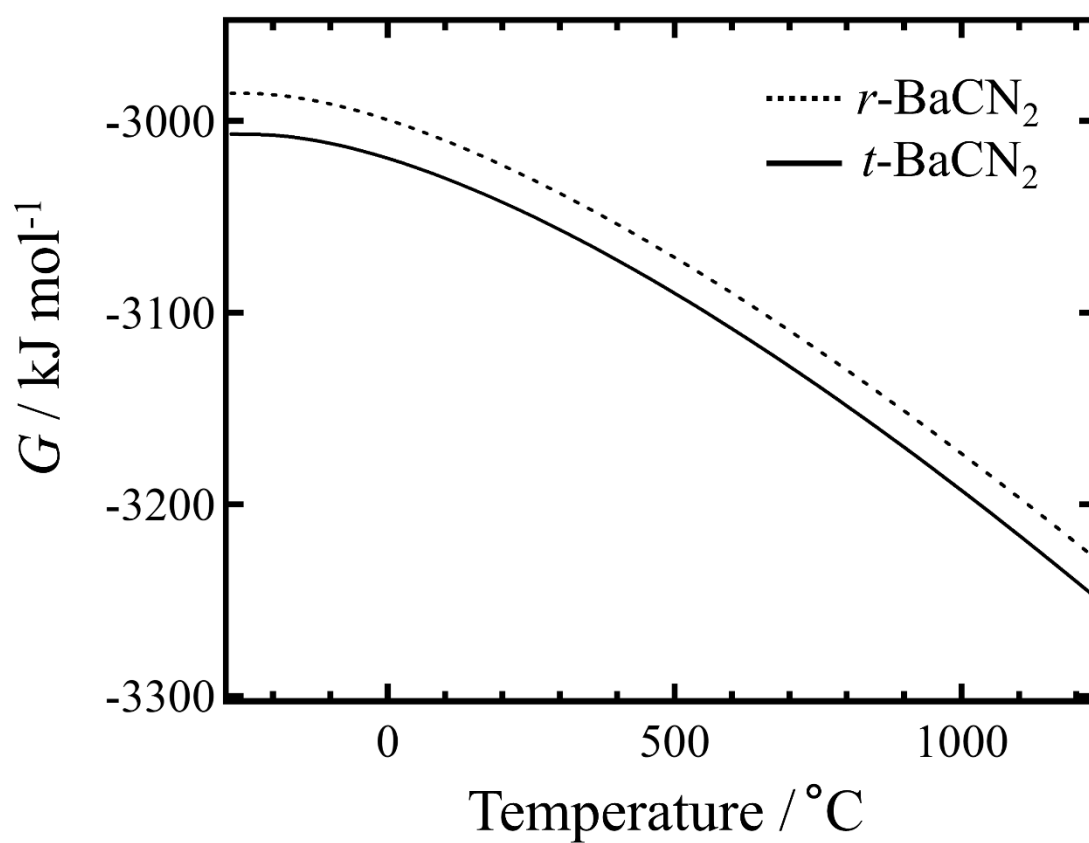
Fig. 4-6. Calculated Gibbs energy values of r- and t-BaCN$_2$ as functions of temperature. Broken and solid lines are r- and t- phases, respectively.
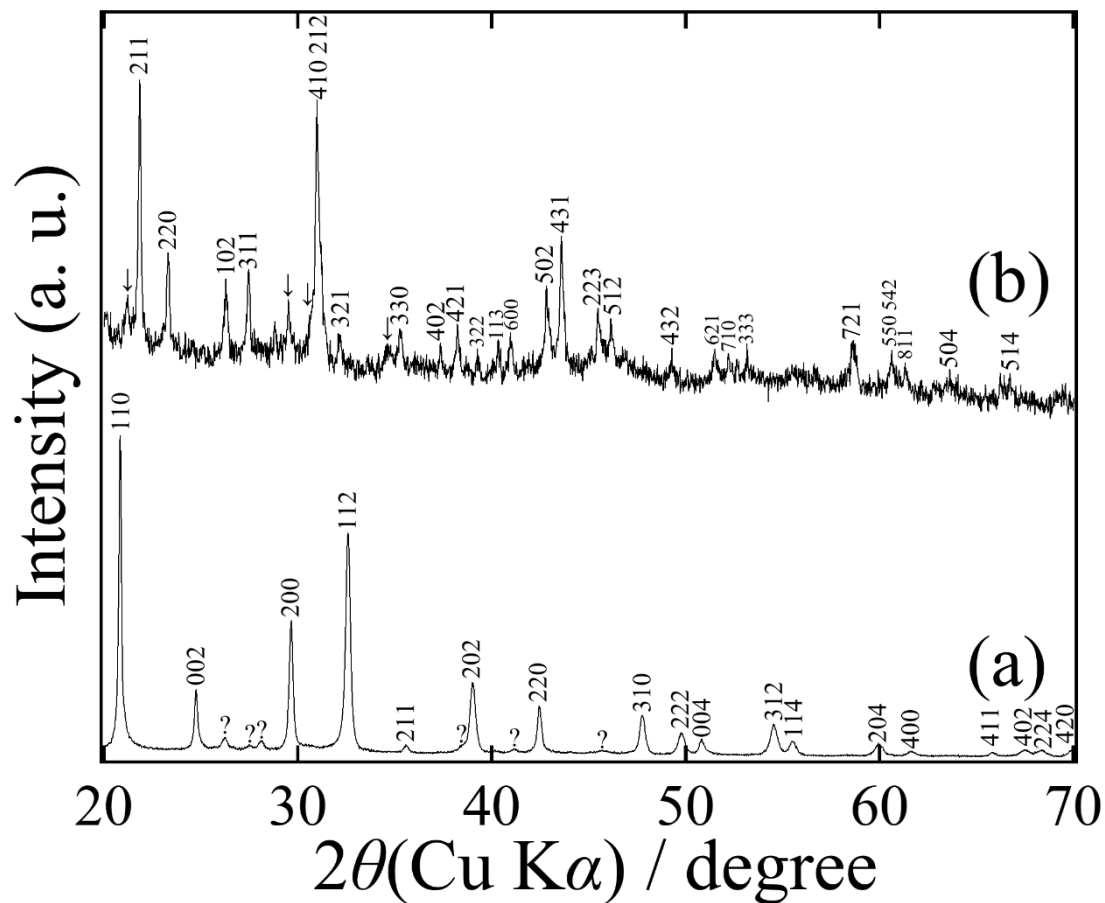
Fig. 4-7. XRD patterns of *t*-BaCN$_2$ powders for **(a)** the as-prepared and **(b)** the annealed samples at approximately 900 °C for 5 h. Indexed diffraction peaks in **(a)** are *t*-BaCN$_2$ [40] and those in **(b)** are *r*-BaCN$_2$ (JCPDS 51-542). [23] Arrows and question marks indicate Ba(OH)$_2$ (ICSD 56828) and unknown phase (probably orthorhombic phase of BaCN$_2$, which has not been published yet), respectively.
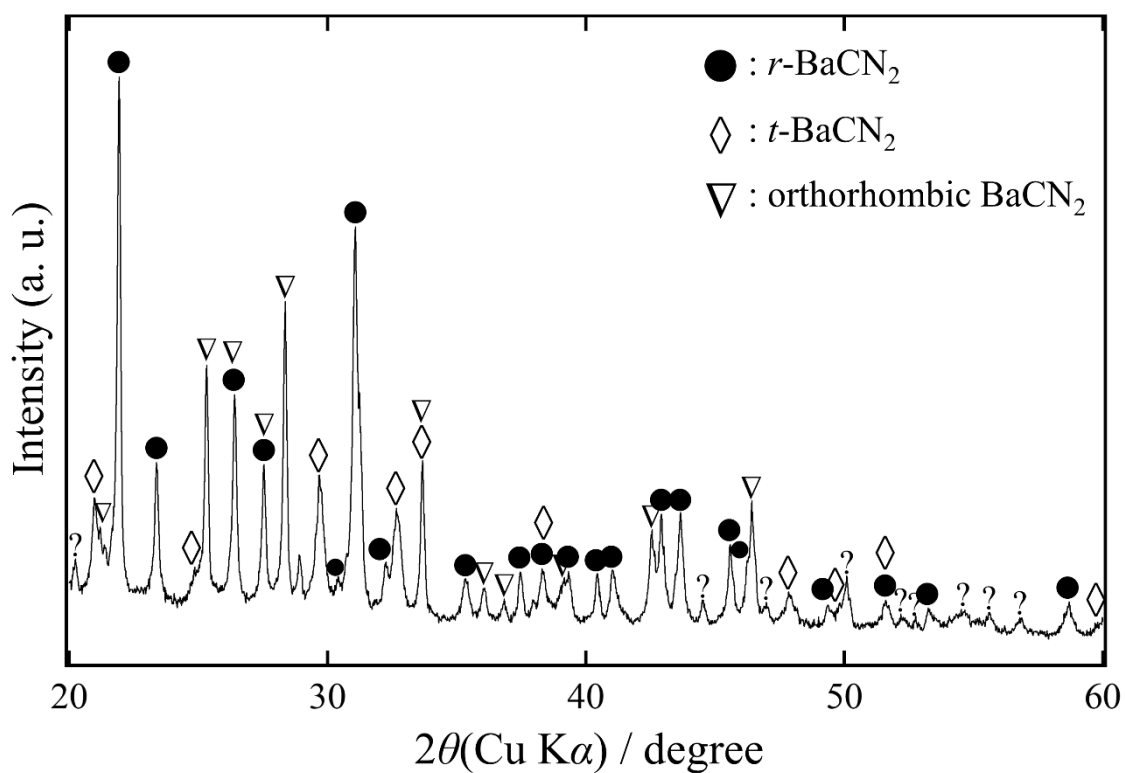
Fig. 4-8. Powder XRD profile of the BaCN$_2$ sample cooled down from 910 °C at a rate of 1.8 °C/h. Filled circles, diamonds, inverse triangles, and question marks indicate r-BaCN$_2$ (JCPDS 51-542) [23], t-BaCN$_2$ [40], unpublished orthorhombic BaCN$_2$, and unknown phases, respectively.

is also a possible way to give $Ba(OH)_2$. Considering the fact calculation results indicate that *t*- phase is more stable one (**Fig. 4-6**), formation of *r*- phase upon heating and cooling of $BaCN_2$ melt seems to be contradictory. Additional slow cooling experiment from 910 °C at a rate of 1.8 °C/min was performed for the $BaCN_2$ melt on an alumina boat and tetragonal phase as well as one more novel polymorph of $BaCN_2$, orthorhombic $BaCN_2$ were generated in the solidified sample, as shown in **Fig. 4-8**. This suggests that the tetragonal phase is more stable than rhombohedral one. It seems to take very long time to increase the phase purity of *t*-$BaCN_2$ by cooling $BaCN_2$ melt. A similar phase transition of nitrogen-containing compound influenced by the cooling rate is reported in the *α* and *β* phases of Li_3BN_2. [60]

Melting and thermal decomposition of CaCN₂

TG measurement under nitrogen flow was conducted on $CaCN_2$ powder containing 18 wt% of $CaCO_3$ mentioned above in an alumina crucible using a TG-DTA equipment. There was no significant weight change between 600 and 1000 °C as shown in **Fig. 4-9**, although a slight weight loss related to a desorption of the surface adsorbate was observed below 600 °C. Thermogravimetry at higher temperature was not conducted because the decomposition reaction of $CaCN_2$ is so intense that the TG equipment can be broken. Additional thermal studies were conducted by heating approximately 100 mg of

CaCN$_2$ powder compacts in an alumina tube furnace. CaCN$_2$ compacts with a diameter of 5.9 mm were fabricated by uniaxial pressing at 46 MPa and then they were put on an alumina boat in a flowing nitrogen. The samples were heated either to 1330 or 1350 °C, which were slightly lower or higher than the reported melting point of CaCN$_2$ (1340 °C) [61] for 5 h. The sample changed from white powder to black solidified mass in the heating at 1350 °C. It was a mixture of CaCN$_2$ and CaO, but the CaO amount increased from the starting material as depicted in **Fig. 4-10(b)**. The Ca metal in the thermally decomposed product was oxidized to CaO in picking up the product from the furnace. A trace amount of CaC$_2$ was also detected in the black solidified product. There was no apparent change on the heated product at 1330 °C. CaCN$_2$ was assumed to melt at approximately 1340 °C as previously reported [61] and almost simultaneously decomposed to a mixture of CaC$_2$, Ca metal, and nitrogen. The thermal decomposition was not completed at 1350 °C and much amount of CaCN$_2$ remained. Similar decomposition behavior was observed in the case of α-SrCN$_2$. The possibilities of side reactions were considered by some researchers and they reported the experimental results of the formation of a trace amount of Ca$_3$N$_2$ during heating CaCN$_2$ at 1000 – 1200 °C, but its proportions in the fired products are very small (less than 2%). [62] Moreover, no generation of Ca$_3$N$_2$ was observed in heating CaCN$_2$ at above 1250 °C [62], which does

not contradict to our experimental results. So, we would like to assume that the amount of Ca_3N_2 formed in the heating procedure is small enough to ignore.

The $CaCN_2$ and α-$SrCN_2$ powder compacts completely melted losing their original shape when they were annealed at 1350 and 1100 °C, respectively. However, their color changed from original white to black due to thermal decomposition. Conversely, t-$BaCN_2$ melted slightly above 900 °C but it remained as a white $BaCN_2$ solid mass at the bottom of alumina boat after cooling. These results also confirm that t-$BaCN_2$ starts to melt at approximately 900 °C without decomposition. It is suitable for the sintering and crystal growth of oxynitride perovskites.

Computational study of the stability of alkaline-earth metal carbodiimides

Thermal decomposition reaction of alkaline-earth metal carbodiimides can be expressed as follows;

$$2AECN_2 \rightarrow AEC_2 + AE + 2N_2 \qquad (4\text{-}1)$$
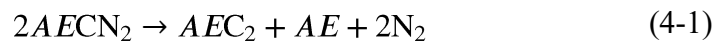
where AE indicates alkaline-earth metal. Decomposition temperature of metal carbodiimides will be able to be estimated by calculating the Gibbs energy values of the reaction (4-1). The parameters of the stability of crystal structure of ionic crystals are very useful to compare their melting points and decomposition temperatures. Pseudo-bonding dissociation energy values (H_{bond}) were calculated at -273.15 °C (0 K) and 0 Pa
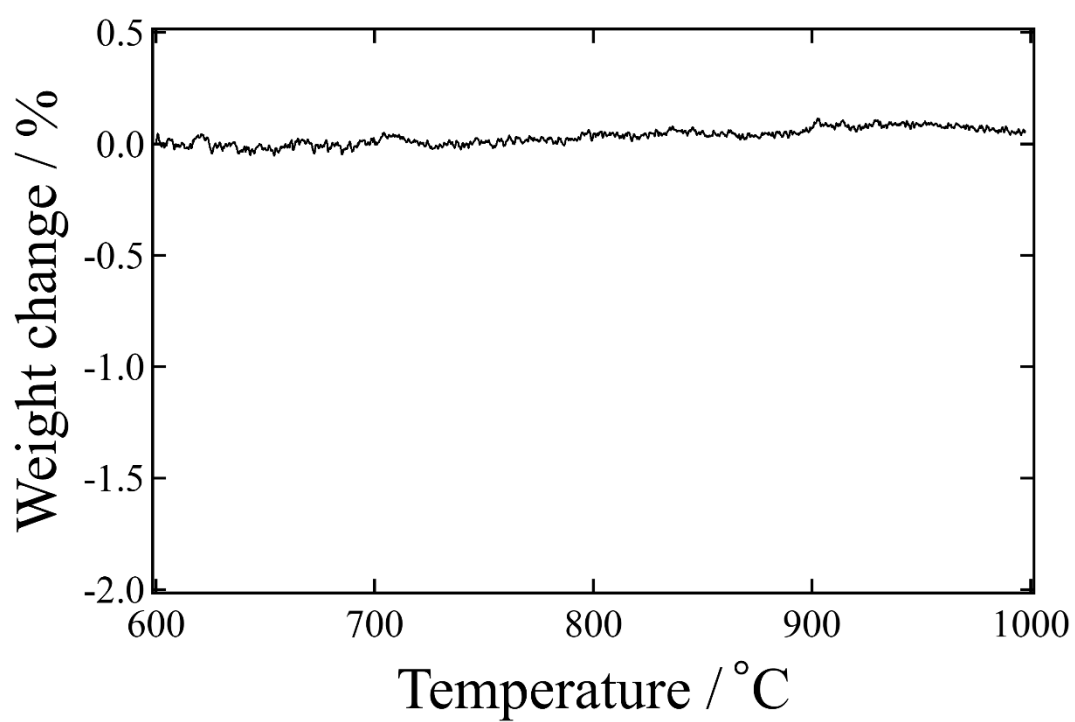
Fig. 4-9. TG curve of CaCN$_2$ powder contaminated with approximately 18 wt% of CaO. The sample was heated at a rate of 10 °C/min under flowing nitrogen.
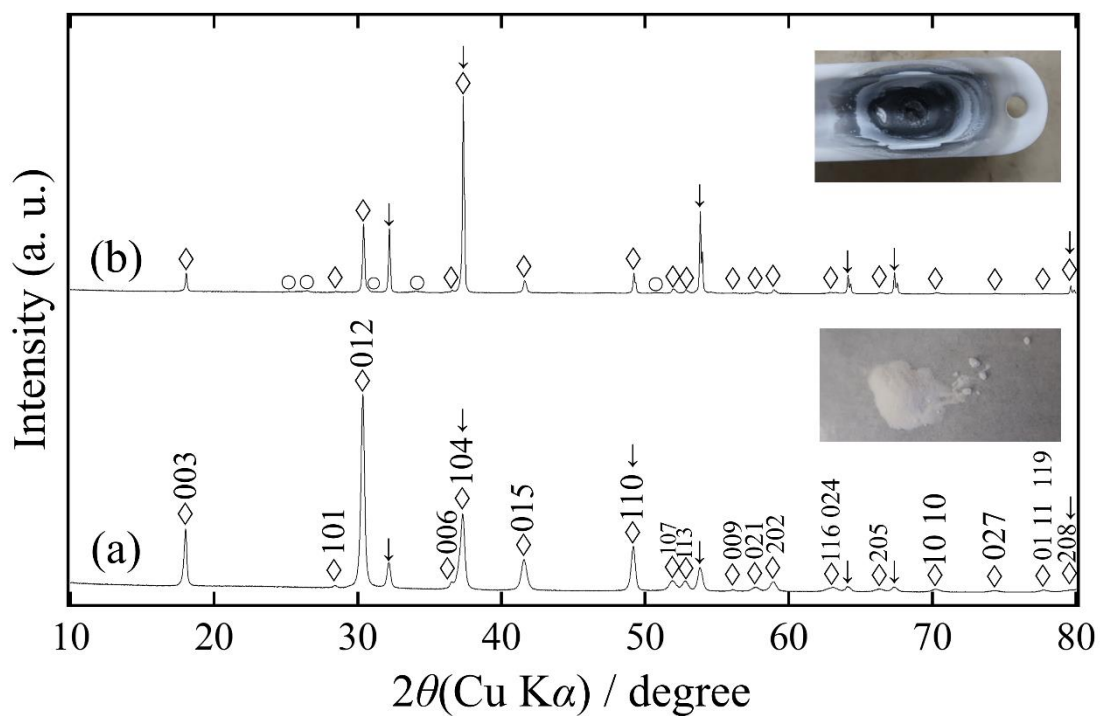
Fig. 4-10. XRD patterns and photographs of the mixture of $CaCN_2$ and CaO. **(a)** the as-prepared powder obtained by the ammonolysis of $CaCO_3$ powder at 600 °C for 10 h. **(b)** ground powder of the black solid after heating at 1350 °C for 5 h. Diamonds, arrows, and circles indicate $CaCN_2$ (ICSD 25763), CaO (PDF 00-037-1497), and CaC_2 (ICSD 252755), respectively.

113

by the total-energy calculations of AECN$_2$ and single atoms of alkaline-earth metal, carbon, and nitrogen.

$$H_{bond} = E_0(AECN_2) - \{E_0(AE) + E_0(C) + 2E_0(N)\} \qquad (4\text{-}2)$$

Where E_0 values indicate the calculated potential energies of the metal carbodiimide and single atoms of its constituents. Calculated bonding energy values (H_{bond}) are summarized in **Table 4-1**. It gradually decreased with the experimentally determined melting points in an order of CaCN$_2$, α-SrCN$_2$, and t-BaCN$_2$ with an increase in ionic radii of alkaline-earth metal ions.

Gibbs energy values of each material at high temperature were obtained with phonon simulation in combination with quasi-harmonic approximation. [48] Calculation for gaseous nitrogen was performed by summing up the electronic total-energy E_0, vibrational zero-point Helmholtz free energy $A_{ph,0}$ calculated for crystalline α-nitrogen [55], literature values of the sublimation enthalpy ΔH_{sub}, entropy S, and the heat capacity $C_p(T)$ of gaseous nitrogen. [61] The following equation was employed as in previous publication. [63]

$$G(N_2) = E_0 + A_{ph,0} + \Delta H_{sub} - TS + \int C_p(T)dT \qquad (4\text{-}3)$$

Gibbs energy values are plotted for the decomposition reaction (4-1) in **Fig. 4-11**. The temperature where the spontaneous decomposition of the alkaline-earth metal

carbodiimide begins is the point of $\Delta G_r = 0$. The estimated decomposition temperatures of $CaCN_2$, α-$SrCN_2$, and t-$BaCN_2$ were 997, 951, and 912 °C, respectively. This means that both of $CaCN_2$ and α-$SrCN_2$ decompose below their melting points shown in **Table 4-1**. It is well known that the thermochemical behaviors of solid strongly depend on the lattice enthalpy values. [64] The decomposition temperature changed with the ionic size of alkaline-earth metals similarly to the melting points. The melts of $CaCN_2$ and α-$SrCN_2$ were not stable and they decompose rapidly in the present experimental study. The calculated decomposition temperature of t-$BaCN_2$ was 912 °C, which was slightly higher than the melting point (910 °C). Only the $BaCN_2$ melt is stable above its melting point to be used as a flux for crystal growth and sintering of alkaline-earth oxynitrides.

Preparation of the microcrystals of $Sr_{1-x}Ba_xTaO_2N$ using a $BaCN_2$ melt

Compacts made of mixtures of $SrTaO_2N$ with t-$BaCN_2$ powder at various ratios were annealed. Their color changed from orange to reddish-orange or red during heating. The volume of the initial green-$SrTaO_2N$ powder compact mixed with 30 wt% of oxynitride perovskite with the chemical composition of $Sr_{0.83}Ba_{0.17}TaO_2N$. The molar ratios of cations were determined using XRF. Oxynitride powder compacts without $BaCN_2$ did not densify during heating at 900 °C and their relative densities remained about 50%. This indicates that addition of $BaCN_2$ is effective to promote the densification
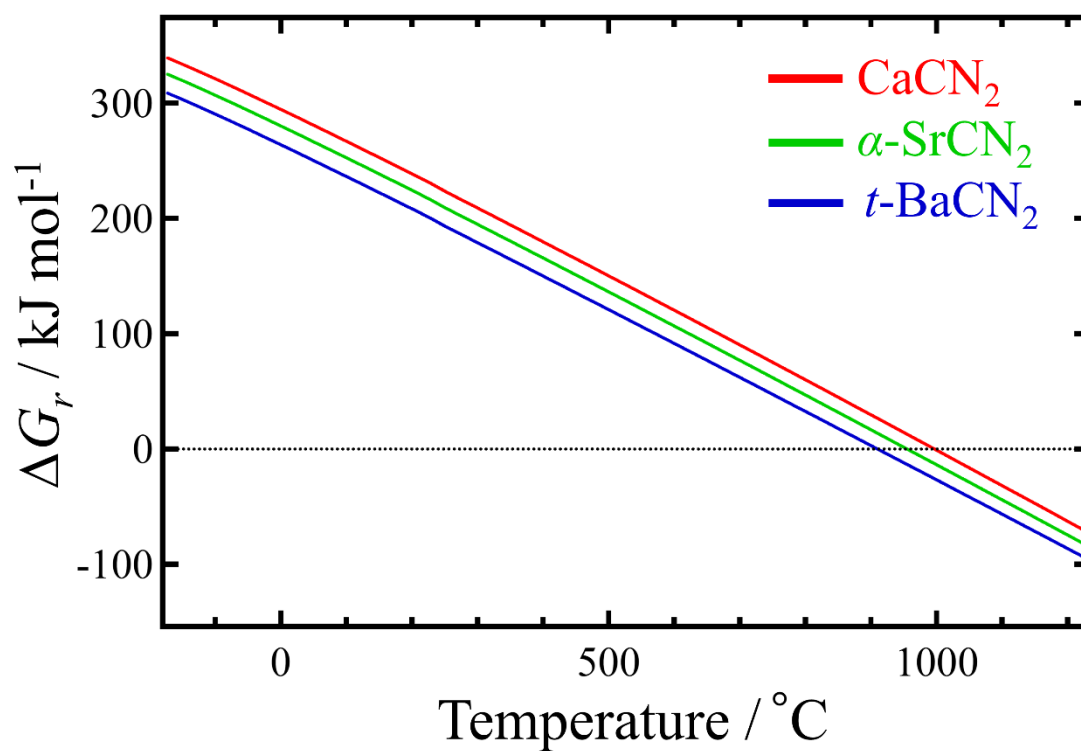
115

Fig. 4-11. Decomposition reaction Gibbs energies of alkaline-earth metal carbodiimides as functions of temperature. Red, green, and blue lines indicate $CaCN_2$, α-$SrCN_2$, and t-$BaCN_2$, respectively.

Table 4-1. Pseudo-bonding energy values (H_{bond}) and melting points of alkaline-earth metal carbodiimides.

Compound	H_{bond} / kJ mol^{-1}	Melting point / °C
$CaCN_2$	2045	1340 [61]
α-$SrCN_2$	2014	1020
t-$BaCN_2$	2012	910

of oxynitride perovskite bulks. Some improvements of sintering process such as applying pressure will be necessary to achieve further densification of oxynitrides.

Electrical properties of the ceramics with RD of 68.9% were investigated. A complex impedance plot was obtained for the abovementioned product, and it is depicted in **Fig. 4-12**. This plot exhibits only a part of a large circle, suggesting the large electrical resistivity of the solid. The data in **Fig. 4-13** demonstrate that relative dielectric constant values of the solid ranged $68 - 90$ over the frequency range of $10^2 - 10^5$ Hz. These values are slightly lower than those previously reported for post-ammonolysis products of $SrTaO_2N$ ceramics sintered at high temperature. [59] This may be because the presence of a small amount of residual $BaCN_2$ flux lowered the volume fraction of $SrTaO_2N$ in the present ceramic product. Dielectric loss values of the ceramics were less than 0.11. These dielectric loss values, together with the Cole-Cole impedance plot described above, indicate that an electrically insulating ceramics was obtained without losing nitrogen from oxynitride perovskite by using $BaCN_2$ flux at approximately 900 °C.

Microstructures of the as-prepared $SrTaO_2N$ powder and fracture surface of the solid product fabricated with 30 wt% t-$BaCN_2$ were observed. The observations were performed before and after etching in citric acid. The as-prepared $SrTaO_2N$ powder was found to be composed of irregularly shaped, rounded particles $40 - 200$ nm in size, as
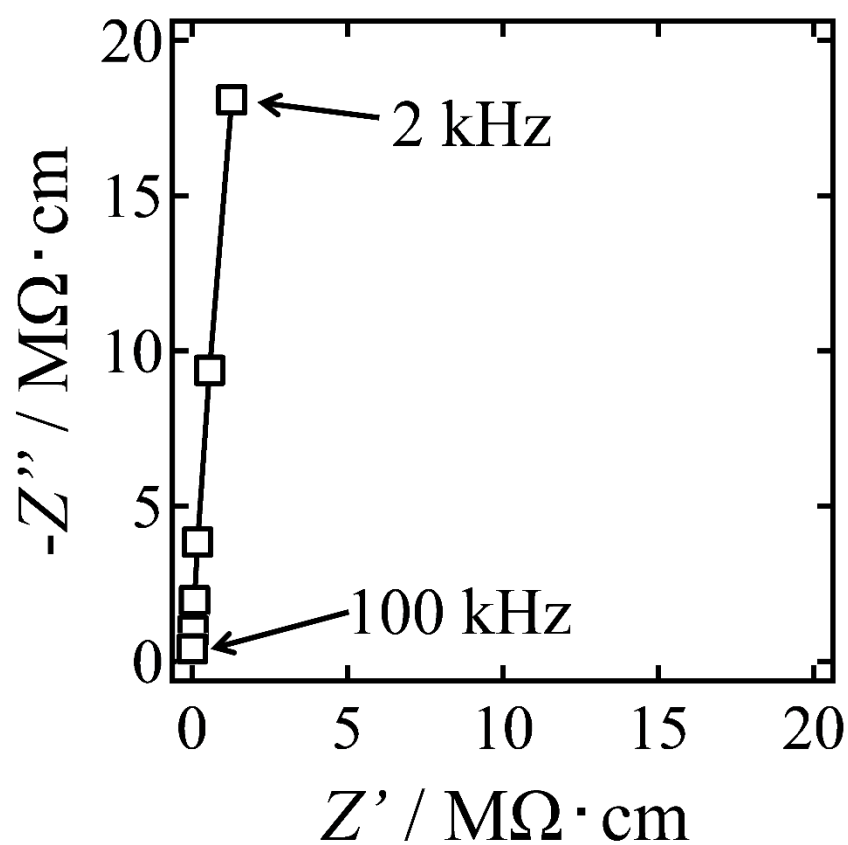
Fig. 4-12. Complex impedance plot of the solid product with a relative density of 68.9% at room temperature. The associated error bars are smaller than the symbol sizes and so are not provided.
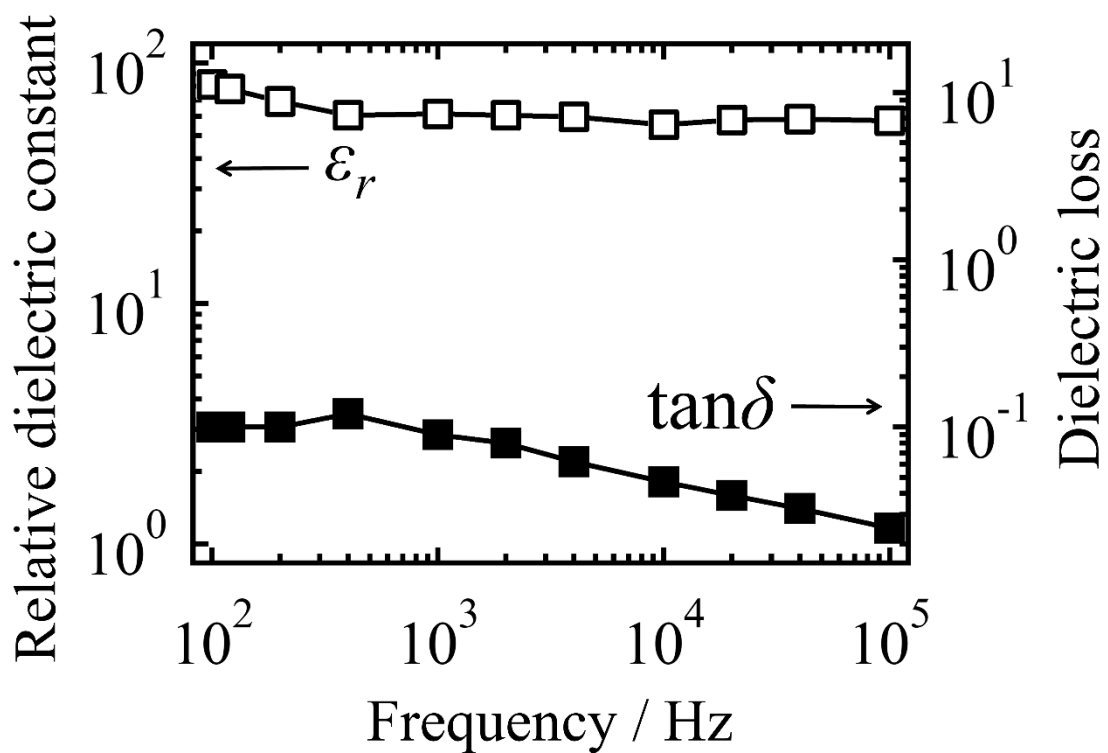
Fig. 4-13. Relative dielectric constant and loss values of the solid product with a relative density of 68.9% as functions of frequency at room temperature. The associated error bars are smaller than the symbol sizes and so are not provided.

shown in **Fig. 4-14(a)**. After heating $SrTaO_2N$ together with 30 wt% t-$BaCN_2$ at 900 °C

for 30 h under nitrogen flow, the shape changed to be slightly angular and the particles

were embedded in the solidified mass, as depicted in **Fig. 4-14(b)**. Cuboid or cubic

particle shapes became evident after the citric acid etching as shown in **Fig. 4-14(c)**. Its

higher magnification image in **Fig. 4-14(d)** demonstrates that the angular crystals were

connected with one other along their straight boundaries.

The color of the products obtained after washing in nitric acid gradually

changed from orange in the original $SrTaO_2N$ to red with increase in the amount of

$BaCN_2$ flux in the starting mixtures, as shown in **Fig. 4-15**. The chemical compositions

of these powder products were estimated using XRF in combination with combustion

analysis, and the results are summarized in **Table 4-2**. These data indicate that total

amount of strontium and barium in each sample was almost equivalent to that of tantalum

in atomic percent. So the products can be represented by the formula $Sr_{1-x}Ba_xTaO_2N$. No

carbon was identified based on a detection limit of CHN analysis (0.3 wt%) in the

products after the nitric acid washing. The crystalline phases of each compound were

oxynitride perovskites as shown in the XRD profiles of **Fig. 4-16**. In each case, all the

diffraction peaks were shifted to lower angles compared to those of the as-prepared

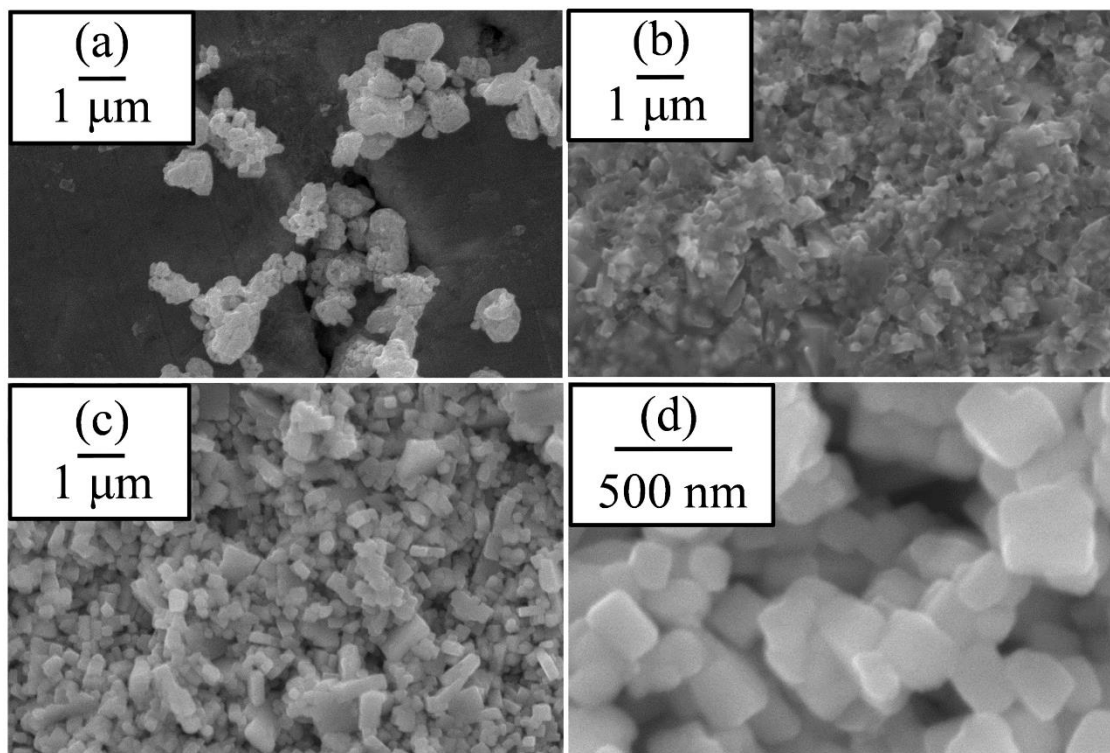$SrTaO_2N$, and it is evident that the perovskite crystalline lattice expanded with increases

Fig. 4-14. SEM images of **(a)** the as-prepared SrTaO₂N powder, **(b)** the fracture surface of the solid obtained after heating a mixed compact made with 30 wt% of BaCN₂, **(c)** the polished surface of the same sample after citric acid etching, and **(d)** a high magnification image of the same etched surface.
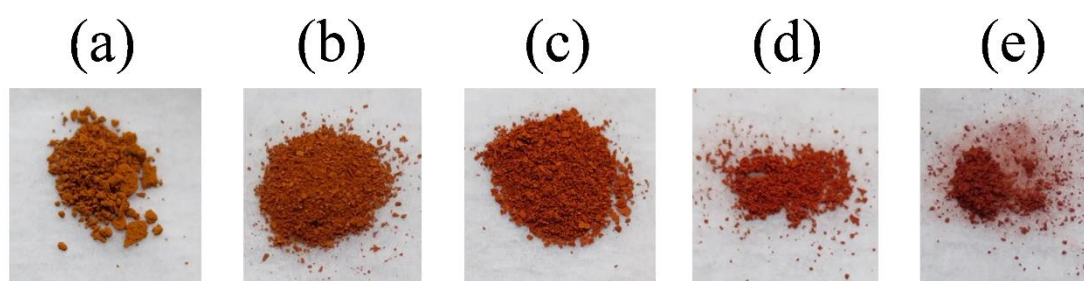
Fig. 4-15. Photographic images of **(a)** the as-prepared SrTaO$_2$N, and the products obtained after washing from heated mixtures made with **(b)** 5, **(c)** 10, **(d)** 30, and **(e)** 50 wt% of BaCN$_2$.

Table 4-2. Elemental contents of the powder products obtained from the mixtures made with various amount of $BaCN_2$ after heating at 900 °C for 30 h. Pure $SrTaO_2N$ and $BaTaO_2N$ were prepared by a solid state reaction under a flow of ammonia. The barium content is represented by x in $Sr_{1-x}Ba_xTaO_2N$.

Preparation condition	Sr / wt%	Ba / wt%	Ta / wt%	O / wt%	N / wt%	Barium content x
5 wt% $BaCN_2$	18.9(1)	0.8(0)	19.7(3)	41.1(2)	19.5(1)	0.04
10 wt% $BaCN_2$	18.2(2)	1.8(2)	19.5(1)	40.6(3)	19.9(1)	0.07
30 wt% $BaCN_2$	17.0(3)	3.4(2)	19.9(2)	40.0(1)	19.7(1)	0.17
50 wt% $BaCN_2$	16.3(1)	4.2(2)	19.8(2)	39.3(3)	20.4(2)	0.23
$SrTaO_2N$(solid state reaction)	19.7(1)	0.0	19.8(2)	41.4(3)	19.1(1)	0.0
$BaTaO_2N$(solid state reaction)	0.0	21.2(2)	21.0(1)	39.4(2)	18.4(1)	1.0

in the amount of $BaCN_2$ in the initial mixtures. The filtrate obtained from the nitric acid washing was found to contain strontium, barium, and tantalum. These results suggest that a portion of strontium in the original $SrTaO_2N$ perovskite was exchanged with barium in the $BaCN_2$ flux to form perovskite-type solid solution $Sr_{1-x}Ba_xTaO_2N$. The color change of the products supports this hypothesis since there is a gradual change in color from orange in the case of $SrTaO_2N$ to red in the case of $BaTaO_2N$. The refined lattice parameters for the tetragonal $\sqrt{2}\times\sqrt{2}\times2$ superlattice of the perovskite ($Z = 4$) are plotted against the barium content (x) in **Fig. 4-17**. These plots indicate a linear transition of lattice parameters between the values for $SrTaO_2N$ and $BaTaO_2N$. Barium ions in the products are in A-site of the perovskite oxynitride. Diffraction peaks were slightly broad and asymmetric on the cation substituted products in **Fig. 4-16**. It may suggest that the strontium exchange to barium was not homogeneous in the oxynitride grains.

The particle shapes and sizes of the products heated at 900 °C for 30 h after the removal of residual $BaCN_2$ were examined and shown in **Fig. 4-18**. Grain growth was not observed in the case of the sample synthesized with 5 wt% of $BaCN_2$, probably because there was insufficient molten $BaCN_2$ to cover the surface of the original $SrTaO_2N$ particles, and an equilibrium between solid and liquid phases was not attained. Angular and cubic particle shapes appeared with increase in the amount of $BaCN_2$ and the particles
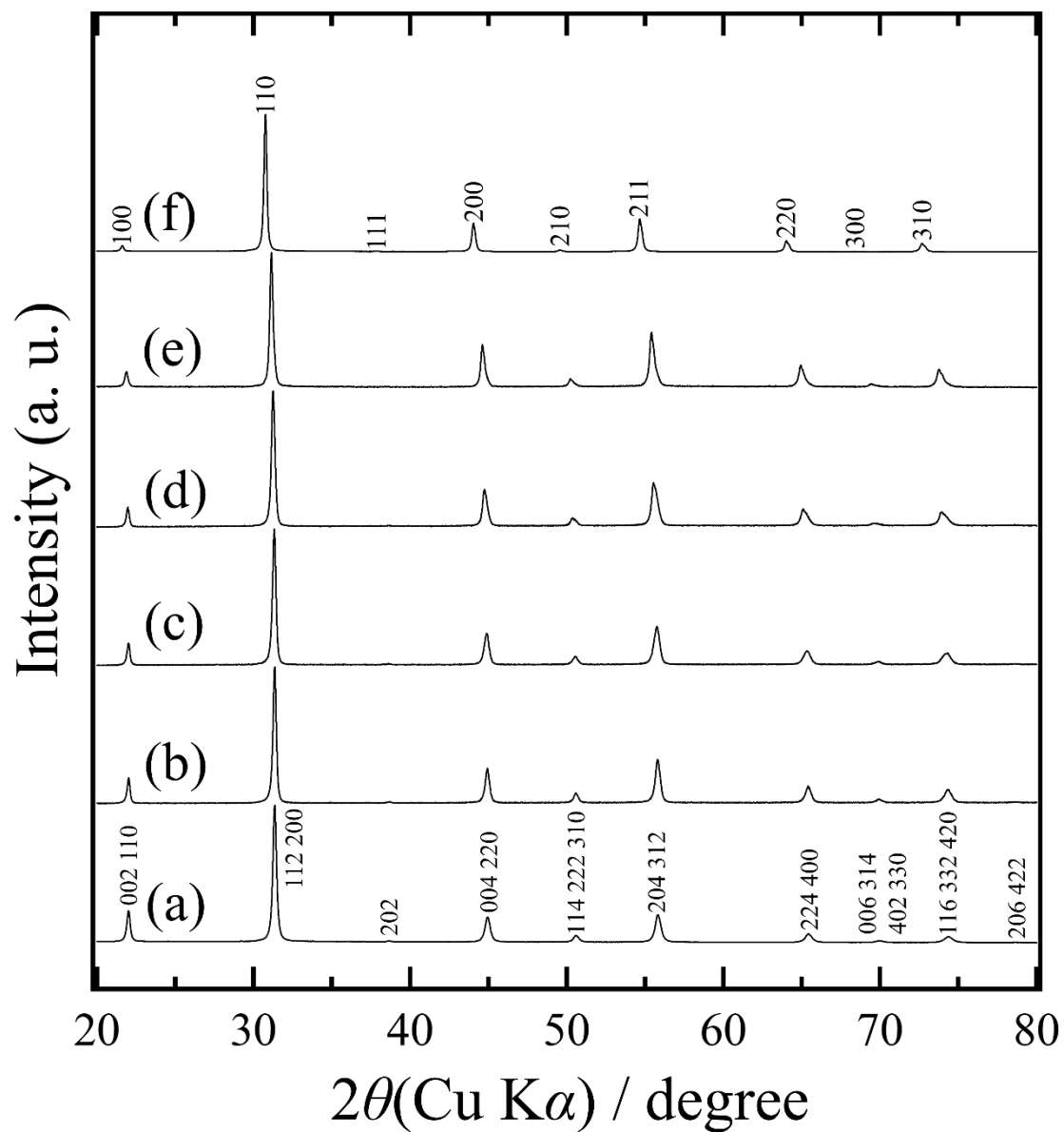
Fig. 4-16. XRD patterns of the $Sr_{1-x}Ba_xTaO_2N$ powder products obtained by heating at 900 °C for 30 h with **(b)** 5, **(c)** 10, **(d)** 30, and **(e)** 50 wt% of $BaCN_2$. Patterns **(a)** and **(f)** are from $SrTaO_2N$ and $BaTaO_2N$ synthesized by the ammonolysis of their respective oxides.
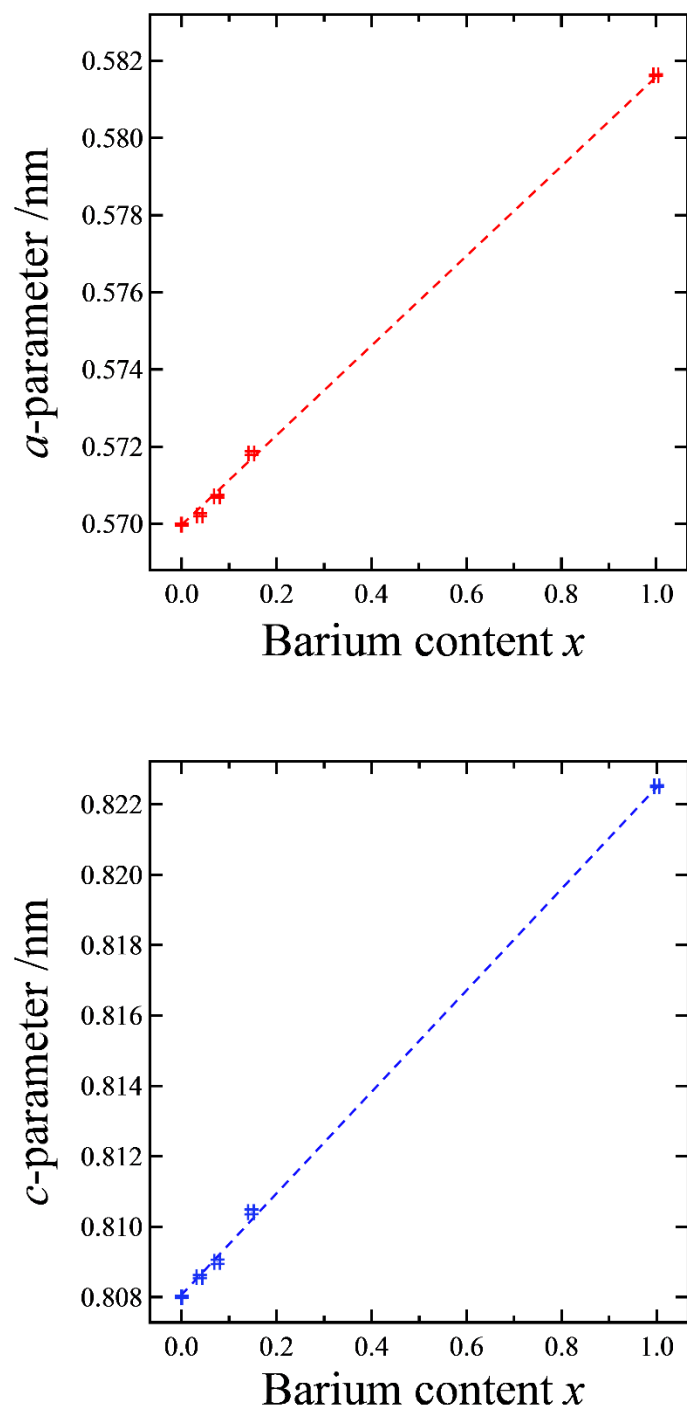
Fig. 4-17. The tetragonal perovskite superlattice parameters as functions of the barium content(x) in $Sr_{1-x}Ba_xTaO_2N$.

simultaneously became larger, as shown in **Figs. 4-18(b)** – **(d)**. The average grain sizes

in the powders were estimated based on analyses of more than 100 particles in SEM

images, and these values are summarized in **Table 4-3**. A sufficient amount of molten

$BaCN_2$ evidently enhanced the crystal growth of the oxynitride perovskite, likely because

the product precipitated more slowly from the more dilute $BaCN_2$ solution. A longer

heating duration was also effective at promoting crystal growth, and the maximum grain

size of 3.7 μm was obtained after heating mixture made with 50 wt% of $BaCN_2$ for 50 h

(**Fig. 4-18(f)**). Some faceting was observed on the surfaces of large crystals. The crystals

grew to sizes that were 20 to 100 times those of the as-prepared $SrTaO_2N$ particles (40 –

200 nm), as shown in **Figs. 4-18(d)** – **(f)**. The crystals were either cuboid or cubic, in

agreement with the perovskite-type structure of $Sr_{1-x}Ba_xTaO_2N$. It appears that a portion

of the original irregular $SrTaO_2N$ particles dissolved to the $BaCN_2$ melt, after which

perovskite crystals with barium-rich compositions precipitated on the undissolved

$SrTaO_2N$ core reflecting a chemical composition of the melt. The larger crystals had more

barium-rich compositions when larger amounts of the $BaCN_2$ flux was employed. The

chemical composition of the melt also gradually changed with the crystal growth and as

noted, the $BaCN_2$ flux removed by washing with nitric acid was found to contain
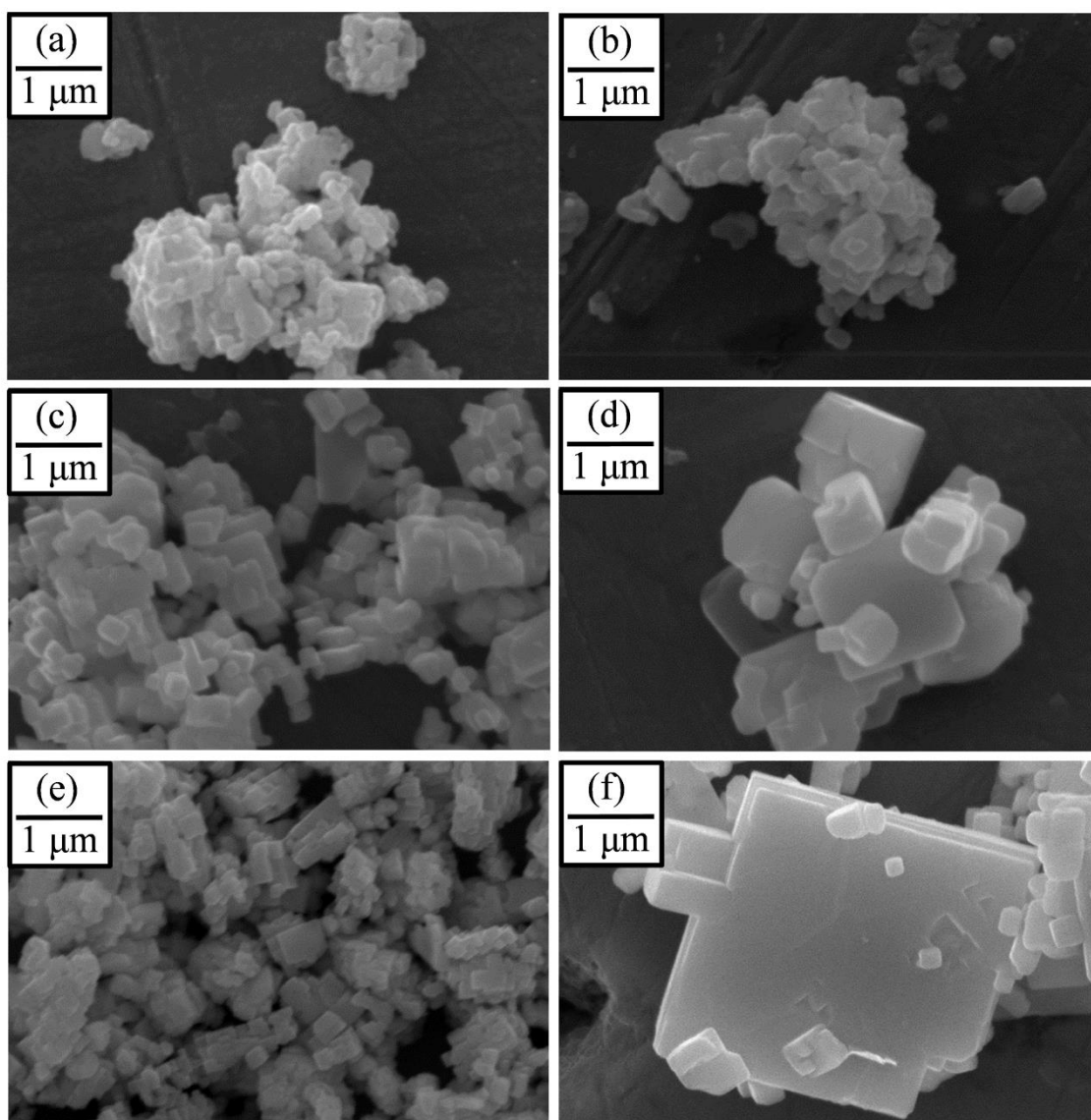
strontium and tantalum.

Fig. 4-18. SEM images of Sr$_{1-x}$Ba$_x$TaO$_2$N powders prepared by heating at 900 °C for 30 h with **(a)** 5, **(b)** 10, **(c)** 30, and **(d)** 50 wt% of BaCN$_2$, and by heating at 900 °C for **(e)** 10 and **(f)** 50 h with 50 wt% of BaCN$_2$.

Table 4-3. The average grain sizes of $Sr_{1-x}Ba_xTaO_2N$ crystals.

Preparation condition	Average grain size / nm
$SrTaO_2N$(As-prepared)	90
$BaCN_2$ 5 wt%, 900 °C-30 h	130
$BaCN_2$ 10 wt%, 900 °C-30 h	180
$BaCN_2$ 30 wt%, 900 °C-30 h	310
$BaCN_2$ 50 wt%, 900 °C-5 h	160
$BaCN_2$ 50 wt%, 900 °C-10 h	440
$BaCN_2$ 50 wt%, 900 °C-30 h	660
$BaCN_2$ 50 wt%, 900 °C-50 h	920

High magnification STEM images of the oxynitride crystals grown in 30 wt% BaCN$_2$ at 900 °C for 30 h are depicted in **Figs. 4-19(a)** and **(b)**. The primary grains are connected with one another through straight boundaries. Grain surfaces evidently became smoother as a result of boundary diffusion during the liquid phase sintering process. The grains and grain boundaries were assessed using electron diffraction analysis. Electron diffraction was observed on the two encircled areas in **Fig. 4-19(c)**. The diffraction pattern generated by the grain in circle**(1)** was indexed as tetragonal Sr$_{1-x}$Ba$_x$TaO$_2$N with an incident electron beam along <110>. The lattice parameters were estimated to be a = 0.571(2) nm and c = 0.811(1) nm. They are in agreement with the values obtained from **Fig. 4-17** using the chemical composition x = 0.17. Additional diffraction spots were observed as represented in **Fig. 4-19(2)** at their grain boundary in the circle**(2)** of **Fig. 4-19(c)**.

The product crystals were observed to grow in size during their recrystallization from the molten BaCN$_2$. TEM-EDX mapping showed that all of the strontium, barium, and tantalum are contained at grain boundary, as shown in **Fig. 4-20**. The relatively large amount of these elements was present in the interiors of both grains and deposited tungsten weakened the signal intensity of all the three elements near the crystal edges especially at the lower right side of the image. The strontium-rich area inside of the crystal
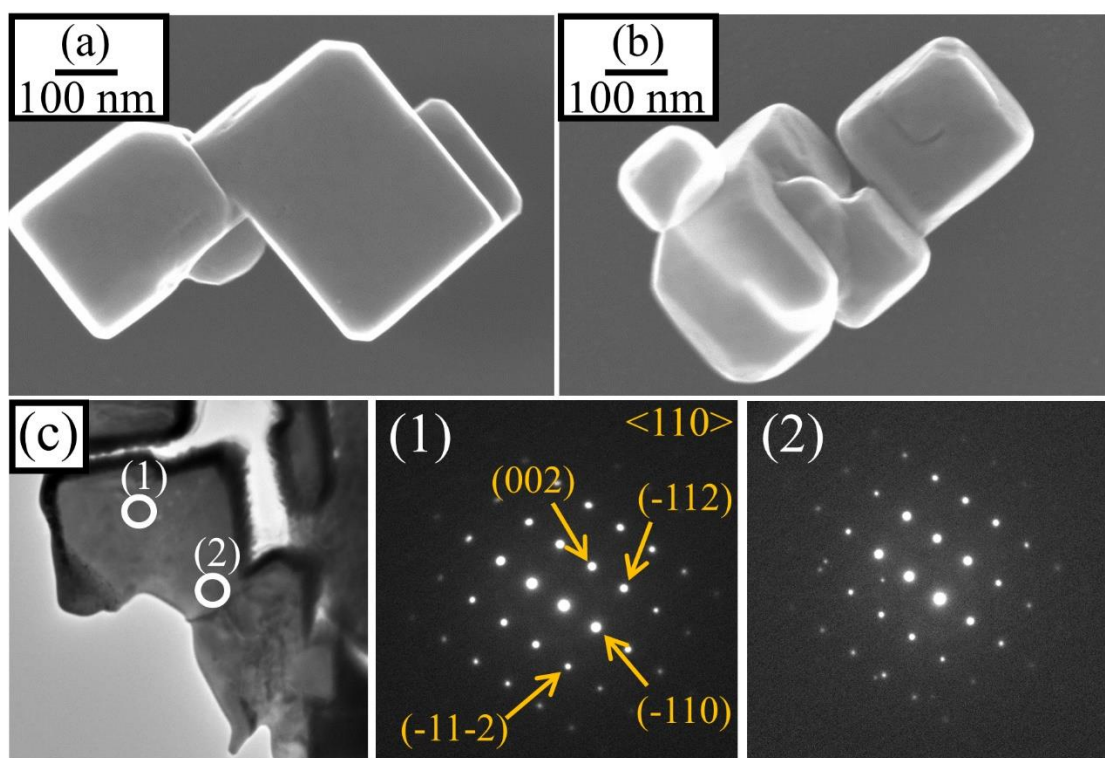
Fig. 4-19. (a and b) STEM, **(c)** TEM, and **(1 and 2)** electron diffraction images of $Sr_{1-x}Ba_xTaO_2N$ particles prepared by heating at 900 °C for 30 h with 30 wt% of $BaCN_2$. Images **(1)** and **(2)** were obtained from the regions indicated in **(c)**.
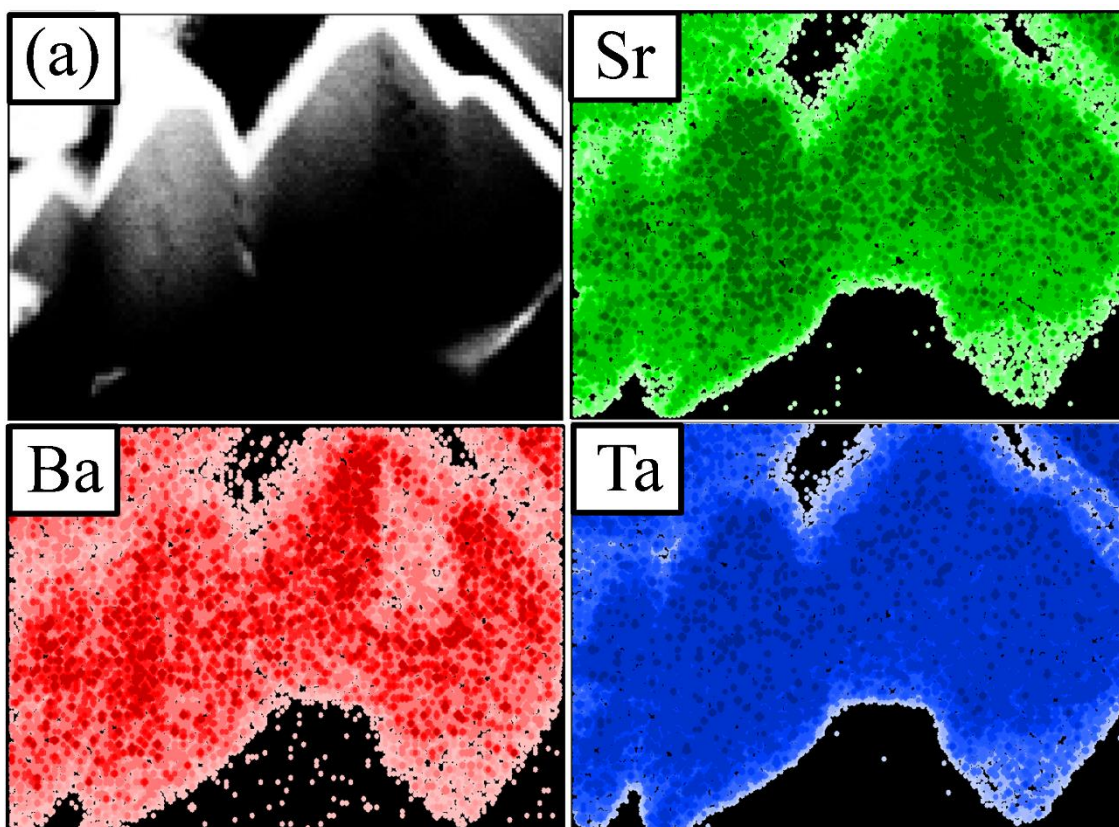
Fig. 4-20. (a) TEM and **(remainder)** EDX mapping images of oxynitride grains prepared by heating at 900 °C for 30 h with 30 wt% of BaCN$_2$.

contained a less amount of barium while exterior was barium-rich. This observation suggests that the reaction to form $Sr_{1-x}Ba_xTaO_2N$ occurred inhomogeneously from the outside to the inside of the grain. The slight asymmetry in the XRD peaks in **Fig. 4-16** supports this inhomogeneity. It is believed that the exteriors of the $SrTaO_2N$ grains dissolved to the $BaCN_2$ melt, after which the barium-rich oxynitride perovskite recrystallized around the residual $SrTaO_2N$ cores. The diffusion of Ba^{2+} ions may also have contributed to an exchange with Sr^{2+} ions in the perovskite crystal lattice during the heating at approximately 900 °C.

4-4. Conclusion

In conclusion, t-$BaCN_2$ melts at 910 °C, which is slightly below its theoretically estimated decomposition temperature of 912 °C in DFT calculation. It will be a promising flux for the crystal growth and sintering of nitrides and oxynitrides. Melts of other alkaline-earth metal carbodiimides were not stable and they decompose to the mixtures of their metals, carbides, and nitrogen at high temperature.

The molten $BaCN_2$ was found to be useful as a flux and the electrically insulating $Sr_{1-x}Ba_xTaO_2N$ ceramics were obtained. These materials maintained their stoichiometric nitrogen contents. The molten $BaCN_2$ partially dissolved $SrTaO_2N$ and

formed the solid solution precipitant $Sr_{1-x}Ba_xTaO_2N$ from the melt upon cooling. Cubic

$Sr_{1-x}Ba_xTaO_2N$ crystals were reddish orange in color. The compositional gradient in a

single crystal suggests that the crystals grew from the melt in nonequilibrium condition

in nitrogen flow. Hereafter, $BaTaO_2N$ was selected as a target material to obtain

homogeneous crystals using a $BaCN_2$ flux.

Chapter 4 References

[1] D. Chen, D. Habu, Y. Masusbuchi, S. Torii, T. Kamiyama, S. Kikkawa, "Partial nitrogen loss in $SrTaO_2N$ and $LaTiO_2N$ oxynitride perovskites", *Solid State Sci.*, 2016, 54, 2–6.

[2] A. Hosono, Y. Masubuchi, S. Kikkawa, "Sintering behavior of dielectric $SrTaO_2N$ under high pressure of nitrogen", *Ceram. Int.*, 2017, 43, 2737–2742.

[3] I. Burn, "Flux-sintered $BaTiO_3$ dielectrics", *J. Mater. Sci.*, 1982, 17, 1398–1408.

[4] G. K. Layden, "Polymorphism of $BaTa_2O_6$", *Mat. Res. Bull.*, 1967, 2, 533–539.

[5] R. J. Gambino, F. Leonhard, "Growth of barium ferrite single crystals", *J. Am. Ceram. Soc.*, 1961, 44, 221–224.

[6] Y. Mizuno, H. Wagata, K. Yubuta, N. Zettsu, S. Oishi, K. Teshima, "Flux growth of $Sr_2Ta_2O_7$ crystals and subsequent nitridation to form $SrTaO_2N$ crystals", *CrystEngComm*, 2013, 15, 8133–8138.

[7] T. Sugai, S. Hasegawa, G. Ohara, "Growth of strontium titanate single crystals from molten salts", *Jpn. J. Appl. Phys.*, 1968, 7, 358–362.

[8] H. Yamane, M. Shimada, S. J. Clarke, F. J. DiSalvo, "Preparation of GaN single crystals using a Na flux", *Chem. Mater.*, 1997, 9, 413–416.

[9] H. Yamane, F. J. DiSalvo, "Sodium flux synthesis of nitrides", *Prog. Solid State Chem.*, 2017, 51, 27–40.

[10] N. Arumugam, A. Honnerscheid, M. Jansen, "A new oxynitride compound of molybdenum, Na_3MoO_3N –synthesis via the azide route and structure", *Z. Anorg. Allg. Chem.*, 2003, 629, 939–941.

[11] M. Hojamberdiev, K. Yubuta, J. J. M. Vequizo, A. Yamanaka, S. Oishi, K. Domen,

K. Teshima, "NH$_3$-assisted flux growth of cube-like BaTaO$_2$N submicron crystals in a completely ionized nonaqueous high-temperature solution and their water splitting activity", *Cryst. Growth Des.*, 2015, 15, 4663–4671.

[12] M. Hojamberdiev, A. Yamaguchi, K. Yubuta, S. Oishi, K. Teshima, "Fabrication of La$_2$Ti$_2$O$_7$ Crystals Using an Alkali-Metal Molibdate Flux Growth Method and Their Nitridability To Form LaTiO$_2$N Crystals under a High-Temperature NH$_3$ atmosphere", *Inorg. Chem.*, 2015, 54, 3237–3244.

[13] N. Cordes, T. Bräuniger, W. Schnick, "Ammonothermal Synthesis of *EAM*O$_2$N (*EA* = Sr, Ba; *M* = Nb, Ta) Perovskites and [14]N Solid-State NMR Spectroscopic Investigations of *AM*(O,N)$_3$ (*A* = Ca, Sr, Ba, La)", *Eur. J. Inorg. Chem.*, 2018, 5019–5026.

[14] N. Cordes, W. Schnick, "Ammonothermal Synthesis of Crystalline Oxonitride Perovskites *Ln*TaON$_2$ (*Ln* = La, Ce, Pr, Nd, Sm, Gd)", *Chem. – Eur. J.*, 2017, 23, 11410–11415.

[15] C. Izawa, T. Kobayashi, K. Kishida, T. Watanabe, "Ammonothermal Synthesis and Photocatalytic Activity of Lower Valence Cation-Doped LaNbON$_2$", *Adv. Mat. Sci. Engin.*, 2014, 465720.

[16] H. Yamane, F. J. DiSalvo, "Synthesis and crystal structure of new oxynitride, Ba$_3$ZnN$_2$O", *J. Alloys Compd.*, 1996, 234, 203–206.

[17] T. Hashimoto, H. Yamane, "Ba$_4$GaN$_3$O", *Acta Cryst.*, 2014, E70, i28.

[18] P. M. Mallinson, Z. A. Gàl, S. J. Clarke, "Two New Structurally Related Strontium Gallium Nitrides: Sr$_4$GaN$_3$O and Sr$_4$GaN$_3$(CN$_2$)", *Inorg. Chem.*, 2006, 45, 419–423.

[19] M. Down, M. Haley, P. Hubberstey, J. Pulham, E. Thunder, "Solutions of lithium salts in liquid lithium: preparation and X-ray crystal structure of the dilithium salt of carbodi-imide (cyanamide)", *J. Chem. Soc. Dalton Trans.*, 1978, 10, 1407–1411.

[20] A. Harper, P. J. Hubberstey, "Alkali Metal Salts of Cyanamide: Synthesis and Characterization of Na(HNCN), Na$_4$H$_2$(NCN)$_3$, and Na$_2$(NCN)", *J. Chem. Res.*, 1989, 7, 194–195.

[21] M. Becker, M. Jansen, "Synthesis of potassium cyanamide, and crystal structure determination by pareto optimization of the cost functions 'lattice energy' and 'powder intensities'", *Solid State Sci.*, 2000, 2, 711–715.

[22] P. Guido, G. James, "Metal amide catalyzed amination of olefins", *Pure & Appl. Chem.*, 1985, 57, 1917–1926.

[23] U. Berger, W. Schnick, "Synthesis, crystal structures, and vibrational spectroscopic properties of MgCN$_2$, SrCN$_2$, and BaCN$_2$", *J. Alloys Compd.*, 1994, 206, 179–184.

[24] N. -G. Vannerberg, "The Crystal Structure of Calcium Cyanamide", *Acta Chem. Scand.*, 1962, 16, 2263–2266.

[25] R. Riedel, A. Greiner, G. Miehe, W. Dressler, H. Fuess, J. Bill, F. Aldinger, "The First Crystalline Solids in the Ternary Si-C-N System", *Angew. Chem. Int. Ed. Engl.*, 1997, 36, 603–606.

[26] S. K. Deb, A. D. Yoffe, "Inorganic cyanamides. Physical and optical properties, and decomposition", *Trans. Faraday Soc.*, 1959, 55, 106–113.

[27] M. Cooper, "The Structures of Some Inorganic Cyanamides. II. The Structure of Lead Cyanamide", *Acta Cryst.*, 1964, 17, 1452–1456.

[28] X. Tang, H. Xiang, X. Liu, M. Speldrich, R. Dronskowski, "A Ferromagnetic Carbodiimide: $Cr_2(NCN)_3$", *Angew. Chem. Int. Ed.*, 2010, 49, 4738–4742.

[29] X. Liu, M. Krott, P. Muller, C. Hu, H. Lueken, R. Dronskowski, "Synthesis, Crystal Structure, and Properties of MnNCN, the First Cabodiimide of a Magnetic Transition Metal", *Inorg. Chem.*, 2005, 44, 3001–3003.

[30] X. Liu, L. Stork, M. Speldrich, H. Lueken, R. Dronskowski, "FeNCN and $Fe(NCNH)_2$: Synthesis, Structure, and Magnetic Properties of a Nitrogen-Based Pseudo-Oxide and -Hydroxide of Divalent Iron", *Chem. – Eur. J.*, 2009, 15, 1558–1561.

[31] M. Krott, X. Liu, B. Fokwa, M. Speldrich, H. Lueken, R. Dronskowski, "Synthesis, Crystal-Structure Determination and Magnetic Properties of Two New Transition-Metal Carbodiimides: CoNCN and NiNCN", *Inorg. Chem.*, 2007, 46, 2204–2207.

[32] M. Krott, "Neue Carbodiimide der 3d-Übergangsmetalle", Shaker Verlag, Aachen (2009).

[33] M. Neukirch, S. Tragl, H. Meyer, "Syntheses and Structural Properties of Rare Earth Carbodiimides", *Inorg. Chem.*, 2006, 45, 8188–8193.

[34] G. Baldinozzi, B. Malinowska, M. Rakib, G. Durand, "Crystal structure and characterization of cadmium cyanamide", *J. Mater. Chem.*, 2002, 12, 268–272.

[35] O. Reckeweg, F. DiSalvo, "$EuCN_2$ — The First, but Not Quite Unexpected Ternary Rare Earth Metal Cyanamide", *Z. Anorg. Allg. Chem.*, 2003, 629, 177–179.

[36] A. Corkett, P. Konze, R. Dronskowski, "The Ternary Post-transition Metal Carbodiimide $SrZn(NCN)_2$", *Z. Anorg. Allg. Chem.*, 2017, 643, 1456–1461.

[37] M. Kubus, R. Heinicke, M. Ströbele, D. Enseling, T. Jüstel, H. -J. Meyer, "Synthesis of new structurally related cyanamide compounds $LiM(CN_2)_2$ where M is Al^{3+}, In^{3+} or Yb^{3+}", *Mat. Res. Bull.*, 2015, 62, 37–41.

[38] A. Perret, A. M. Krawezynski, "Recherches sur les cyanamides metalliques", *Helvetica Chimica Acta*, 1932, 15, 1009–1022.

[39] S. Nagai, G. Yamaguchi, "Studies on Synthesis of Calcium Cyanamide from Calcium Carbonate and Ammonia, I", *J. Soc. Chem. Ind. Japan*, 1940, 43, 219B.

[40] Y. Masubuchi, S. Nishitani, A. Hosono, Y. Kitagawa, J. Ueda, S. Tanabe, H. Yamane,

M. Higuchi, and S. Kikkawa, "Red-emission over a wide range of wavelength at various temperatures from tetragonal $BaCN_2:Eu^{2+}$", *J. Mater. Chem. C*, 2018, 6, 6370–6377.

[41] M. Krings, M. Wessel, W. Wilsmann, P. Müller, R. Dronskowski, "Temperature-dependent synthetic routes to and thermochemical ranking of *α*- and *β*- SrNCN", *Inorg. Chem.*, 2010, 49, 2267–2272.

[42] K. Momma, F. Izumi, "VESTA 3 for three-dimensional visualization of crystal, volumetric and morphology data", *J. Appl. Crystallogr.*, 2011, 44, 1272–1276.

[43] F. Izumi, K. Momma, "Three-Dimensional Visualization in Powder Diffraction", *Solid State Phenom.*, 2007, 130, 15–20.

[44] S. -K. Sun, Y. Masubuchi, T. Motohashi, S. Kikkawa, "Direct synthesis of nearly single-phase $BaTaO_2N$ and $CaTaO_2N$ powders", *J. Eur. Ceram. Soc.*, 2015, 35, 3289–3294.

[45] G. Kresse and J. Furthmüller, "Efficiency of *ab-initio* total energy calculations for metals and semiconductors using a plane-wave basis set", *Comput. Mater. Sci.*, 6, 15–50.

[46] J. P. Perdew, K. Burke and M. Ernzerhof, "Generalized Gradient Approximation Made Simple", *Phys. Rev. Lett.*, 1996, 77, 3865–3868.

[47] S. Grimme, J. Antony, S. Ehrlich, S. Krieg, "A consistent and accurate *ab initio* parametrization of density functional dispersion correction (DFT-D) for the 94 elements H-Pu", *J. Chem. Phys.*, 2010, 132, 154104/1–19.

[48] A. Togo, I. Tanaka, "First principles phonon calculations in materials science", *Scr. Mater.*, 2015, 108, 1–5.

[49] R. P. Stoffel, C. Wessel, M. -W. Lumey, R. Dronskowski, "Ab initio thermochemistry of solid-state materials", *Angew. Chem. Int. Ed.*, 49, 2010, 5242–5266.

[50] R. P. Stoffel, R. Dronskowski, "*Handbook of Solid State Chemistry*", Vol. 5, R. Dronskowski, S. Kikkawa, A. Stein (Eds.), Wiley-VCH, Weinheim, New York (2017).

[51] Y. Yamamoto, K. Kinoshita, K. Tamaru, T. Yamanaka, "Redetermination of the Crystal Structure of Calcium Cyanamide", *Bull. Chem. Soc. Jpn.*, 1958, 31, 501–502.

[52] J. D. Hanawalt, H. W. Rinn, L. K. Frevel, "Chemical Analysis by X-Ray Diffraction", *Anal. Chem.*, 1938, 10, 457–512.

[53] A. J. King, G. L. Clark, "The Crystal Structure of Barium", *J. Am. Chem. Soc.*, 1929, 51, 1709–1711.

[54] J. Howe, C. Rawn, L. Jones, H. Ow, "Improved crystallographic data for graphite", *Powder Diffr.*, 2003, 18, 150–154.

[55] J. Donohue, "A refinement of the positional parameter in *α*-nitrogen", *Acta Crystallogr.*, 1961, 14, 1000–1001.

[56] M. Knapp, U. Ruschewitz, "Structural Phase Transitions in CaC_2", *Chem. Eur. J.*,

2001, 7, 874–880.

[57] V. Vohn, M. Knapp, U. Ruschewitz, "Synthesis and Crystal Structure of SrC_2", *J. Solid State Chem.*, 2000, 151, 111–116.

[58] V. Vohn, W. Kockelmann, U. Ruschewitz, "On the synthesis and crystal structure of BaC_2", *J. Alloys Compds.*, 1999, 284, 132–137.

[59] S. -K. Sun, Y. -R. Zhang, Y. Masubuchi, T. Motohashi, S. Kikkawa, "Additive sintering, postannealing, and dielectric properties of $SrTaO_2N$", *J. Am. Ceram. Soc.*, 2014, 97, 1023–1027.

[60] H. Yamane, S. Kikkawa, M. Koizumi, "High- and Low-Temperature Phases of Lithium Boron Nitride, Li_3BN_2: Preparation, Phase Relation, Crystal Structure, and Ionic Conductivity", *J. Solid State Chem.*, 1987, 71, 1–11.

[61] "*CRC Handbook of Chemistry and Physics 97th Edition*", W. M. Haynes (Ed.), CRC Press, Florida (2016).

[62] H. Krase, Y. Yee, "The mechanism and thermochemistry of the reaction between calcium carbide and nitrogen", *J. Am. Chem. Soc.*, 1924, 46, 1358–1366.

[63] M. Gilleßen, M. Lumeij, J. George, R. P. Stoffel, T. Motohashi, S. Kikkawa, R. Dronskowski, "Oxygen-storage materials $BaYMn_2O_{5+\delta}$ from the quantum-chemical point of view", *Chem. Mater.*, 2012, 24, 1910–1916.

[64] "*Shriver & Atkins Inorganic Chemistry*", P. Atkins, T. Overton, J. Rourke, M. Weller, F. Armstrong (Eds.), Oxford University Press, United Kingdom (2005).

Chapter 5

Preparation of BaTaO$_2$N Microcrystals Using a BaCN$_2$ Flux

5-1. Introduction

Perovskite-type BaTaO$_2$N has been expected to show relaxor-like ferroelectricity. [1,2] Highly-insulating single crystals are necessary to study its intrinsic electrical properties. The flux growth method is considered to be suitable for obtaining crystals of such thermally unstable materials. The use of molten BaCN$_2$ at approximately 900 °C for the preparation of Sr$_{1-x}$Ba$_x$TaO$_2$N (x = 0.04 – 0.23) microcrystals was mentioned in the last chapter. The crystal products were inhomogeneous and there was a compositional gradient from Sr-rich interior to Ba-rich exterior in the grains. Selecting BaTaO$_2$N as a target material will be more sensible strategy to obtain homogeneous oxynitride crystals. In the present chapter, crystals of perovskite-type BaTaO$_2$N were grown with molten BaCN$_2$ and the crystal growth mechanism is discussed through the microstructural analysis of the product using TEM.

5-2. Experimental

Sample preparation

Reddish BaTaO$_2$N powder with particle size of approximately 0.1 μm was

synthesized by heating a powder mixture of $BaCO_3$ and Ta_2O_5 as mentioned in **Chapter 2**. White tetragonal $BaCN_2$ (t-$BaCN_2$) powder was prepared by ammonolysis of $BaCO_3$ powder (FUJIFILM Wako Pure Chemical, 99.9%) at 900 °C for 10 h. [3]

The $BaTaO_2N$ powder was mixed with $BaCN_2$ of 17 – 67 mol% ratios in an agate mortar in a glove box filled with a dry nitrogen to avoid the oxidation and hydrolysis of $BaCN_2$ by the reaction with air. The powder mixture in an alumina crucible was enclosed in a hand-made tantalum container with a thickness of approximately 0.1 mm (Nilaco, > 99%) in a nitrogen atmosphere to suppress the loss of $BaCN_2$ flux due to its partial decomposition or vaporization above 910 °C. The tantalum container was then heated to 910 °C at a rate of 300 °C/h and then held for 30 min in an alumina tube furnace. The sample was slowly cooled to 880 °C at a rate of 1.8 °C/h. The effect of the cooling rate was studied by changing it to 300 °C/h in an additional experiment. The duration time at 910 °C was changed to 24 h to investigate the effect of flux loss above the melting point of $BaCN_2$. The sample was cooled down at a rate of 1.8 °C/h in this trial. The products were either reddish powder or solidified lumps, depending on the amount of t-$BaCN_2$ in the starting mixture. The products were washed with 1 M nitric acid and distilled water to remove the soluble residue, which was mainly excess $BaCN_2$. Reddish powder was obtained after filtration using filter paper with a pore size of less than 50 μm

(Toyo Roshi K. K.). The sample preparation conditions, the product appearance after being taken out from the furnace, and the particle sizes of the washed products are summarized in **Table 5-1**.

The crystalline phases of the samples were identified using powder X-ray diffraction (XRD; Ultima IV, Rigaku) with Cu Kα radiation over the 2θ range of 10 to 90° with a step size of 0.02° and a scanning rate of 10°/min. Electron probe microanalysis (EPMA; JXA-8530F, JEOL) was conducted to analyze the elemental contents in the final washed product with grain size larger than 2 μm. The average molar ratio was Ba:Ta:O:N = 23.0:22.1:37.0:17.9, which roughly corresponds to a ratio of 1:1:2:1, i.e., the crystal products are $BaTaO_2N$. The residual carbon contents in the $BaTaO_2N$ crystal products were less than the detection limit (< 0.3 wt%) of combustion CHN analysis (CE440, Exeter Analytical Inc.).

Microstructure observation

Thin slice of the $BaTaO_2N$ crystals embedded in the solidified $BaCN_2$ less than 100 nm in thickness was prepared with a focused ion beam (FIB) of gallium ion (SMI 3050SE, Hitachi High-Technologies). Transmission electron microscope (TEM, Titan3 G2 60-300, FEI Company) with Cs-spherical aberration corrector was employed for microstructure observation of the crystals. Energy dispersive X-ray spectroscopy (EDX)

analysis was also performed to investigate the fluctuation in the molar ratio of Ba and Ta in the crystals. Furthermore, high angle annular dark-field scanning TEM (HAADF-STEM) images were acquired using the same TEM machine. The $BaTaO_2N$ particle sizes and their surfaces were analyzed using a scanning electron microscope (SEM; JSM-6390 LVS, JEOL). The shapes of relatively large $BaTaO_2N$ crystals were observed with an optical microscope (VHX-2000, KEYENCE).

5-3. Results and discussion

Sample preparation

Some grain growth was observed on the reddish products for all preparation conditions, as summarized in **Table 5-1**. **Fig. 5-1** shows powder XRD patterns for the grown product prepared with 67 mol% of $BaCN_2$. Secondary phases were most easily observed with XRD among the products prepared with various amounts of t-$BaCN_2$. Perovskite-type $BaTaO_2N$ was the main phase in the annealed sample (**Fig. 5-1(a)**), which was contaminated with a trace amount of Ba-rich Ruddlesden-Popper (RP) type layered perovskite Ba_2TaO_3N and an unidentified impurity. Ba_2TaO_3N may have been formed by the reaction of $BaTaO_2N$ perovskite with an excess Ba in the $BaCN_2$ flux. Oxygen was supplied from surface adsorbates both on $BaTaO_2N$ and $BaCN_2$. The excess Ba was

supplied as BaO to the BaTaO$_2$N perovskite, which formed Ba$_2$TaO$_3$N. Ba$_2$TaO$_3$N has

been reported to easily decompose and react with oxygen and humidity in the air. [4] The

Ba$_2$TaO$_3$N impurity thus disappeared and formed another impurity of BaCO$_3$ during the

reaction with air for 1 h (**Fig. 5-1(b)**). The crystallinity of BaTaO$_2$N was significantly

improved after a leaching procedure of the as-grown product in nitric acid (**Fig. 5-1(c)**).

The full width at half maximum (FWHM) of the (321) diffraction peak for BaTaO$_2$N was

significantly reduced from 0.31° to 0.22° by the leaching process. The leached product

was highly crystalline BaTaO$_2$N without any impurities. The lattice parameter (a =

0.4111(1) nm) of BaTaO$_2$N was consistent with the literature value (a = 0.41128 nm). [5]

These results suggest some structural defects in the perovskite were removed by the nitric

acid treatment, which resulted in the formation of highly-crystalline BaTaO$_2$N. Generally,

oxynitride perovskites are stable to nitric acid, but Ruddlesden-Popper phases (e.g.

Sr$_2$TaO$_3$N and Ba$_2$TaO$_3$N) containing rock-salt layers like SrO and BaO are decomposed

by acid and humidity.

TEM observation

The microstructure of the product prepared with 67 mol% of BaCN$_2$ before

nitric acid leaching was assessed. Square-shaped grains surrounded by a solidified BaCN$_2$

flux are apparent in the TEM bright field image of a thin slice of the as-grown product,

as shown in **Fig. 5-2(a)**. A selected area electron diffraction (SAED) pattern was obtained

from the region indicated in this figure, and the presence of cubic $BaTaO_2N$ was

confirmed by applying an incident electron beam along the <110> direction, as shown in

Fig. 5-2(b). No additional diffraction spots were observed. The lattice parameter was $a =$

0.415(3) nm, which was in good agreement with that of the acid-washed powder sample

shown in **Fig. 5-1(c)** (a = 0.4111(1) nm) within experimental error. A high-magnification

HAADF-STEM image (**Fig. 5-2(c)**) shows cation ordering in a portion of the encircled

area in **Fig. 5-2(a)**. Ba and Ta atoms can be distinguished in this image because their

brightness levels are different depending on atomic numbers. This phenomenon is known

as Z-contrast. Specifically, the Ta atoms appear to be slightly brighter than the Ba atoms.

The atomic arrangement in **Fig. 5-2(c)** is consistent with a cubic perovskite-type structure

observed from the <110> direction.

The crystalline lattice was not well developed in the areas around the grain

edges. The encircled area in **Fig. 5-3(a)** is observed along the <111> zone axis. The

atomic arrangement of $BaTaO_2N$ along this direction is clearly observed for the area

labeled **1** at the bottom right of the higher-magnification image in **Fig. 5-3(b)**. However,

it is not clearly observed in the areas labeled **2 – 4**, which have different atomic

arrangements over ranges of approximately 3 – 10 nm. Fourier transformations of these

Table 5-1. Crystal growth conditions, appearance of the products, and maximum grain sizes of BaTaO$_2$N crystals.

Product name	BaCN$_2$ amount / mol%	Duration time at 910 °C / h	Cooling rate / °C h^{-1}	Appearance after cooling	Maximum grain size / μm
As-prepared(a)	-	-	-	Reddish powder	0.15
(b)	17	0.5	1.8	Reddish powder	0.2
(c)	22	0.5	1.8	Reddish powder	0.7
(d)	36	0.5	1.8	Reddish powder	2.2
(e)	46	0.5	1.8	Reddish solid	3.1
(f)	67	0.5	1.8	Reddish solid	0.9
(g)	46	0.5	300	Reddish solid	0.5
(h)	46	24	1.8	Reddish solid	0.4
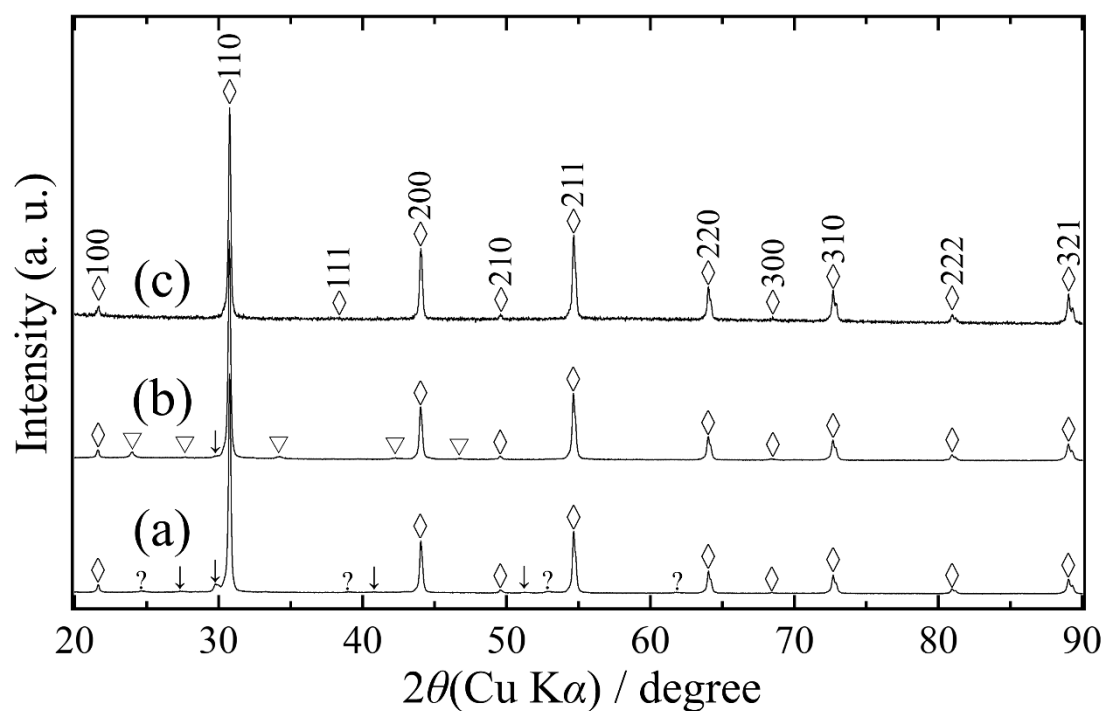
Fig. 5-1. Powder XRD patterns for BaTaO$_2$N grown with 67 mol% of BaCN$_2$. **(a)** As-grown product, **(b)** that after exposure to air for 1 h, and **(c)** that after leaching in nitric acid and water. Diamonds, arrows, inverse triangles, and question marks indicate diffraction peaks for BaTaO$_2$N (ICSD 202763), Ba$_2$TaO$_3$N (JCPDS 47-1388), BaCO$_3$ (PDF 01-071-2394), and an unknown phase, respectively.

images were performed using the Digital Micrograph software package (Gatan) for the areas **1** – **4** in **Fig. 5-3(b)**. The (01-1) lattice spacing was estimated from the lattice fringes indicated by the yellow arrows in the same figure. The average spacing in area **1** was 0.293 nm, which was consistent with the literature value of 0.291 nm. [5] The average spacing estimated for area **3** was 0.316 nm, which is slightly larger than that for area **1**. For area **4**, the crystal orientation could not be identified from the Fourier transform image. The average lattice spacing in area **4** was approximately 0.333 nm, which is larger than that for area **1**. One possible explanation is that the fringes in area **4** correspond to (004) plane of RP-type Ba_2TaO_3N with space group $I4/mmm$ together with $a = 0.411508(3)$ nm and $c = 1.33778(1)$ nm. The $c/4$ value was calculated to be 0.334 nm (JCPDS 47-1388). The area out of $BaTaO_2N$ crystals therefore consists primarily of a solidified $BaCN_2$ flux and $BaTaO_2N$ containing a large amount of BaO in the form of stacking defects, similar to the results obtained in the work with $SrTaO_2N$-Sr_2TaO_3N system. [6]

The chemical compositions of these areas were investigated using EDX. Measurement at each point was conducted for a short duration of 10 s to avoid sample drift. The Ba/Ta molar ratios are plotted in **Fig. 5-4(b)**. The ratio was normalized for positions **2** – **4** against the value for the $BaTaO_2N$ single crystal at position **1** in **Fig. 5-4(a)**. A much greater amount of Ba was detected at the edge positions **2** – **4** than at the
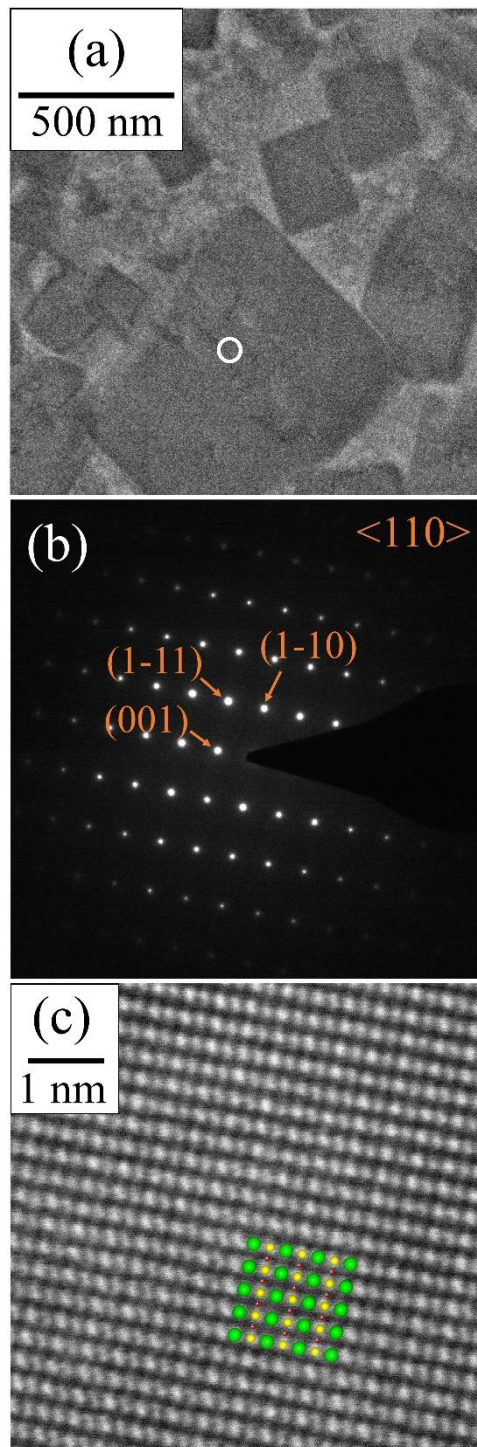
Fig. 5-2. (a) TEM bright-field image of a thin specimen. **(b)** SAED image of the encircled area in **(a)**. **(c)** High-magnification HAADF-STEM image of the area encircled in **(a)**. Green, yellow, and red circles in **(c)** indicate Ba, Ta, and O/N anions, respectively. The crystal structure model was drawn by the crystallographic imaging software VESTA. [7]
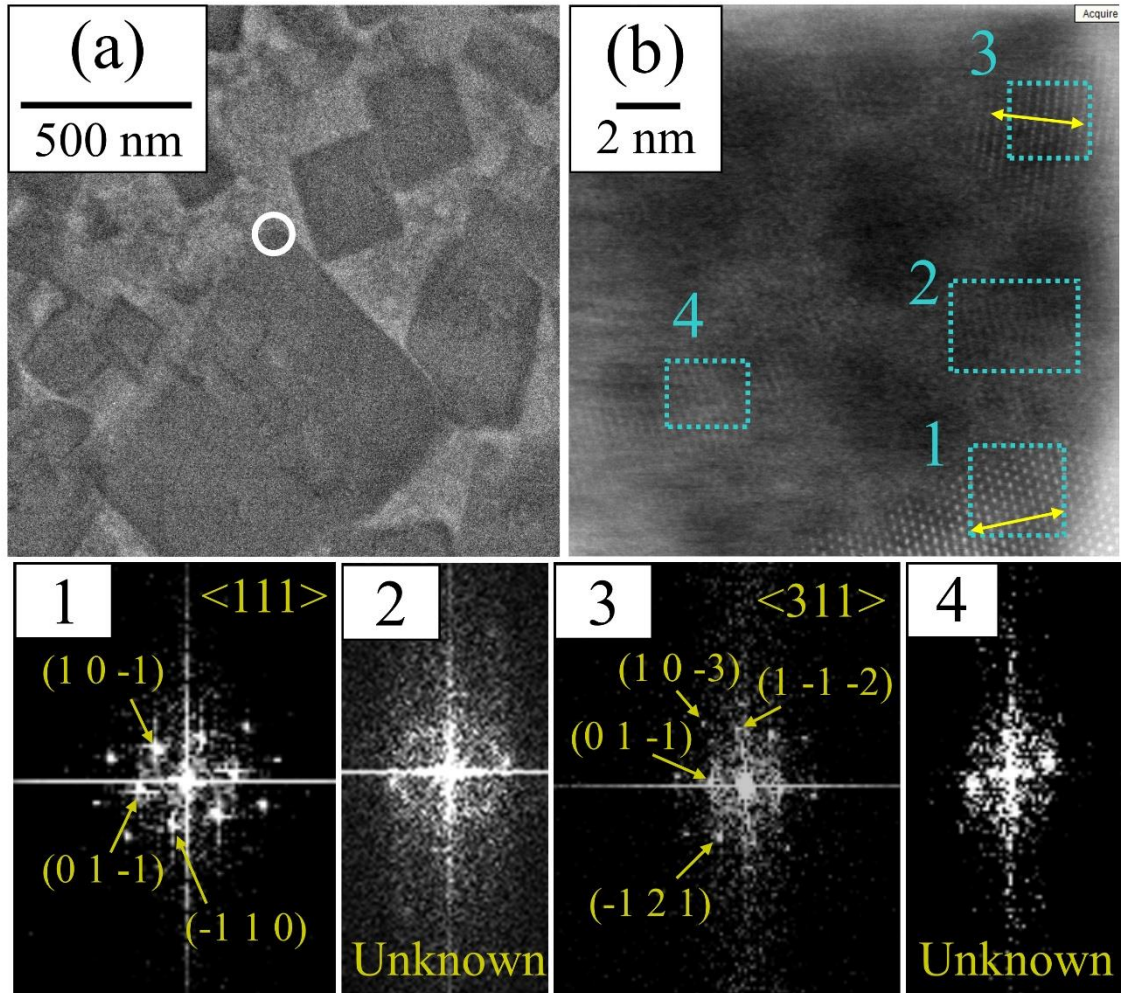
Fig. 5-3. (a) TEM blight-field image of BaTaO$_2$N crystals in the solidified BaCN$_2$ specimen. **(b)** HAADF-STEM image of the area encircled in **(a)**. **(1)** – **(4)** Fourier transformation images generated from the respective areas in **(b)**.

highly-crystalline position **1**. Ba-rich phases such as RP type Ba_2TaO_3N identified in powder XRD (**Fig. 5-1(a)**) are contained at the positions **2 – 4**.

Ba₂TaO₃N was generated as a thin skin layer around the BaTaO₂N perovskite crystals recrystallized from the $BaCN_2$ melt. The Ba-rich phase layers such as BaO were randomly inserted between the BaTaO₂N perovskite layers, stacking around the edges of the perovskite crystals. These phenomena explain why the crystallinity of the as-grown BaTaO₂N was slightly low and why a trace amount of Ba_2TaO_3N was evident in the powder XRD pattern in **Fig. 5-1(a)**. These data suggest that the starting BaTaO₂N powder was dissolved in molten $BaCN_2$, followed by recrystallization of BaTaO₂N single crystals with a uniformed perovskite-type atomic arrangement and precipitation of solid phases including Ruddlesden-Popper type Ba_2TaO_3N, which partially contain an insertion of BaO layers. The formation mechanism of Ba-rich oxynitrides such as Ba_2TaO_3N can be surmised in several routes. (1) they were formed as metastable phases at the beginning of the recrystallization from the flux. These phases were generated at the interfaces between solid BaTaO₂N and molten $BaCN_2$ during the growth of BaTaO₂N crystals at high temperatures. That is, crystals of BaTaO₂N did not directly recrystallize from the solute of this compound in the $BaCN_2$ flux. (2) BaTaO₂N simply recrystallized from the $BaCN_2$ solvent, and then Ba-rich phases were formed by decomposition of $BaCN_2$ during heating.

151

Growth of the BaTaO$_2$N perovskite crystals

The primary particles in as-prepared BaTaO$_2$N powder after ammonolysis were rounded form and 40 – 150 nm in size. They formed irregular aggregates approximately 2 – 3 μm in size, as depicted in **Fig. 5-5(a)**. The shape and size of the aggregates changed with increases in the amount of BaCN$_2$ in the flux during heating at 910 °C for 30 min. A slight grain growth occurred in the cases of precipitation of BaTaO$_2$N from the 17 mol% BaCN$_2$ flux (**Fig. 5-5(b)**). Cubic crystals reflecting the euhedral form of the perovskite-type structure appeared at 22 mol% as shown in **Fig. 5-5(c)**. These powder products with small amount of BaCN$_2$ ($\leq$ 22 mol%) are composed of submicron-sized tiny particles due to a lack of flux enough to grow BaTaO$_2$N crystallites. Larger red crystals were observed when 46 mol% BaCN$_2$ was used, and the particle size increased to 3.1 μm at 46 mol% BaCN$_2$, as can be seen in **Fig. 5-5(e)**. Micron-sized BaTaO$_2$N crystals were grown only in the cases in which the exterior region of the original BaTaO$_2$N particles were dissolved in the BaCN$_2$ flux and the interior of the BaTaO$_2$N particles are remained as the nucleus for crystal growth. In the samples containing micron-sized BaTaO$_2$N crystals (**Figs. 5-5(d)** and **(e)**), large crystals several microns in size coexisting with many submicron particles were observed. Slow precipitation from a dilute BaTaO$_2$N solution in the BaCN$_2$ flux was expected to increase the crystal size. Reddish color, which is the characteristic

of stoichiometric $BaTaO_2N$ [8,9], was confirmed by optical microscope observation of large grains (**Fig. 5-5(e)-2**). Rather, aggregates of small cubic crystals were present when high $BaCN_2$ concentrations (≥ 67 mol%) were used, as depicted in **Fig. 5-5(f)**. The original $BaTaO_2N$ powder was completely dissolved in a large amount of molten $BaCN_2$ at high temperatures, and tiny particles recrystallized by homogeneous nucleation.

In one trial, the cooling rate was increased from 1.8 to 300 °C/h using 46 mol% $BaCN_2$. Under these conditions, the crystal size was found to decrease to less than 0.5 μm, as shown in **Fig. 5-5(g)**. This suggests that slow cooling is required to obtain larger $BaTaO_2N$ crystals from a $BaCN_2$ flux. The effect of the hold duration at 910 °C was also investigated by changing the hold time from 30 min to 24 h using the 46 mol% $BaCN_2$. The maximum particle size from this trial was only 0.4 μm, as is evident in **Fig. 5-5(h)**. The formation of much smaller crystals compared to those obtained after 30 min (**Fig. 5-5(e)**) is attributed to a partial loss of the molten $BaCN_2$ flux by evaporation and decomposition during the heating process. Heating the reaction system to the melting point of tetragonal $BaCN_2$ (910 °C) is necessary to dissolve $BaTaO_2N$ powder, but the duration at 910 °C should be as short as possible because $BaCN_2$ flux is lost above 910 °C, which results in a condensation of the solution to form only tiny crystallites. Therefore, it is important to maintain a sufficient amount of the $BaCN_2$ melt during crystal growth,
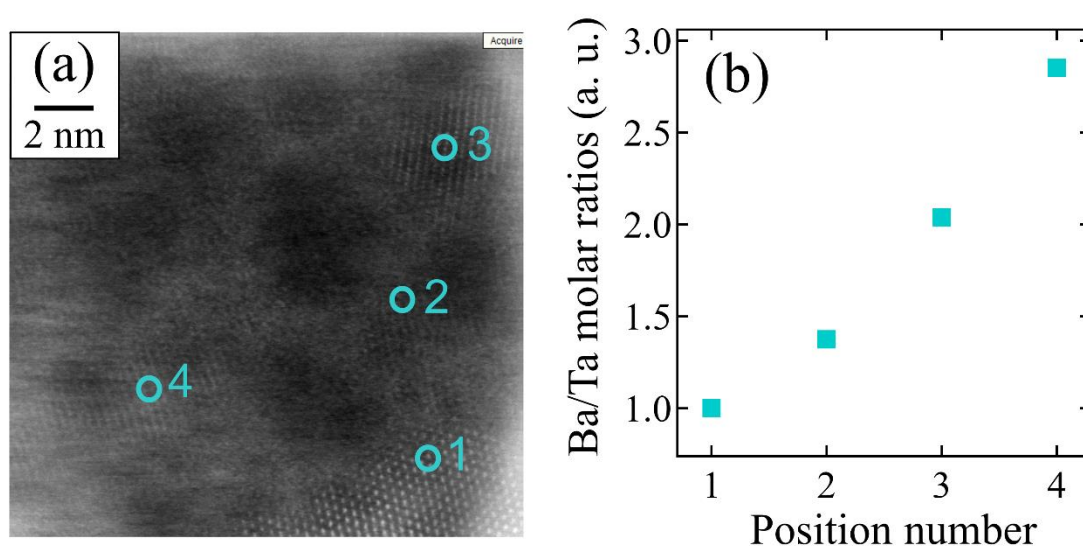
Fig. 5-4. (a) HAADF-STEM image of the same area as in **Fig. 5-3(b)**. **(b)** Ba/Ta molar ratio plots at the respective points in **(a)**. Each value was determined by EDX quantification. Ba/Ta ratios of positions **2 – 4** were normalized with respect to that for position **1** (BaTaO$_2$N single crystal).
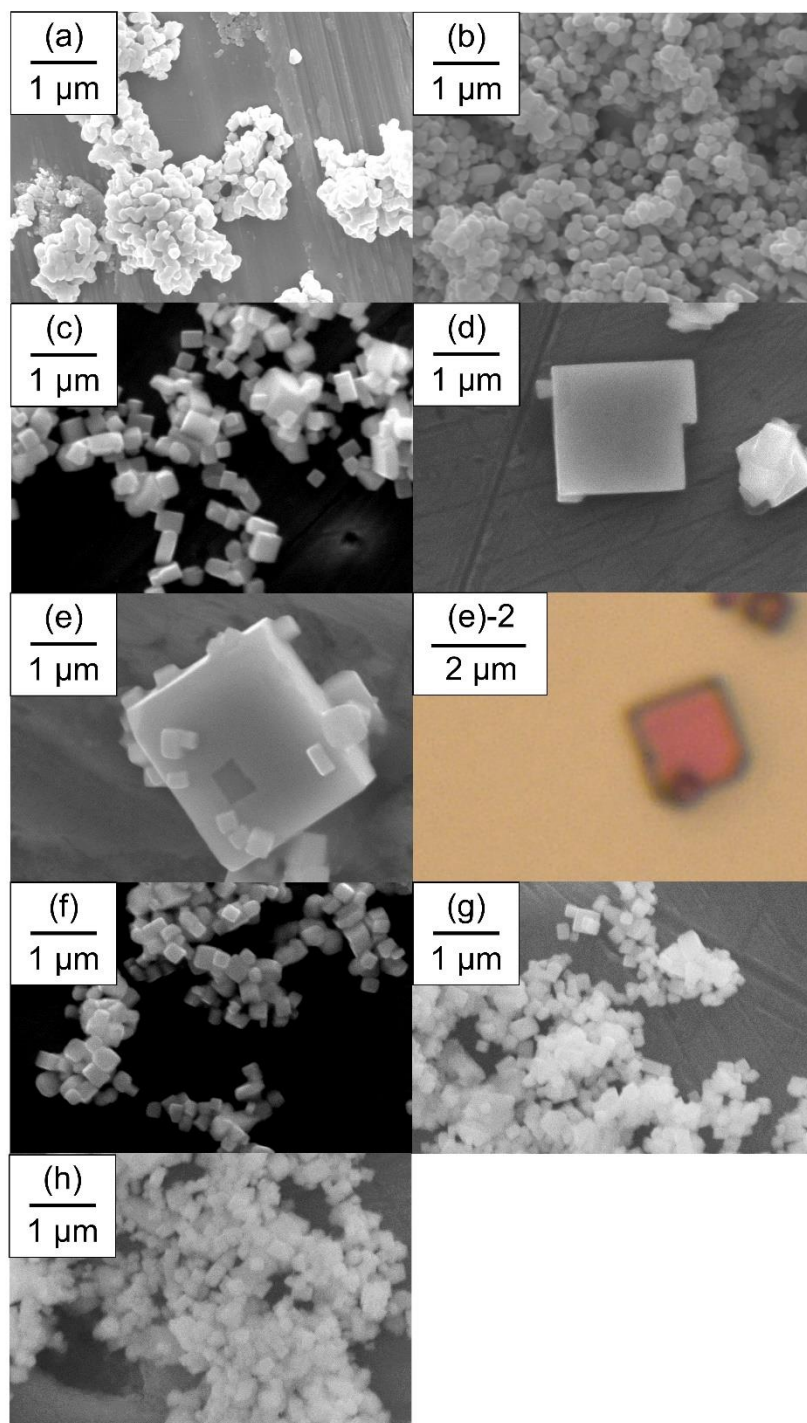
Fig. 5-5. SEM micrographs of BaTaO$_2$N particles: **(a)** As-prepared ammonolysis product; **(b)** – **(f)** products generated in the flux at 910 °C for 30 min with 17, 22, 36, 46, and 67 mol% BaCN$_2$, respectively, after cooling at 1.8 °C/h and acid/water washing, and similar products obtained using 46 mol% BaCN$_2$ at 910 °C **(g)** for 30 min with cooling at 300 °C/h and **(h)** for 24 h at the rate of 1.8 °C/h. [**(e)-2**] Optical micrograph of the product **(e)**.

even though this is difficult in practice.

5-4. Conclusion

Cubic crystals of perovskite-type BaTaO$_2$N were grown to approximately 3.1

μm in size in molten BaCN$_2$. Micron-size is enough to investigate the piezoelectricity

using piezoresponse force microscopy (PFM). TEM observations of BaTaO$_2$N crystals in

solidified BaCN$_2$ suggested that crystals were grown through several nanometer-sized

crystalline areas with a slightly larger lattice spacing than BaTaO$_2$N, such as RP phases

like Ba$_2$TaO$_3$N. Further growth would be possible by maintaining the BaCN$_2$ melt.

Growing furtherly larger BaTaO$_2$N crystals is expected to help clarify their intrinsic

properties by allowing dielectric measurements.

Chapter 5 References

[1] R. L. Withers, Y. Liu, P. M. Woodward, Y. I. Kim, "Structurally frustrated polar nanoregions in BaTaO$_2$N and the relationship between its high dielectric permittivity and that of BaTiO$_3$", *App. Phys. Lett.*, 2008, 92, 102907.
[2] Y. Hinuma, H. Moriwake, Y. Zhang, T. Motohashi, S. Kikkawa, I. Tanaka, "First principles study on relaxor-type ferroelectric behavior without chemical inhomogeneity in BaTaO$_2$N and SrTaO$_2$N", *Chem. Mater.*, 2012, 24, 4343–4349.
[3] Y. Masubuchi, S. Nishitani, A. Hosono, Y. Kitagawa, J. Ueda, S. Tanabe, H. Yamane, M. Higuchi, and S. Kikkawa, "Red-emission over a wide range of wavelength at various temperatures from tetragonal BaCN$_2$:Eu^{2+}", *J. Mater. Chem. C*, 2018, 6, 6370–6377.
[4] S. J. Clarke, K. A. Hardstone, C. W. Michie, M. J. Rosseinski, "High-temperature

synthesis and structures of perovskite and n=1 Ruddlesden-Popper tantalum oxynitrides", *Chem. Mater.*, 2002, 14, 2664–2669.

[5] F. Pors, R. Marchand, Y. Laurent, "Structural study of $BaTaO_2N$ and $BaNbO_2N$ oxynitrided perovskites", *Mat. Res. Bull.*, 1988, 23, 1447–1450.

[6] Y. Suemoto, Y. Masubuchi, Y. Nagamine, A. Matsutani, T. Shibahara, K. Yamazaki, S. Kikkawa, "Intergrowth between the Oxynitride Perovskite $SrTaO_2N$ and the Ruddlesden-Popper Phase Sr_2TaO_3N", *Inorg. Chem.*, 2018, 57, 9086–9095.

[7] K. Momma, F. Izumi, "VESTA 3 for three-dimensional visualization of crystal, volumetric and morphology data", *J. Appl. Crystallogr.*, 2011, 44, 1272–1276.

[8] M. Jansen, H. P. Letschert, "Inorganic yellow-red pigments without toxic metals", *Nature*, 2000, 404, 980–982.

[9] R. Aguiar, D. Logvinovich, A. Weidenkaff, A. Rachel, A. Reller, S. G. Ebbinghaus, "The vast colour spectrum of ternary metal oxyniride pigments", *Dyes Pigment.*, 2008, 76, 70–75.

Chapter 6

Ferroelectric Piezoresponse of BaTaO$_2$N Microcrystals

6-1. Introduction

In the last chapter, BaTaO$_2$N crystals in several micrometer size were grown in a BaCN$_2$ melt and further knowledge about their dielectricity is expected to be provided from the evaluation of these crystals. In the last decade, some atomic force microscopy (AFM)-based electrical property measurement techniques suitable for the samples in nano and micron-size have been developed. This method called piezoresponse force microscopy (PFM) is useful for the investigation on the piezoelectricity in small dielectric samples through the displacement of AFM cantilever. In the measurements, the contact of the electrical power source to the sample is achieved by placing a conductive cantilever on the sample surface. [1-3] A schematic image of a measurement setup is depicted in **Fig. 6-1(a)**.

PFM technique has been employed for some measurements of oxynitride perovskite materials. Piezoresponses were studied on the thin ceramic surfaces of SrTaO$_2$N and BaTaO$_2$N in thicknesses of less than 10 μm scratched off from their bulks in the applied voltage range of ±10 V. Clear piezoresponse images were obtained over the range of ±3 to 4 V for SrTaO$_2$N [4] and ±7 V for BaTaO$_2$N as mentioned in
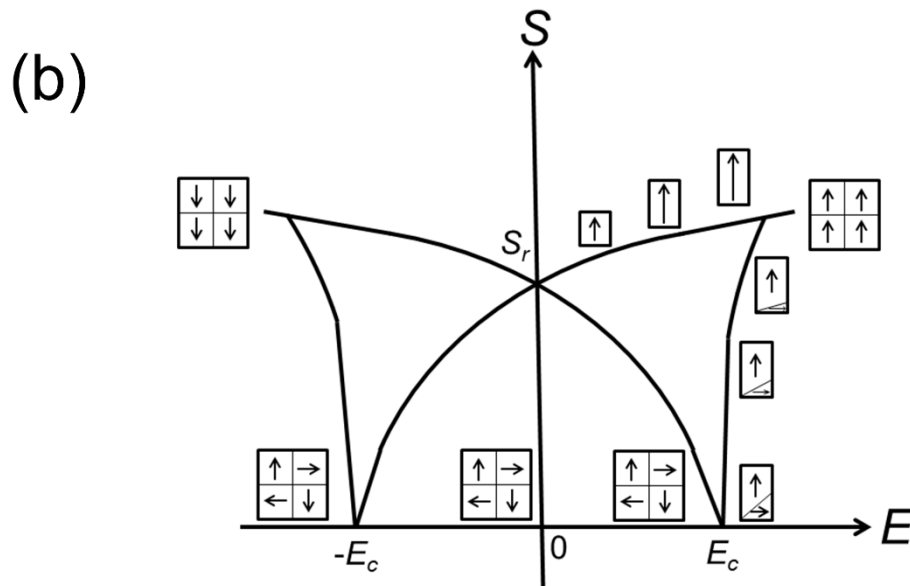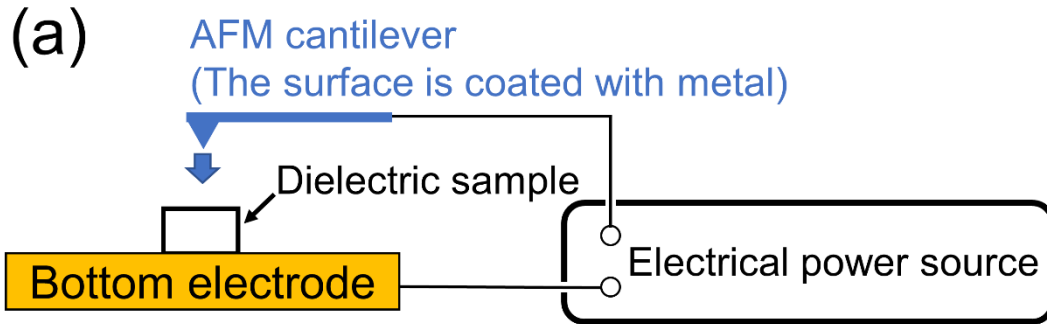
Fig. 6-1. (a) A schematic image of PFM device system and **(b)** PFM signal graph of ferroelectrics with a complete polarization phase switching drawn with sample stretching (S) and electrical field bias (E). Where E_c and S_r are coercive field and remnant strain, respectively.

Chapter 3. Local hysteresis polarization (P)-electrical field (E) loops were also acquired from a thin specimen of SrTaO$_2$N ceramic using a micron-sized Pt-deposited electrode over the applied voltage range of ±12 V. [4] The signal intensity was found to increase with increasing voltage and showed a maximum in the range of approximately ±8 V. However, its polarization could not be saturated because a serious current leakage appeared at high voltage range. This is presumably because a trace amount of electrically conductive nature is present even after post-ammonolysis of nitrogen-deficient oxynitride ceramics. [4] Highly-insulating oxynitride samples are desired to elucidate the occurrence of polarization phase alternation by making it possible to apply high electrical field to the samples.

In other works, compressively strained SrTaO$_2$N, LaTiO$_2$N, and Sr$_{1-x}$La$_x$Ta$_{1-x}$Ti$_x$O$_2$N ($x \approx 0.01$) thin films deposited on oxide perovskite crystal substrates also showed ferroelectric behaviors [5-8] below the bias voltage range of ±8 V in the PFM measurements. They were observed only in very small domains with the sizes of $10 - 100$ nm and a serious current leakage occurred during the measurements as in the cases of the abovementioned ceramic specimens. [4] The origin of the ferroelectricity in such inhomogeneous films is considered to be the compressive stress induced by the crystalline lattice size mismatches between the films and oxide substrates. [5-8] Most importantly,

investigation on the electrical properties in self-standing single crystals is necessary to elucidate the emergence of ferroeletricity in oxynitride perovskites.

In the present chapter, piezoresponse measurements were conducted on BaTaO$_2$N crystals using a piezoresponse force microscope (PFM). Ferroelectric behavior of BaTaO$_2$N is discussed with a concept of polar nano regions (PNRs) in the crystal structure of BaTaO$_2$N. Additionally, Raman spectroscopic measurements were conducted on a BaTaO$_2$N microcrystal to discuss its crystal structure in relation to the piezoresponse and the presence of non-centrosymmetric regions discussed in **Chapter 2**.

6-2. Experimental

Sample preparation

Reddish BaTaO$_2$N microcrystals were grown as mentioned in **Chapter 5**. Cubic crystals in size larger than 3 μm were obtained with 46 mol% BaCN$_2$, heating at 910 °C for 30 min, and subsequent cooling at 1.8 °C/h. The sample after cooling was washed in 1 M nitric acid to remove soluble impurities mainly BaCN$_2$ and an obvious square shape of reddish crystal was observed as shown in an inset of **Fig. 6-2**. The single phase of perovskite-type $Pm\bar{3}m$ was confirmed using powder XRD with Cu Kα radiation as in the profile shown in **Fig. 6-2**. Its lattice parameter of cubic perovskite $a = 0.41118(3)$ nm well

matches with the literature value (a = 0.41128 nm). [9]

Piezoresponse measurements were conducted on micron-scaled BaTaO$_2$N single crystals. Very recently, it has been pointed out that some false detections of piezoresponse may occur due to electrostatic force on the bared surfaces of dielectric samples as schematically depicted in **Fig. 6-3**. [10-12] In the present study, top electrodes were applied to the surfaces of the crystals to remove static electrons as shown in **Fig. 6-4 (a)**. The crystals after leaching in nitric acid were dispersed by sonication in ethanol (99.5%, FUJIFILM Wako Pure Chemical). The suspension was then dropped on an Au bottom electrode deposited by sputtering with a thickness of approximately 100 nm on a Cu plate. The Cu plate was then annealed at 500 °C for 5 h in nitrogen atmosphere to complete a contact between the Au film and the bottom of BaTaO$_2$N crystals. Top electrode was fabricated by sputtering Pt (JFC-1100E, JEOL) in a thickness of approximately 150 nm on the entire surface of the Cu plate. The surroundings of each BaTaO$_2$N crystal were grooved with focused ion beam (FIB, JIB-4600F/HKD, JEOL) of gallium to separate top and bottom electrodes, as depicted in the SEM images of **Figs. 6-4(b, c)**.
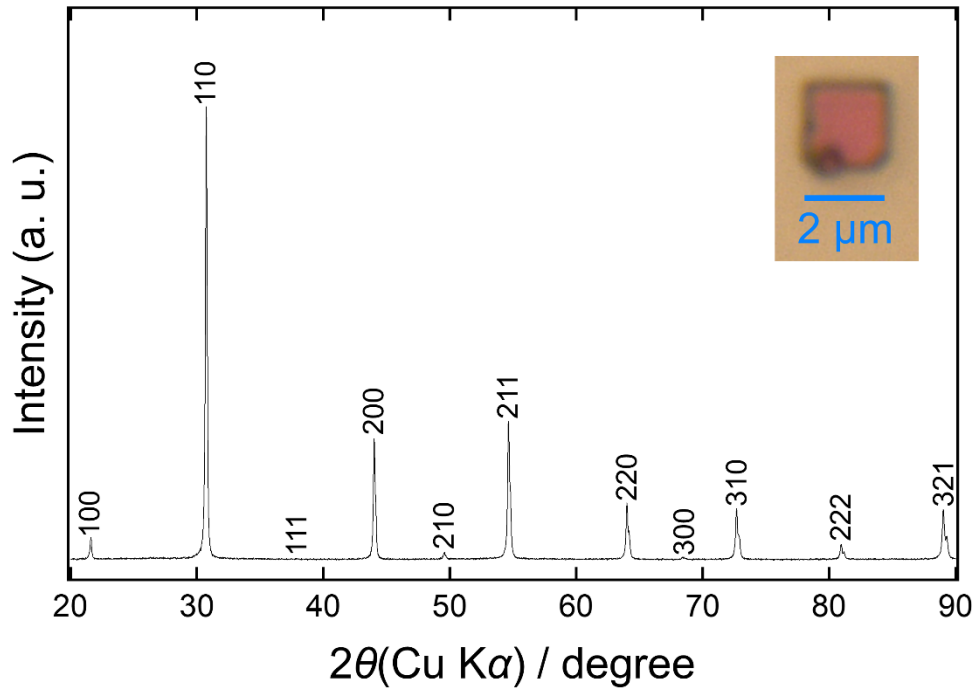
Fig. 6-2. Powder XRD pattern of $BaTaO_2N$ crystals prepared with 46 mol% $BaCN_2$, duration time at 910 °C for 30 min, and a cooling rate of 1.8 °C/h. The sample was leached in 1 M nitric acid. The inset is an optical image of a crystal grain. Its lattice parameter of cubic perovskite $a = 0.41118(3)$ nm well matches with the literature value ($a = 0.41128$ nm). [9]
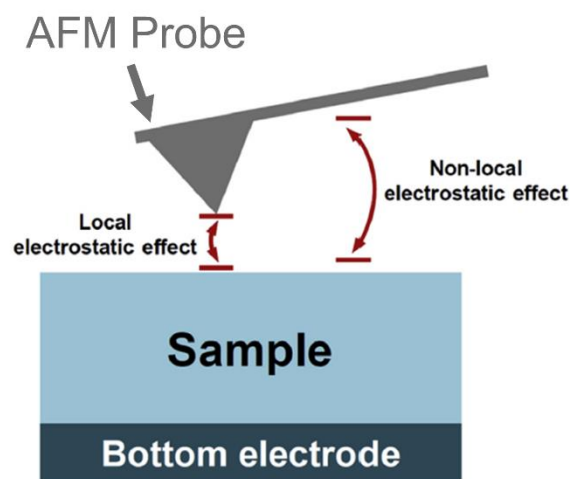

Fig. 6-3. A schematic image of the false detection of piezoresponse caused by electrostatic force on the surface of dielectric materials. [11]
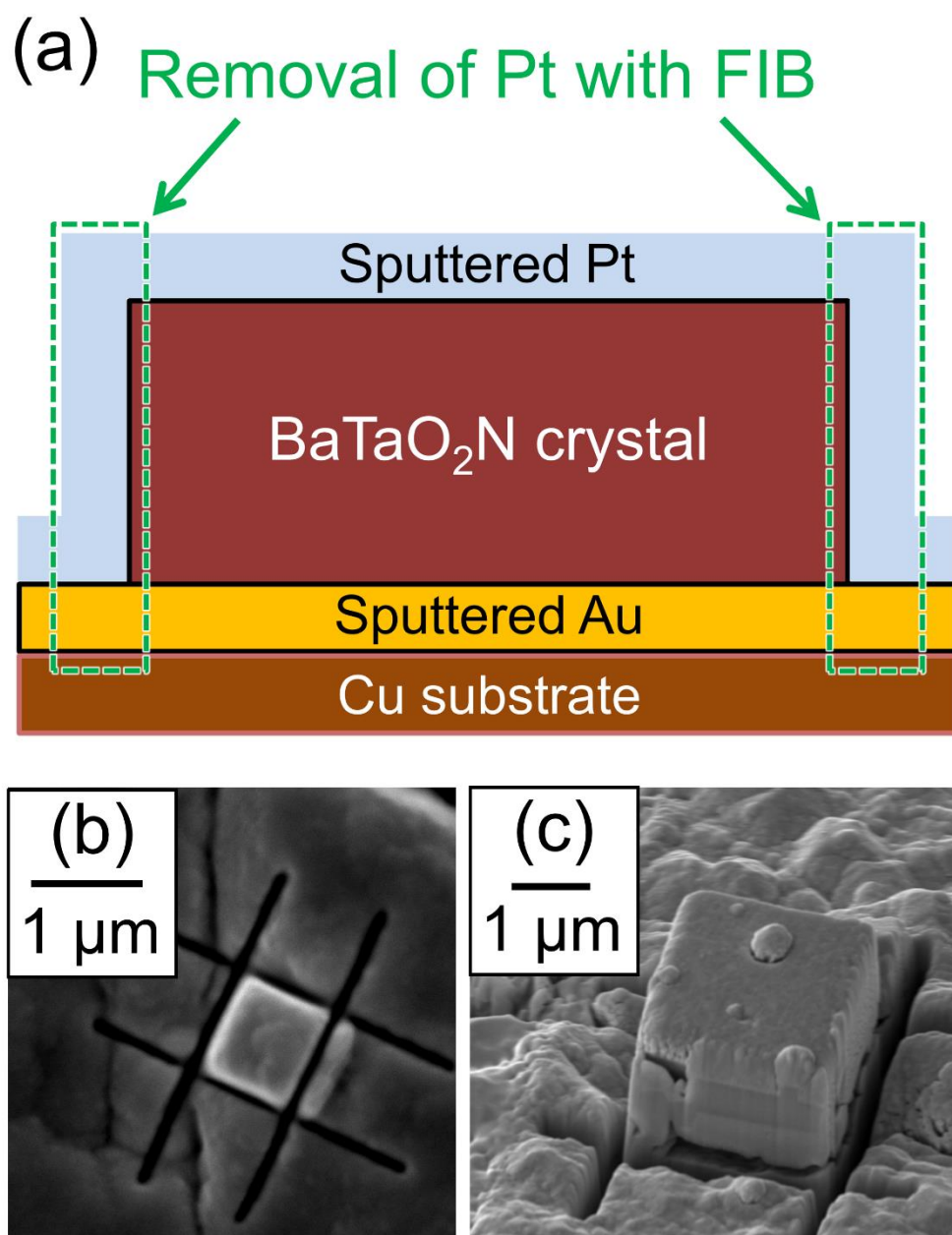
Fig. 6-4. (a) A schematic image of the processed BaTaO$_2$N sample and **(b,c)** SEM micrographs of the crystals after FIB grooving.

PFM measurements

The piezoelectricity of the $BaTaO_2N$ crystals was investigated using a PFM technique that is applicable to nano-sized areas in tiny samples. [1-3] Electrical voltage was applied to $BaTaO_2N$ crystals with electrodes on both sides as mentioned above. Switching spectroscopy piezoresponse force microscope with DART technique (SS-PFM, ASYLUM MFP-3D, Oxford Instruments) was employed in an electrical field bias of up to ±100 V through a silicon probe coated with Ir metal (ASYELEC-01) and a stiffness of 0.77 N/m. SS-PFM was measured in a temperature range of up to 120 °C. The maximum applied electric field was roughly estimated as 460 kV/cm.

Raman spectroscopy

Subsequently Raman spectroscopic measurements were conducted on a $BaTaO_2N$ crystal at room temperature. Nd:YAG laser beam with a wavelength of 514.5 nm and a diameter of 1 μm was irradiated on the surface of a $BaTaO_2N$ crystal with a size larger than 2 μm. The energy output was optimized to be less than 150 mW to avoid the decomposition of $BaTaO_2N$ during measurements. Measurements were conducted using monochromaters (Triple Monochromator, PDPX, Photon Design for ~200 cm^{-1} and Triple Monochromer, T64000, Jobin Yvon for ~800 cm^{-1}).

6-3. Results and discussion

Electrical short was avoided by forming an island capacitor structure, which was fabricated by the FIB grooving of a Pt deposited side-wall connected to the bottom Au electrode and copper substrate (see **Fig. 6-4**). A square region with dimensions of 2.5 × 2.0 μm^2 was found out in the AFM topographical image of a $BaTaO_2N$ single crystal covered with a Pt top electrode, as shown in **Fig. 6-5(a)**. An AC electrical voltage of $2V$p-p (peak to peak voltage) was subsequently applied to the present crystal at various temperatures. It was found that a much higher electrical voltage could be applied to the present highly-insulating crystals than the previous ceramic samples, which showed serious current leakage at voltages as low as 10 V as mentioned in **Chapter 3**. [4] Deformations were observed in the PFM measurements over the temperature range of 30 to 90 °C under an electrical voltage of less than 40 V, but there was no polarization switching over the voltage range applied. A PFM phase hysteresis loop and a PFM amplitude butterfly curve originating from the ferroelectricity were clearly observed at 120 °C in an applied electrical voltage of ±100 V (that corresponds to the approximate electrical field of ±460 kV/cm), as shown in **Fig. 6-5(b)** and **(c)**. The coercive field was estimated to be 250 kV/cm, according to the phase and amplitude signals, although a higher voltage was required to induce clear piezoresponse phase switching. In a

166

preliminary experiment on another crystal, polarization phase alternation was observed at high temperature (e.g. 100 °C), while no phase switching was detected in the same voltage range at 30 °C as shown in **Fig. 6-6**. This suggests that polarization phase in PNRs could be more easily altered by the assist of heat as in the cases of typical relaxor ferroelectrics like $Pb(Mg_{1/3}Nb_{2/3})O_3$. [13] The difference of coercive fields of the samples shown in **Figs. 6-5(b,c)** and **6-6(c)** may be due to the difference of the sizes and polarization directions of PNRs contained in the crystals.

Note that an electrostrictive effect was observed in the amplitude curve due to application of a very high voltage. Here, the polarization(P)-electric field(E) hysteresis loop should be measured; however, it is very difficult to execute for the following reasons; (1) enough charge could not be obtained using an island system because of the very small top electrode size, and (2) artificial charge from the air capacitor between the cantilever and top electrode might be included in the measurement. A reliable capacitance value could not be obtained due to the same reason with as that given in (1). Although we could not exactly measure the P-E hysteresis loop, clear polarization switching was obtained in this SS-PFM measurement, indicating that $BaTaO_2N$ single crystal is truly a ferroelectric material.

The observed ferroelectric polar phase alternation is consistent with the

presence of PNRs in BaTaO$_2$N, which has previously been suggested by many researchers as indicated by the favorability of *cis*-type anisotropic anion configurations and the formation of spontaneous polarization in oxynitride perovskites (**Fig. 6-7(a)**). [14-20] The nitrogen atoms form the *cis*-type configurations to consist the helical Ta-N chain motifs in the apical linkages to TaO$_4$N$_2$ octahedra. The PNRs in **Fig. 6-7(a)** are formed by the interaction between two kinds of helical Ta-N chain coil motifs; clockwise and anti-clockwise. These are present in the domain structures of PNRs even at room temperature, which is considered to be below the Burns temperature for this compound (**Fig. 6-7(b)**). [21] The concentration of these PNRs may be low, as suggested by the weak intensity of the SHG signal shown in **Fig. 2-1** in **Chapter 2**, probably because of the disordering between oxygen and nitrogen atoms at 3c site. Also, the presence of non-centrosymmetric *Pmc*2$_1$ phase discussed in **Chapter 2** is consistent with the present ferroelectric piezoresponse. The polar domain size gradually grows with increases in the applied electrical field bias, as summarized schematically in **Figs. 6-7(c)** and **(d)**. In the crystal in **Fig. 6-5**, the polarization was saturated above ±250 kV/cm in the applied electric field to show the clear ferroelectric piezoresponse. The present crystals were sufficiently insulating so as to allow the application of electrical fields as high as ±460 kV/cm, which is by far higher than the maximum values for ceramic samples reported in
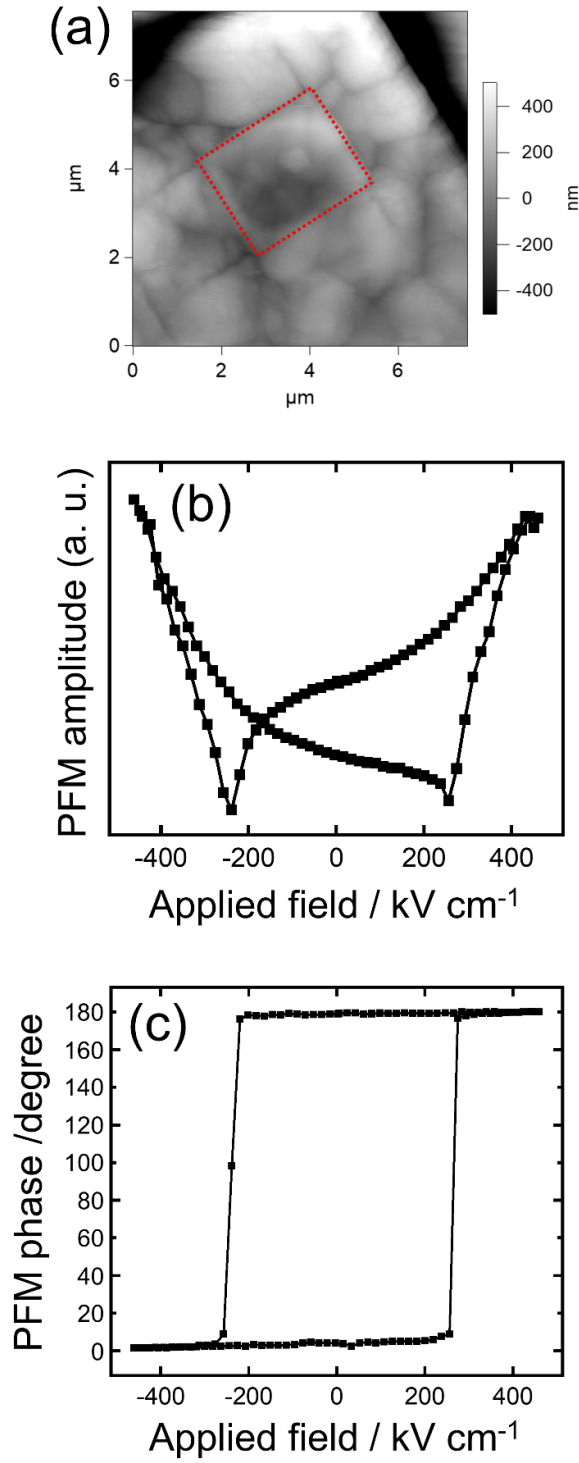
168

Fig. 6-5. (a) AFM topographical image of a BaTaO$_2$N crystal (indicated by the dotted red square), **(b)** piezoresponse amplitude curve obtained at 120 °C, and **(c)** its ferroelectric phase signal graph.
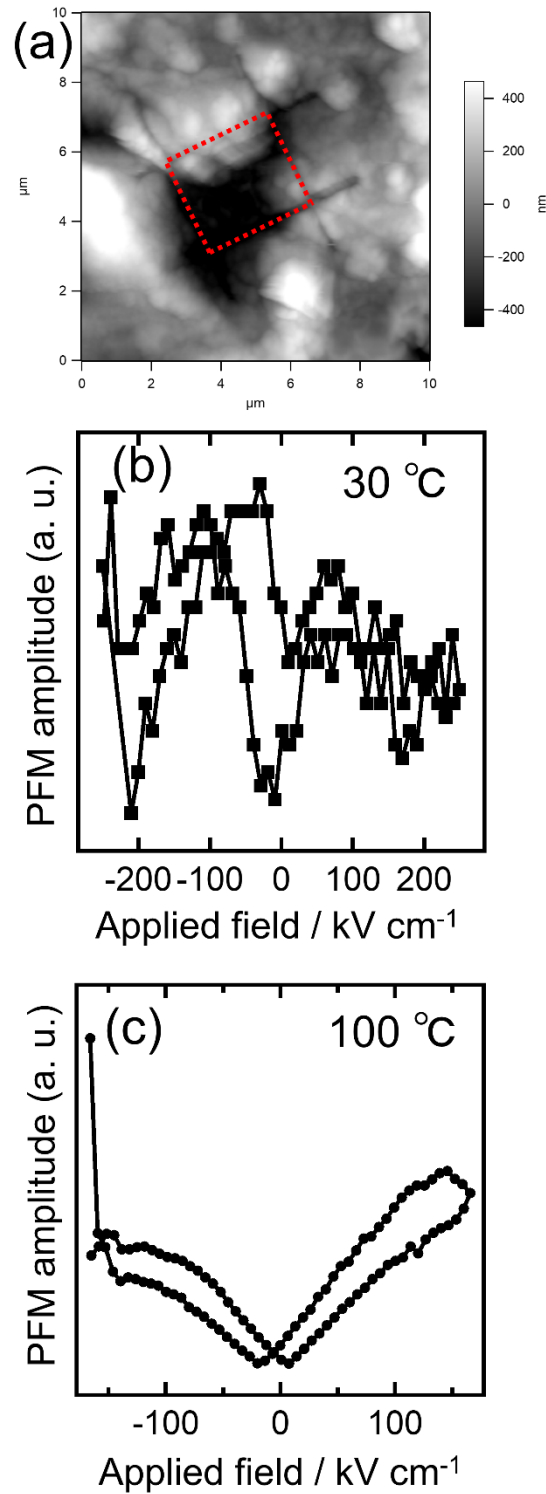
Fig. 6-6. (a) AFM topograph of a thin BaTaO$_2$N crystal after FIB grooving process (indicated by the dotted red square), its piezoresponse at **(b)** 30 °C, and **(c)** 100 °C.

Chapter 3 (up to approximately ± 10 V (= 12.5 kV/cm)). This characteristic enabled to saturate the polarization of $BaTaO_2N$ crystals to produce clear butterfly-like PFM signal.

Raman spectroscopy was performed on a $BaTaO_2N$ microcrystal depicted in an optical image of **Fig. 6-8(a)**. Raman spectra obtained on a $BaTaO_2N$ crystal is shown in **Fig. 6-8(b)**. It shows at least five Raman peaks. The profile appearance is completely different from the one of perovskite-type $SrTiO_3$ single crystal with a cubic $Pm\overline{3}m$ space group [23], which has only three Raman tensor elements. [24] This may suggest the presence of more distorted structure in $BaTaO_2N$. More detail regarding the Raman spectra is now under investigation.

The situation that non-centrosymmetric regions are contained over the "average" centrosymmetric phase matches with the model of relaxor ferroelectrics with spontaneous polarization originating from PNRs. Here, the presence of PNRs was demonstrated by PFM measurements on $BaTaO_2N$ single crystals.
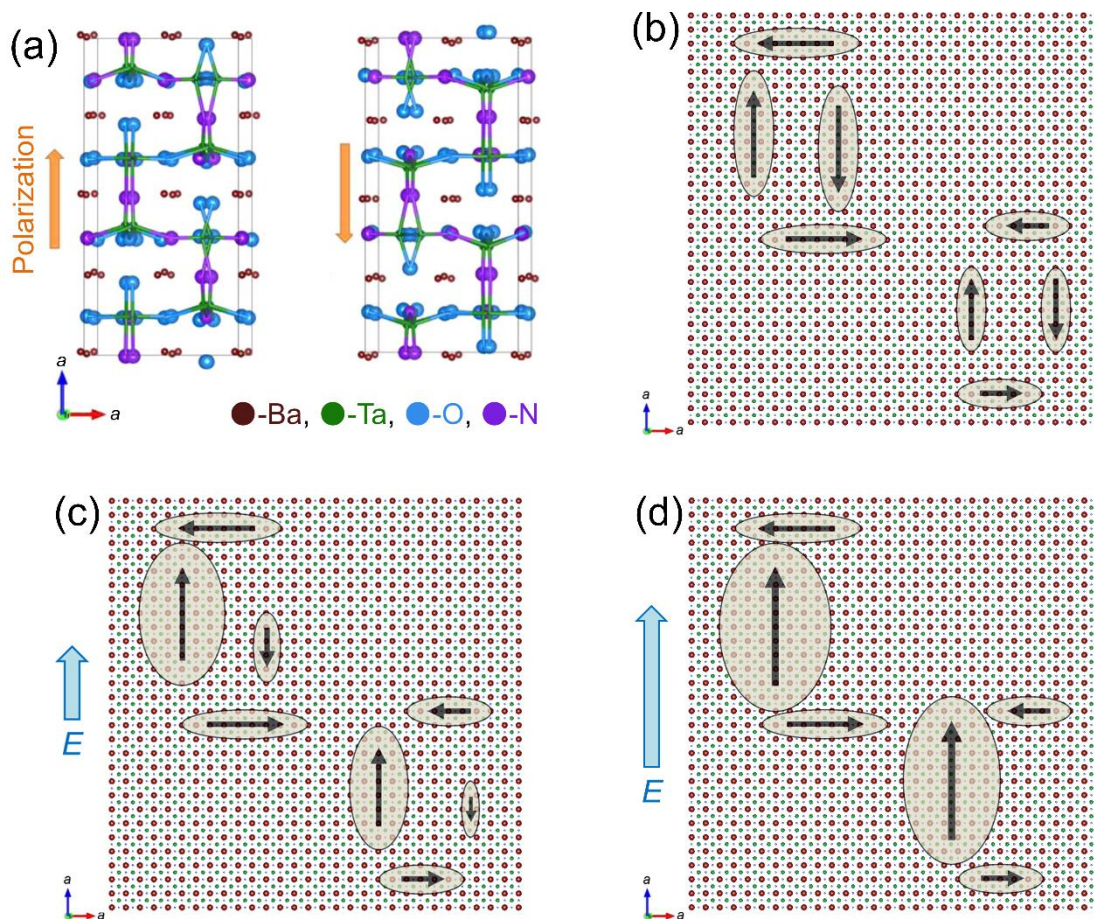
Fig. 6-7. (a) Two sets of polar nano regions in the crystal structure of BaTaO₂N with *cis*-type anion ordering, as simulated by molecular dynamics calculations. [17] Brown, green, blue, and purple spheres indicate Ba, Ta, O, and N, respectively. **(b)** Polar nano regions present in the average $Pm\bar{3}m$ cubic crystal lattice in which most of the oxygen and nitrogen atoms are randomly distributed at $3c$ sites. **(c)** Polar nano regions growing along the applied electric field. **(d)** Polarization saturated at applied bias higher than coercive field. Structural models were drawn using the VESTA software package. [22]
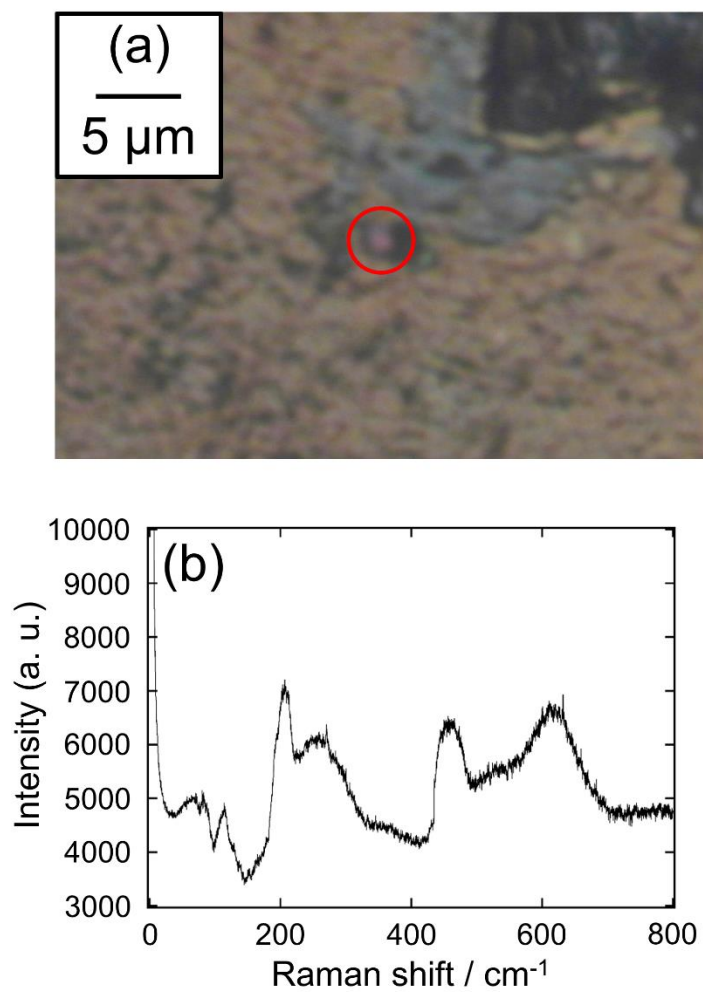
Fig. 6-8. (a) Optical micrograph of a $BaTaO_2N$ microcrystal (indicated with a red circle, approximately 2 μm in size), **(b)** Raman spectroscopic profile of a $BaTaO_2N$ crystal.

6-4. Conclusion

Highly-insulating $BaTaO_2N$ microcrystals showed clear ferroelectric piezoresponses, indicating the presence of spontaneous polarizations that could be switched by applying an external electrical field at high temperature about 100 °C. The polarization switching without electrical leakage was observed in self-standing oxynitride perovskite solid samples for the first time. This finding clearly confirmed the presence of the ferroelectricity in this material, as a result of the formation of polar nano regions by anisotropic anion configurations without compositional inhomogeneity.

The polar nano regions are believed to be generated in association with polar crystal structural units introduced by the *cis*-type TaO_4N_2 octahedra linkages. This hypothesis was supported by SHG measurement and the Rietveld fitting of a powder neutron diffraction profile using a polar structure model of *Pmc*2_1. The results of the PFM measurements are consistent with these structural studies. Furthermore, Raman spectroscopic studies on the $BaTaO_2N$ crystal provided a possibility of the presence of some distorted structure other than *Pm*$\overline{3}$*m* space group.

Chapter 6 References

[1] D. A. Bonnell, S. V. Kalinin, A. L. Kholkin, A. Gruverman, "Piezoresponse Force

Microscopy: A Window into Electromechanical Behavior at the Nanoscale", *MRS Bulletin*, 2009, 34, 648–657.

[2] E. Soergel, "Piezoresponse force microscopy (PFM)", *J. Phys. D: Appl. Phys.*, 2011, 44, 464003.

[3] A. Gruverman, M. Alexe, D. Meier, "Piezoresponse force microscopy and nanoferroic phenomena", *Nat. Commun.*, 2019, 10, 1661.

[4] S. Kikkawa, S. -K. Sun, Y. Masubuchi, Y. Nagamine, T. Shibahara, "Ferroelectric response induced by *cis*-type anion ordering in $SrTaO_2N$ oxynitride perovskite", *Chem. Mater.*, 2016, 28, 1312–1317.

[5] D. Oka, Y. Hirose, T. Fukumura, K. Sasa, S. Ishii, H. Matsuzaki, Y. Sato, Y. Ikuhara, T. Hasegawa, "Possible ferroelectricity in perovskite oxynitride $SrTaO_2N$ epitaxial thin films", *Sci. Rep.*, 2014, 4, 4987.

[6] C. L. Paven, R. Benzerga, A. Ferri, D. Fasquelle, V. Laur, L. L. Gendre, F. Marlec, F. Tessier, F. Cheviré, R. Desfeux, S. Saitzek, X. Castel, A. Sharaiha, "Ferroelectric and dielectric study of strontium tantalum based perovskite oxynitride films deposited by reactive rf magnetron sputtering", *Mat. Res. Bull.*, 2017, 96, 126–132.

[7] F. Marlec, C. L. Paven, L. L. Gendre, R. Benzerga, F. Cheviré, F. Tessier, F. Gam, A. Sharaiha, "Deposition and dielectric study as function of thickness of perovskite oxynitride $SrTaO_2N$ thin films elaborated by reactive sputtering", *Surf. Coat. Technol.*, 2017, 324, 607–613.

[8] N. Vonrüti, U. Aschauer, "Anion Order and Spontaneous Polarization in $LaTiO_2N$ Oxynitride Thin Films", *Phys. Rev. Lett.*, 2018, 120, 046001.

[9] F. Pors, R. Marchand, Y. Laurent, "Structural study of $BaTaO_2N$ and $BaNbO_2N$ oxynitrided perovskites", *Mat. Res. Bull.*, 1988, 23, 1447–1450.

[10] J. Seidel, L. W. Martin, Q. He, Q. Zhan, Y. -H. Chu, A. Rother, M. E. Hawkridge, P. Maksymovych, P. Yu, M. Gajek, N. Balke, S. V. Kalinin, S. Gemming, F. Wang, G. Catalan, J. F. Scott, N. A. Spaldin, J. Orestein, R. Ramesh, "Conduction at domain walls in oxide multiferroics", *Nat. Mater.*, 2009, 8, 229–234.

[11] D. Seol, B. Kim, Y. Kim, "Non-piezoelectric effects in piezoresonse force microscopy", *Curr. Appl. Phys.*, 2017, 17, 661–674.

[12] N. Faraji, Z. Yan, J. Seidel, "Electrical conduction at domain walls in lead titanate ($PbTiO_3$) single crystals", *Appl. Phys. Lett.*, 2017, 110, 213108.

[13] D. Fu, H. Taniguchi, M. Itoh, S. Koshihara, N. Yamamoto, S. Mori, "Relaxor $Pb(Mg_{1/3}Nb_{2/3})O_3$: A Ferroelectric with Multiple Inhomogeneities", *Phys. Rev. Lett.*, 2009, 103, 207601.

[14] K. Page, M. Stoltzfus, Y. -I, Kim, T. Proffen, P. M. Woodward, A. K. Cheetham, R.

Seshadri, "Local atomic ordering in BaTaO$_2$N studied by neutron pair distribution function analysis and density function theory", *Chem. Mater.*, 2007, 19, 4037–4042.

[15] R. L. Withers, Y. Liu, P. M. Woodward, Y. I. Kim, "Structurally frustrated polar nanoregions in BaTaO$_2$N and the relationship between its high dielectric permittivity and that of BaTiO$_3$", *App. Phys. Lett.*, 2008, 92, 102907.

[16] B. Ravel, Y. I. Kim, P. M. Woodward, C. M. Fang, "Role of local disorder in the dielectric response of BaTaO$_2$N", *Phys. Rev. B*, 2006, 73, 184121.

[17] Y. Hinuma, H. Moriwake, Y. Zhang, T. Motohashi, S. Kikkawa, I. Tanaka, "First principles study on relaxor-type ferroelectric behavior without chemical inhomogeneity in BaTaO$_2$N and SrTaO$_2$N", *Chem. Mater.*, 2012, 24, 4343–4349.

[18] H. Wolff, R. Dronskowski, "First-Principles and Mollecular-Dynamics Study of Structure and Bonding in Perovskite-Type Oxynitrides ABO$_2$N (A = Ca, Sr, Ba; B = Ta, Nb)", *J. Comput. Chem.*, 2008, 29, 2260–2267.

[19] M. Yang, J. Oro-Sole, J. A. Rodgers, A. Jorge, A. Fuertes, J. P. Attfield, "Anion order in perovskite oxynitrides", 2011, *Nat. Chem.*, 3, 47–52.

[20] Y. -R. Zhang, T. Motohashi, Y. Masubuchi and S. Kikkawa, "Local anionic ordering and anisotropic displacement in dielectric perovskite SrTaO$_2$N", *J. Cer. Soc. Jpn.*, 2011, 119, 581–586.

[21] G. Burns, F. H. Dacol, "Crystalline ferroelectrics with glassy polarization behavior", *Phys. Rev. B*, 2008, 28, 2527–2530.

[22] K. Momma, F. Izumi, "VESTA 3 for three-dimensional visualization of crystal, volumetric and morphology data", *J. Appl. Crystallogr.*, 2011, 44, 1272–1276.

[23] V. I. Merkulov, J. R. Fox, H. –C. Li, W. Si, A. A. Sirenkol, X.X. Xi, "Metal-oxide bilayer Raman scattering in SrTiO$_3$ thin films" *Appl. Phys. Lett.*, 1998, 72, 3291–3293.

[24] S. J. Cyvin, J. E. Rauch, J. C. Decius, "Theory of Hyper-Raman Effects (Nonlinear Inelastic Light Scattering): Selection Rules and Depolarization Ratios for the Second-Order Polarizability", *J. Chem. Phys.*, 1965, 43, 4083–4095.

Chapter 7

Spark Plasma Sintering of BaTaO$_2$N Using a Molten BaCN$_2$ Additive

7-1. Introduction

In the last chapter, an evidence of the ferroelectricity of BaTaO$_2$N crystals grown in a BaCN$_2$ melt was presented. The melting point of BaCN$_2$ (910 °C) is slightly lower than the nitrogen releasing temperature of BaTaO$_2$N (920 °C), and stoichiometric, excellently insulating microcrystals were obtained. Further target is the fabrication of polycrystalline BaTaO$_2$N ceramics without nitrogen loss during sintering to simplify the sample fabrication process and improve electrical insulation in the products compared to the high temperature sintering reported in **Chapter 3**.

As mentioned in **Chapters 4** and **5**, the melt of BaCN$_2$ dissolves oxynitride perovskites and cubic oxynitride crystals precipitate. The BaCN$_2$ melt may be also useful to fabricate polycrystalline BaTaO$_2$N ceramics without nitrogen loss in the sintering process. It will wet the BaTaO$_2$N powder surface assisting the solute diffusion through the BaCN$_2$ solvent similarly to the case of liquid phase sintering. Spark plasma sintering (SPS) method will be beneficial in rapid sintering under pressure to avoid the thermal decomposition of BaTaO$_2$N. [1-5]. SPS is a densification technique on a pressurized powder compact assisted by external electrical field. Rapid heating can be performed

177

through the Joule heating of conductive die and punches. [1-5] A typical equipment setup is depicted in **Fig. 7-1**.

In the present chapter, $BaTaO_2N$ powder was sintered with a $BaCN_2$ additive under a uniaxial mechanical pressure applied with an SPS equipment. The crystalline phases, microstructure, and electrical properties of the ceramic products were studied, to find out a possibility to obtain dielectric $BaTaO_2N$ ceramics without the partial loss of nitrogen from the perovskite-type crystalline lattice.
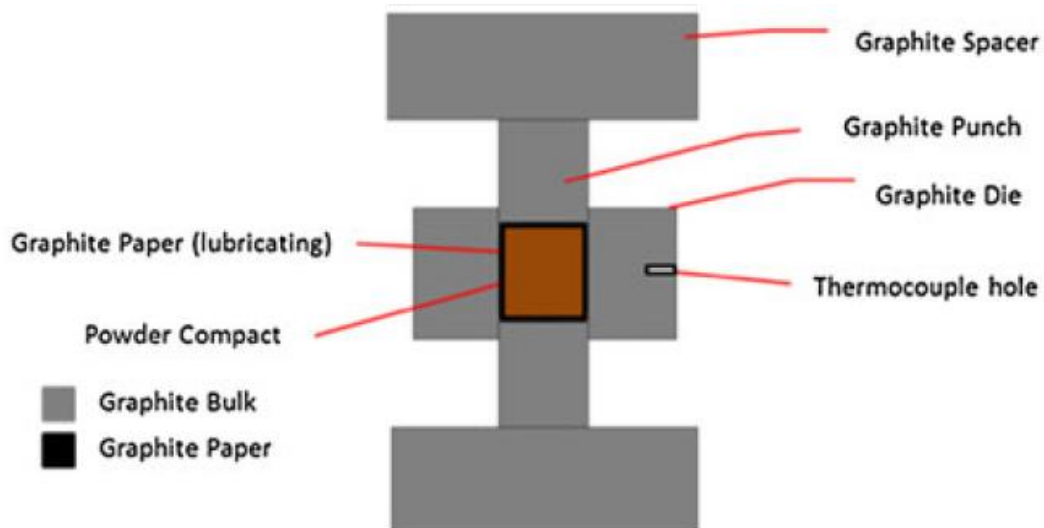
Fig. 7-1. An example of a tool setup of SPS furnace. [1]

7-2. Experimental

Sintering of BaTaO₂N powder

BaTaO$_2$N and BaCN$_2$ powders were obtained by the ammonolysis of either powder mixture of BaCO$_3$ and Ta$_2$O$_5$ or BaCO$_3$, as mentioned in **Chapters 2** and **4**. The prepared BaTaO$_2$N powder of 0.8 g was then mixed with 0 – 20 wt% of BaCN$_2$ in a planetary ball milling system using zirconia balls with a diameter of 5 mm and 5 mL of hexane (> 95%, FUJIFILM Wako Pure Chemical) as a dispersion medium in a 45 mL zirconia pot. Mixing was performed at a rotation rate of 570 rpm for 10 min. This procedure was performed in nitrogen atmosphere to avoid the oxidation and hydrolysis of BaCN$_2$. The milled powder mixture was sintered into 1 mm-thick disc shape with a diameter of 1 cm using an SPS equipment (Spark plasma sintering system LABOX-1575, SinterLand Inc.). A schematic image of its sintering procedure is illustrated in **Fig. 7-2**. Approximately 500 mg of BaTaO$_2$N/BaCN$_2$ powder mixture was sandwiched between additive-free BaTaO$_2$N powder parts of about 150 mg. They were inserted into carbon punches and die covered with graphite sheet to avoid BaCN$_2$ contamination. The sample chamber was evacuated and then nitrogen gas (> 99.999%) was introduced up to 0.08 MPa prior to heating. Uniaxial mechanical pressure was applied to 100 MPa on the samples and the chamber was heated to approximately 900 °C at a rate of 200 °C/min and

kept for the desired time of 1 – 10 min. Mechanical pressure was applied over the entire

SPS process. First of all, the temperature of the carbon die was investigated. The

temperature of carbon die slightly exceeded the melting point of $BaCN_2$ (910 °C) with a

temperature setting of 900 °C. When only $BaCN_2$ powder was heated with the same

temperature setting, it completely melted even in a short keeping time of a few minutes,

confirming the presence of $BaCN_2$ melt for liquid phase sintering during heating. The

sample preparation conditions and properties of the ceramic products are summarized in

Table 7-1.

Characterization of the ceramic products

The sintered ceramics were polished with a 1000-grit sandpaper to remove

excess $BaTaO_2N$ powder adhered to the ceramic surface. Their bulk densities were

calculated with geometric method and relative density (RD) values were obtained

assuming the products are pure $BaTaO_2N$ (theoretical density = 8.69 g cm^{-3}). [6] The

amount of $BaCN_2$ in the ceramic products cannot be quantified because of a partial loss

of molten $BaCN_2$ by its vaporization and partial decomposition at high temperature.

Moreover, molten $BaCN_2$ reacts with the surface of $BaTaO_2N$ grains to form Ba-rich

Ruddlesden-Popper type oxynitride perovskites. The Archimedes method was not

applicable in the present case because the ceramics in the present work contain a number

of open pores, which makes it impossible to obtain the precise density values of the ceramic products. The crystalline phases of the polished ceramic surfaces were identified with XRD with Cu Kα radiation over the 2θ range of $20 - 80°$ with a scanning rate and step size of $10°$/min and $0.02°$. XRD profile fitting and the phase proportion calculation were conducted with a Rietveld software package (RIETAN-FP). [7]

Chemical compositions of the ceramic products were studied using XRF for the molar ratios of Ba/Ta and combustion O/N analyzer for oxygen/nitrogen contents. Carbon contents were ignored for its small weight ratios less than the detection limit of CHN combustion analyzer (< 0.3 wt%, MICROCORDER JM10, J-Science Lab.).

A thin slice of the ceramic product obtained with 5 wt% $BaCN_2$, keeping at 900 °C for 1 min, and uniaxial pressure of 70 MPa was prepared using FIB (SMI 3050SE, Hitachi High-Technologies). The microstructure and composition of the specimen in a thickness less than 100 nm was observed with a TEM (Titan3 G2 60-300, FEI Company) with Cs-spherical aberration corrector and EDS.

Electrical properties of the ceramic product sintered with 5 wt% $BaCN_2$, at 70 MPa, and duration at 900 °C for 3 min (sample (e) in **Table 7-1**) were investigated with an impedance analyzer (4294A, Agilent Technologies, Inc.) through the electrodes applied by sputtering Pt (JFC-1100E, JEOL) in a thickness larger than 100 nm.

Measurements were conducted at room temperature over a frequency range of $10^2 - 10^6$ Hz.

7-3. Results and discussion

Effects of BaCN₂ additive and applied mechanical pressure

Preliminary SPS processing was applied on BaTaO$_2$N powder with or without BaCN$_2$ additive to elucidate the effect of BaCN$_2$ on its densification. All the samples were heated at approximately 900 °C, which corresponds to the melting point of BaCN$_2$. No densification was observed on the additive-free BaTaO$_2$N powder. The powder mixtures containing some amount of BaCN$_2$ rapidly densified to the RDs larger than 66.5%. The RD values are plotted against BaCN$_2$ amount for the products SPSed for 5min or less in **Fig. 7-3(a)**. BaCN$_2$ additive is obviously effective for rapid densification compared with the high temperature sintering mentioned in **Chapter 3**.

In **Fig. 7-3**, samples sintered with 7 wt% BaCN$_2$ tend to show slightly lower RD values. This may be because BaTaO$_2$N solid particles are sometimes separated by molten BaCN$_2$, which disturbs the densification of BaTaO$_2$N. As for the case of the addition of 5 wt% BaCN$_2$, the distance between solid particles is appropriate due to the absence of too much amount of molten BaCN$_2$, to make the ceramic products a little

Table 7-1. Sintering conditions and BaTaO$_2$N ceramic products fabricated by SPS method.

Name	Dwell time at 900 °C	Pressure	BaCN$_2$ amount	RD	Nitrogen content (compared with the sample before sintering)	Note
a	1 min	30 MPa	5wt%	68.7%	Stoichiometric	Red, insulating
b	1 min	70 MPa	5wt%	80.7%	Stoichiometric	Red, insulating
c	3 min	30 MPa	7wt%	66.5%	Stoichiometric	Red, insulating
d	3 min	30 MPa	10wt%	70.5%	Stoichiometric	Red, insulating
e	3 min	70 MPa	5wt%	79.8%	Stoichiometric	Red, insulating
f	3 min	70 MPa	7wt%	72.1%	Stoichiometric	Red, insulating
g	3 min	70 MPa	10wt%	83.0%	Stoichiometric	Red, insulating
h	3 min	100 MPa	5wt%	80.1%	Stoichiometric	Red, insulating
i	3 min	100 MPa	7wt%	76.9%	Stoichiometric	Red, insulating
j	3 min	100 MPa	10wt%	82.4%	Stoichiometric	Red, insulating
k	5 min	70 MPa	5wt%	84.1%	Stoichiometric	Red, insulating
l	10 min	30 MPa	3wt%	78.6%	-	Black, conductive
m	10 min	30 MPa	5wt%	97.6%	-	Black, conductive
n	10 min	30 MPa	10wt%	98.0%	Deficient in 9.5%	Black, conductive
o	10 min	30 MPa	20wt%	Broken	-	Black, conductive
p	10 min	70 MPa	10wt%	78.0%	-	Brown, conductive
q	60 min	30 MPa	5wt%	93.5%	Deficient in 11.0%	Black, conductive
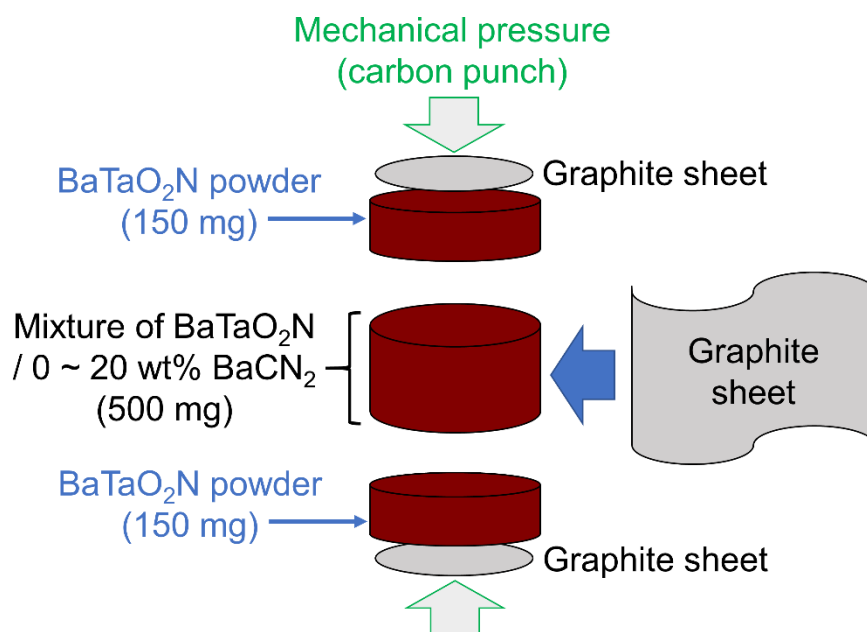
Fig. 7-2. A schematic image of the sample setup for the present SPS procedure.
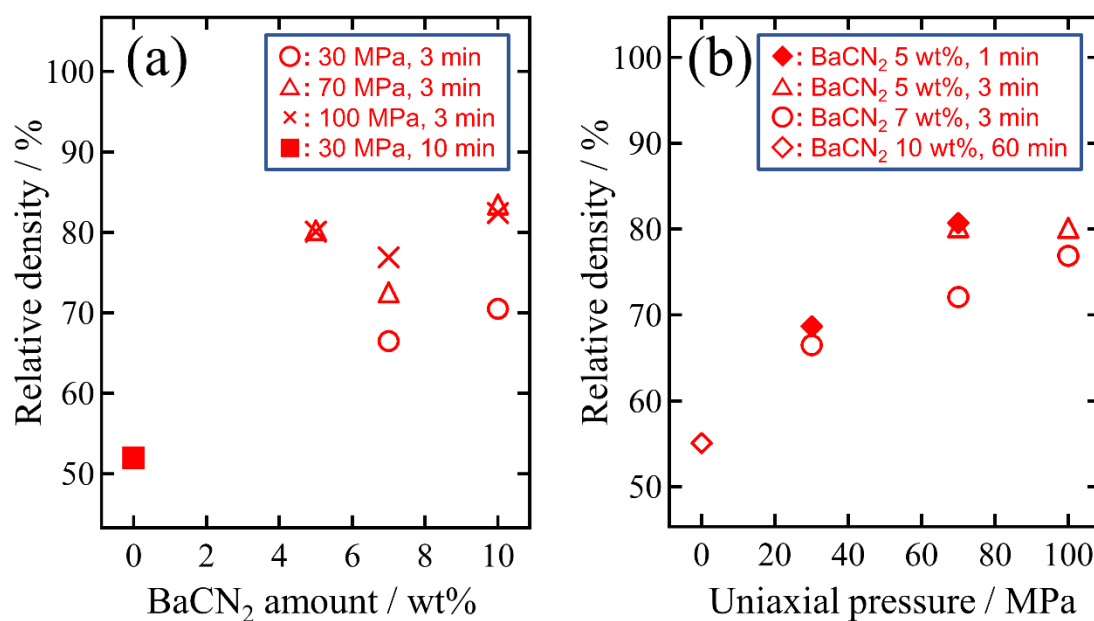
Fig. 7-3. Relative densities of BaTaO$_2$N ceramics as functions of **(a)** the amount of BaCN$_2$ additive and **(b)** applied uniaxial pressure. The plotted data are for the samples with stoichiometric nitrogen contents.

denser. However, the reason why the 10 wt% samples became slightly denser than 7 wt% ceramics still remains unclear. Some penetration of molten $BaCN_2$ into the $BaTaO_2N$ powder beds was detected by analyzing Ba/Ta molar ratios of the powder beds using XRF. Excess amount of Ba (by more than 5 mol%) compared with Ta was contained. This, evacuation of $BaCN_2$ out of the main $BaTaO_2N/BaCN_2$ mixture, was significant when large amount of $BaCN_2$ additive of 7 wt% or more was mixed before heating and high pressure was applied. So, the effect of $BaCN_2$ amount in the initial mixtures on RD values cannot be compared quantitatively because a rich amount of molten $BaCN_2$ was not utilized for densification effectively. Too much amount of $BaCN_2$ (20 wt%, sample (o) in **Table 7-1**) resulted in ceramic products broken into tiny particles. The preferable $BaCN_2$ amount was less than 10 wt% to keep the disk shape of the products.

The effect of the applied mechanical pressure was studied as shown in **Fig. 7-3(b)**. The powder mixture of $BaTaO_2N$ with 10 wt% $BaCN_2$ did not densify at all in a heating without mechanical pressure at 900 °C for 1 h. The RD values increased to exceed 66.5% under the pressures higher than 30 MPa. Molten $BaCN_2$ was infiltrated between the $BaTaO_2N$ particles to wet their particle surface in the squeezing under mechanical pressure. The RD values did not increase furthermore above 70 MPa. This may be because $BaCN_2$ melt was squeezed out from the main $BaTaO_2N/BaCN_2$ sample body to the upper

and lower $BaTaO_2N$ powder beds under the high pressures.

$BaTaO_2N$ powder was densified with 5 wt% $BaCN_2$ by changing heating duration at approximately 900 °C. Photographs of $BaTaO_2N$ ceramics sintered for 3 min (sample (e)) and 60 min (sample (q)) are shown in **Fig. 7-4**. Red, and electrically insulating $BaTaO_2N$ ceramics were obtained in the duration shorter than 5 min as shown in **Fig. 7-4(a)**. The heating for longer than 5 min resulted in black semiconductors (**Fig. 7-4(b)**). A part of nitrogen was lost from the oxynitride perovskite by a reducing atmosphere produced in the presence of graphite sheets, die, and punches. Keeping duration time up to 5 min is appropriate to obtain $BaTaO_2N$ dielectric ceramics. Maximum RD value of the stoichiometric $BaTaO_2N$ ceramics was 84.1% in sample (k).

Sintering mechanism of $BaTaO_2N$ with $BaCN_2$

XRD profile was observed on the polished $BaTaO_2N$ ceramic surface sintered with 5 wt% $BaCN_2$ at 70 MPa and 900 °C for 5 min (sample (k)). The main crystalline phase is perovskite-type $BaTaO_2N$ with a lattice parameter $a = 0.411009(11)$ nm, which well matches with the literature value ($a = 0.41128$ nm). [6] A Ba-rich Ruddlesden-Popper type Ba_2TaO_3N appeared as a side phase about 5.8 wt% as shown in **Fig. 7-5**. Similar Ba_2TaO_3N impurity was observed in the crystal growth study on $BaTaO_2N$ in a reaction between $BaTaO_2N$ and $BaCN_2$. The excess oxygen in Ba_2TaO_3N impurity is supplied

from the adsorbed oxygen and/or moisture on the surfaces of $BaTaO_2N/BaCN_2$ mixture and the inside of SPS equipment. The presence of Ba_2TaO_3N impurity suggests that the present densification of $BaTaO_2N$ is not a simple liquid phase sintering. The material diffusion in densification is assisted by chemical reactions in which the perovskite dissolves and recrystallizes in molten $BaCN_2$ as it was between the $BaTaO_2N$ main phase and the BaO intermediate formed in a partial oxidation of $BaCN_2$ as mentioned in **Chapter 5**.

TEM blight field image was obtained on a thin specimen of the ceramics (sample (b) with RD = 80.7%) as depicted in **Fig. 7-6(a)**. Compared with the primary particle size of as-prepared $BaTaO_2N$ powder shown in **Fig. 7-6(d)** and **(e)**, a slight grain growth seems to have occurred during SPS processes, although it is not significant. Grains in ceramics are connected via thin boundaries and some voids are observed in its microstructure. Large voids in the approximate grain size are present probably because the packing of starting powder was insufficient. Further increase in RD values will be attained by improving starting $BaTaO_2N$ powder contacts by changing their particle sizes. EDS compositional analyses were conducted on several parts across a grain boundary in a high magnification high-angle annular dark field scanning TEM (HAADF-STEM) image (**Fig. 7-6(b)**). Molar ratios of Ba/Ta at each point were normalized with the value
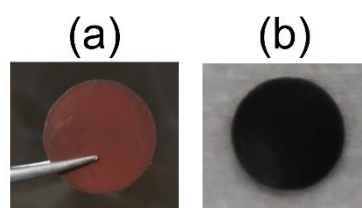
Fig. 7-4. Photographs of BaTaO$_2$N ceramics (e) and (q) sintered with 5 wt% BaCN$_2$ additive 900 °C for **(a)** 3 min and **(b)** 60 min, respectively.
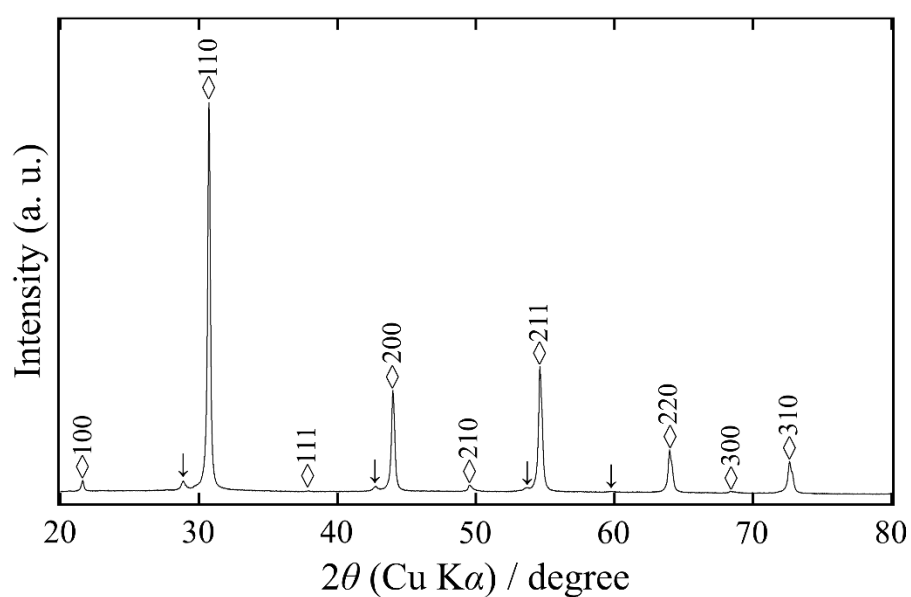
Fig. 7-5. XRD pattern of the polished ceramic surface sintered with 5 wt% BaCN$_2$, at 70 MPa and 900 °C for 5 min (sample (k), RD = 84.1%). Diamonds and arrows indicate BaTaO$_2$N (ICSD 202763) and Ba$_2$TaO$_3$N (JCPDS 47-1388), respectively.
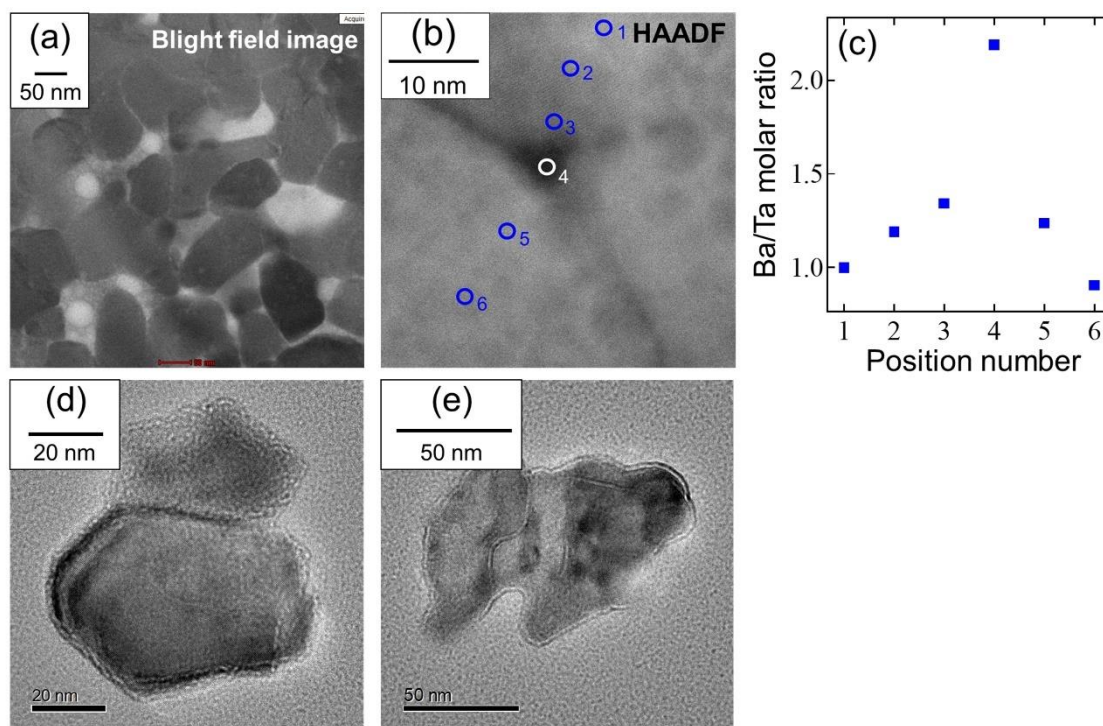
Fig. 7-6. (a) TEM blight field and **(b)** HAADF-STEM images of a BaTaO$_2$N ceramic specimen with RD = 80.7% (sample (b)). **(c)** is Ba/Ta molar rations observed with EDS at several points in **(b)**. **(d)** and **(e)** are blight field images of as-prepared BaTaO$_2$N particles obtained by ammonolysis.

of the **point 1** (an interior of BaTaO$_2$N grain). The proportion of Ba gradually increased

from the grain interior to the exterior and the maximum value was at the triple point (**point

4** in **Fig. 7-6(b)**). The molten BaCN$_2$ spread out into the narrow grain boundary area by a

mechanical pressure and wetted the surface of BaTaO$_2$N grains. The BaCN$_2$ flux is

concentrated in triple points of the solidified BaTaO$_2$N grains. Sintering process in the

present study can be explained as schematically illustrated in **Fig. 7-7**. The surface of

BaTaO$_2$N grains is wetted by molten BaCN$_2$ to cover the boundaries as shown in **Fig. 7-

7(a)**. BaTaO$_2$N grains are then dissolved to the molten BaCN$_2$ and precipitates forming

Ba-rich side phases like Ba$_2$TaO$_3$N on the surface region of the grains. This step is

accompanied by a slight grain growth to connect BaTaO$_2$N particles as in **Fig. 7-7(b)**.

Finally, each BaTaO$_2$N grain is connected via thin boundaries of BaTaO$_2$N itself

containing a small amount of Ba-rich components mainly the residual BaCN$_2$ and

Ba$_2$TaO$_3$N. Sometimes such Ba-rich constituents are confined in the triple points of the

grown BaTaO$_2$N grains as shown in **Fig. 7-7(c)**.

SEM micrographs were observed on the as-prepared BaTaO$_2$N powder and the

fracture surfaces of sintered BaTaO$_2$N ceramics (sample (k)). Grains are well connected

each other in the ceramics, but neither significant necking between the grains nor apparent

grain growth are observed, despite its high RD = 84.1% as depicted in **Fig. 7-8**. All the

grains were just bonded at their boundaries formed through the molten $BaCN_2$. Grain growth is not well enough generally in a short duration of SPS process even in sintering of oxide inorganic materials. [2]

Electrical properties of BaTaO$_2$N ceramics

The electrical properties were studied on the BaTaO$_2$N ceramic sample (e) at room temperature over a frequency range of $10^2 - 10^6$ Hz. The sample was relatively dense (RD = 79.8%) among the present products and well-characterized as mentioned above. Complex impedance plots shown in **Fig. 7-9(a)** indicate only a small part of a giant arc, suggesting the present ceramics is an insulator, even without post-ammonolysis. **Fig. 7-9(b)** shows its relative dielectric constants ε_r of $320 - 650$ and dielectric loss tanδ of $0.04 - 0.19$. These values are comparable with the best ones reported on the post-annealed ceramics with RD = 73.0% sintered at high temperature ($\varepsilon_r = 290 - 620$ and tanδ = $0.04 - 0.4$). Partial nitrogen loss was eliminated in the present sintering at 900 °C. The temperature is below the nitrogen releasing from BaTaO$_2$N and around the melting point of $BaCN_2$. In summary, fabrication of BaTaO$_2$N ceramics maintaining its nitrogen contents and electrically insulating properties was achieved by relatively low temperature sintering at 900 °C, without post-ammonolysis process required after the high temperature sintering accompanied by a partial decomposition.
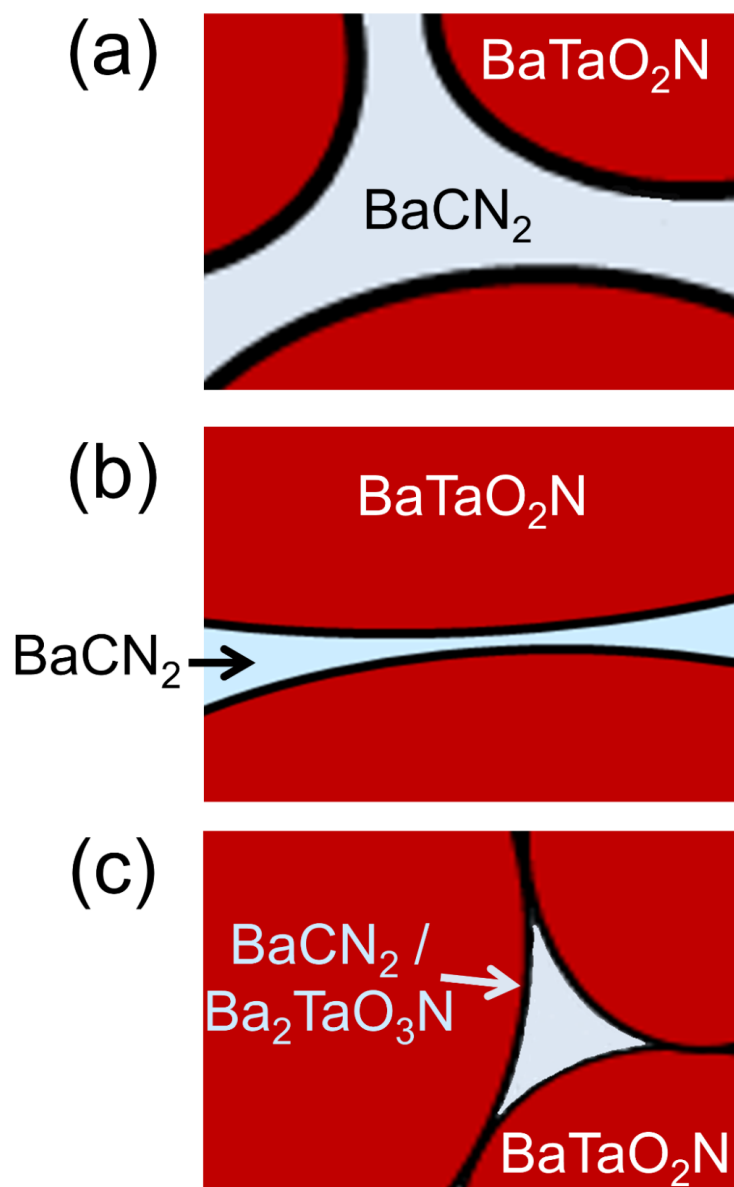
Fig. 7-7. Schematic images of the sintering process of $BaTaO_2N$ involving molten $BaCN_2$. **(a)** wetting on the surface of $BaTaO_2N$ grains, **(b)** grain growth in the dissolution and precipitation of $BaTaO_2N$ via molten $BaCN_2$ flux, and **(c)** formation of a triple point after the sintering.
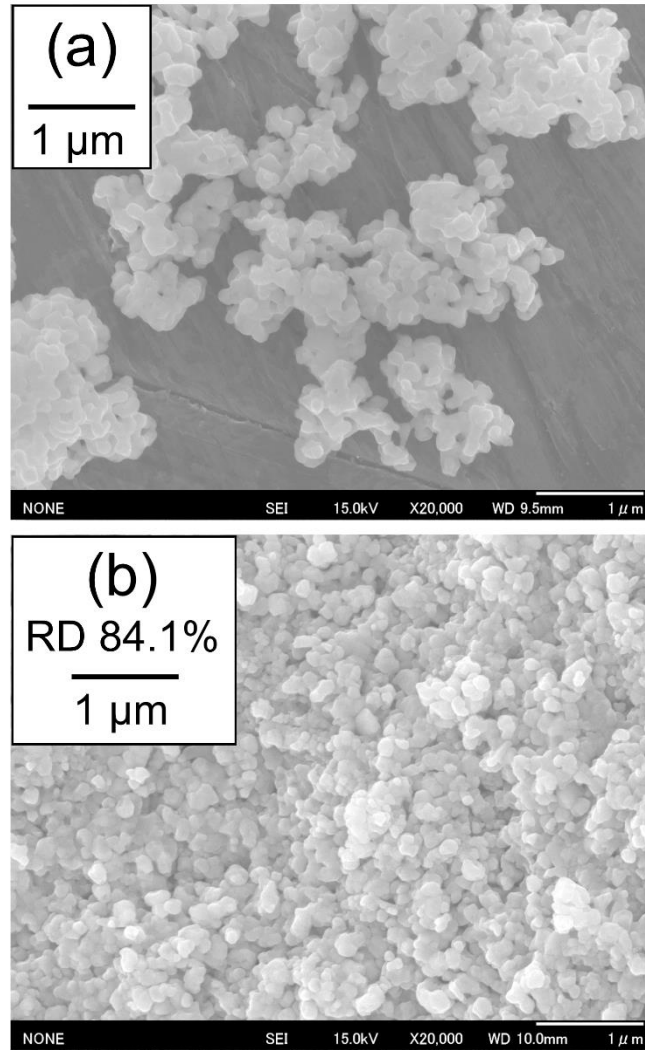
Fig. 7-8. SEM micrographs of **(a)** as-prepared BaTaO$_2$N powder and **(b)** fracture surface of a BaTaO$_2$N ceramics with RD = 84.1% sintered with 5 wt% BaCN$_2$, 70 MPa mechanical pressure, and 5 min keeping at 900 °C (sample (k)).
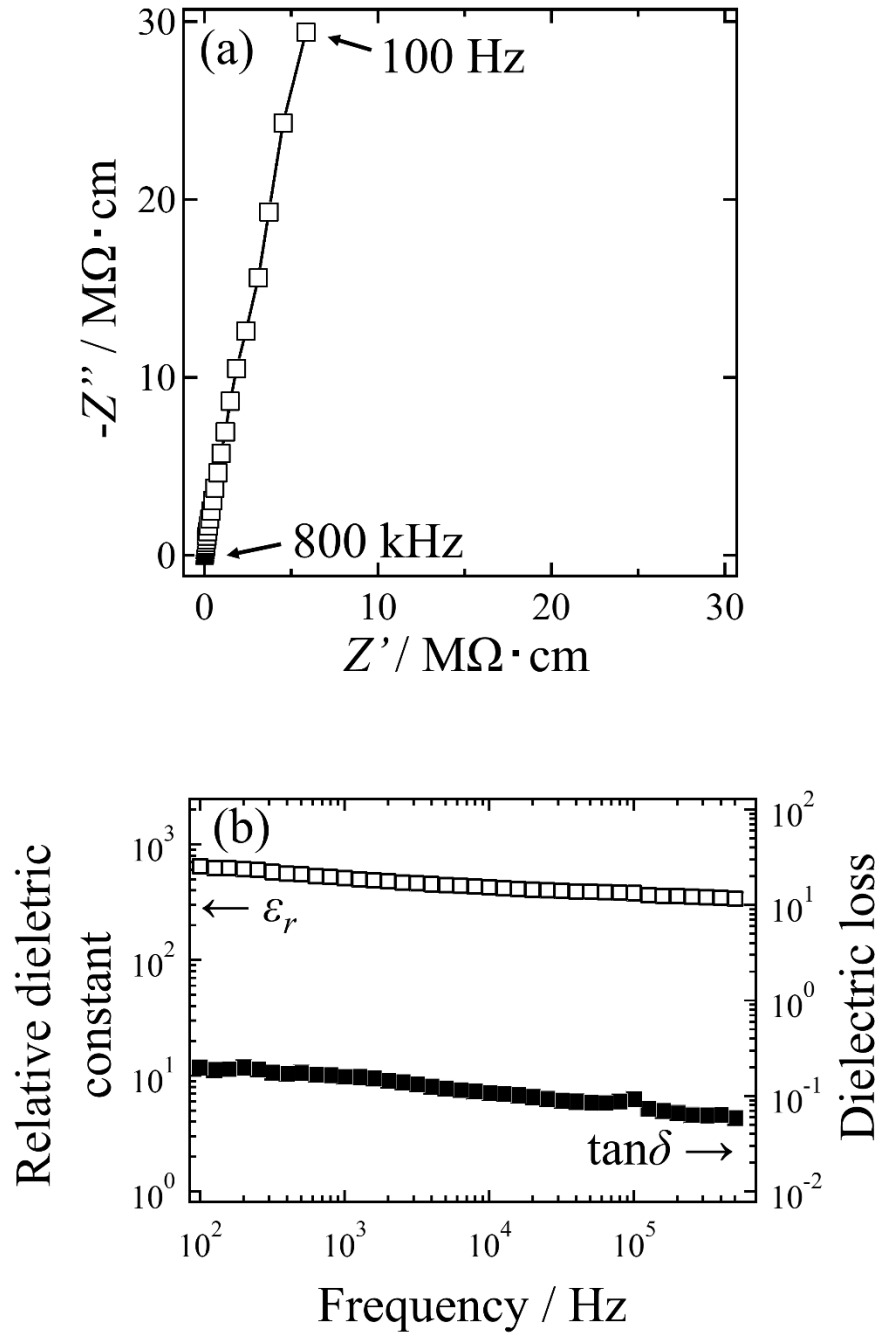
Fig. 7-9. (a) Cole-Cole complex impedance plots and **(b)** dielectric properties as functions of frequency of a BaTaO$_2$N ceramics (sample (e), RD = 79.8%) at room temperature.

7-4. Conclusion

BaTaO$_2$N powder was sintered at the lowest temperature (approximately 900 °C) among its sintering studies, using a BaCN$_2$ additive under mechanical pressure in SPS equipment to avoide a partial nitrogen loss. BaTaO$_2$N grains were bonded through their dissolution and precipitation around their surface in BaCN$_2$ melt. Minor reaction product, Ba-rich compound such as Ruddlesden-Popper type Ba$_2$TaO$_3$N, was present in grain boundaries and triple points of the ceramics. Rapid heating and cooling process in an SPS furnace were also effective to avoid a partial nitrogen loss from BaTaO$_2$N. The maximum relative density of 84.1% was observed on the BaTaO$_2$N ceramics maintaining the original nitrogen content. Both relative dielectric constants of 320 – 650 and losses of 0.04 – 0.19 in the present ceramics with RD = 79.8% are comparable with the previously reported values for post-ammonolysis product with RD = 73.0% sintered at high temperature (ε_r = 290 – 620, tanδ = 0.04 – 0.4). The present sintering process at around the melting point of BaCN$_2$ additive will be useful to fabricate commercially available relaxor ferroelectric ceramics based on BaTaO$_2$N oxynitride.

Chapter 7 References

[1] W. Li, E. Olevski, J. McKittrick, A. L. Maximenko, R. M. German, "Densification mechanisms of spark plasma sintering: multi-step pressure dilatometry", *J. Mater. Sci.*,

2012, 47, 7036–7046.

[2] R. Chaim, G. Chevallier, A. Weidel, C. Estournés, "Grain growth during spark plasma and flash sintering of ceramic nanoparticles: a review", *J. Mater. Sci.*, 2018, 53, 3087–3105.

[3] M. J. Li, L. M. Zhang, Q. Shen, T. Li, M. Q. Yu, "Microstructure and properties of spark plasma sintered AlN ceramics", *J. Mater. Sci.*, 2006, 41, 7934–7938.

[4] D. Salamon, Z. Shen, P. Pavol Sajgalik, "Rapid formation of α-sialon during spark plasma sintering: Its origin and implications", *J. Eur. Ceram. Soc.*, 2007, 27, 2541–2547.

[5] Z. Shen, M. Nygren, "Microstructural Prototyping of Ceramics by Kinetic Engineering: Applications of Spark Plasma Sintering", *Chem. Rec.*, 2005, 5, 173–184.

[6] F. Pors, R. Marchand, Y. Laurent, "Structural study of $BaTaO_2N$ and $BaNbO_2N$ oxynitrided perovskites", *Mat. Res. Bull.*, 1988, 23, 1447–1450.

[7] F. Izumi, K. Momma, "Three-dimensional visualization in powder diffraction", *Solid State Phenom.*, 2007, 130, 15–20.

Chapter 8

Conclusion

This thesis is mainly focused on the development of sintering and crystal preparation procedures for perovskite-type $BaTaO_2N$ to elucidate the emergence of ferroelectricity in oxynitride perovskites.

The average crystal structure of $BaTaO_2N$ has been reported to be centrosymmetric $Pm\bar{3}m$ space group. Structural reinvestigation using SHG measurement and powder neutron diffraction profile fitting suggested that the real structure is non-centrosymmetric phase like $Pmc2_1$ forming PNRs, but most of the polar domains may be too small to be clearly detected in diffraction studies. Thermal decomposition and sintering behaviors of $BaTaO_2N$ are similar to those of $SrTaO_2N$. TG-MS studies on $BaTaO_2N$ disclosed that it releases a part of its nitrogen above 920 °C to form $BaTaO_2N_{0.85}$ semiconductor. Further decomposition behaviors are strongly affected by its atmosphere. Most of perovskite-type lattice of $BaTaO_2N_{0.85}$ was maintained above 1400 °C in nitrogen, whereas it completely decomposed to its component oxides and nitrides in helium. $BaTaO_2N$ powder mixed with a small amount of a $BaCO_3$ additive was sintered in nitrogen atmosphere above 1350 °C in a BN crucible and subsequent post-annealing in ammonia flow was necessary to recover stoichiometric nitrogen content and

electrical insulation. The completely post-annealed ceramics with RD = 73.0% showed relative dielectric constants of 620 at 10^2 Hz and 320 at 10^8 Hz, slightly higher than the values reported for $SrTaO_2N$. These values were not affected in the applied frequency and temperature up to 150 MHz and 150 °C, respectively. The dielectric loss was less than 0.1 at higher frequency range than 10 kHz and it was nearly independent of frequency and temperature. For dense $BaTaO_2N$ ceramics, a clear piezoresponse was observed at the applied voltages between ±4 – 7 V on the surface slice of dense $BaTaO_2N$ ceramics with RD > 90%, confirming the presence of spontaneous polarization in $BaTaO_2N$ as suggested in **Chapter 2**. However, a serious current leakage occurred during the measurements.

To find out appropriate fluxes for the sintering and crystal growth of $BaTaO_2N$, melting behaviors of a series of alkaline-earth metal carbodiimides were investigated by experimental and computational approaches. $CaCN_2$ and alpha-phase of $SrCN_2$ melted at 1340 and 1020 °C, respectively, and both of them rapidly decomposed to their metals and carbides releasing nitrogen. On the other side tetragonal $BaCN_2$ melts at 910 °C and its melt was maintained without decomposition. This tendency is consistent with the DFT calculation results on the Gibbs energies of their decomposition reactions. Low melting point of $BaCN_2$ is attributed to its small lattice enthalpy.

Micron-sized crystals of $Ba_{1-x}Sr_xTaO_2N$ (x = 0.04 – 0.23) oxynitride solid solutions and $BaTaO_2N$ were effectively grown up using $BaCN_2$ as a solvent at approximately 910 °C. For $Ba_{1-x}Sr_xTaO_2N$, a compositional gradient from Sr-rich interior to Ba-rich exterior was observed. On the other side homogeneous $BaTaO_2N$ crystals were obtained by using a powder mixture of $BaTaO_2N$ and $BaCN_2$ as the starting materials. Cubic $BaTaO_2N$ crystals were obtained through the formation of Ruddlesden-Popper type Ba-rich side phases as a skin layer of crystals. Hence, crystals of $BaTaO_2N$ did not grow by a simple dissolution and recrystallization. Crystal size reached 3.1 μm, which is enough for the piezoelectric measurements.

A clear ferroelectric piezoresponse with a coercivity of 50 – 60 V ($\approx$ 250 kV/cm) of micron-sized $BaTaO_2N$ crystals was investigated using the PFM technique. $BaTaO_2N$ crystals showed by far higher electrical insulation than the post-annealed ceramics fabricated by high temperature sintering. This enabled to apply high electrical voltage enough to saturate its polarization. Polarization phase alternation was observed at high temperature of 100 °C, while no polarization switching was observed at 30 °C in the same voltage range. This is consistent with the temperature dependence of coercive field values of ferroelectrics. In summary, this research is the first demonstration of the ferroelectric polar phase alternation of excellently insulating oxynitride crystals. Its

ferroelectricity can be explained by the formation of polar nano regions originate from anisotropic anion configurations.

Sintering of BaTaO$_2$N at approximately 900 °C, which is below its nitrogen release temperature, was also tried using a BaCN$_2$ additive in a spark plasma sintering furnace. Both the presence of molten BaCN$_2$ and uniaxial pressure were effective to achieve densification of the ceramic products. Densification of the powder mixture of BaTaO$_2$N and BaCN$_2$ proceeded by dissolution and precipitation via BaCN$_2$ flux and a chemical reaction to form Ba$_2$TaO$_3$N. The ceramic product with a RD = 79.8% showed insulating behaviors and its dielectric properties are consistent with those of the post-annealed BaTaO$_2$N ceramics sintered at 1400 °C.

Further research target of this category of oxynitrides will be the crystal growth of oxynitrides to the size larger than several hundred micrometers and sintering of their fully-densified ceramics. These will be achieved by controlling the loss of molten fluxes and oxynitride particle morphologies. Such dense samples will enable to obtain a clear *P-E* ferroelectric hysteresis loops and reliable dielectric constant values. The author hopes this thesis will be a key for the future scientific researches and industrial applications of non-oxide solid state materials especially oxynitrides.

Acknowledgements

Finally, I'd like to express my highest appreciation to my family for their generous supports. Without them, it was impossible for me to insist on my research to the end.

Publications

Original papers for the present thesis

1. A. Hosono, S. -K. Sun, Y. Masubuchi, S. Kikkawa, "Additive sintering and post-ammonolysis of dielectric $BaTaO_2N$ oxynitride perovskite", *J. Eur. Ceram. Soc.*, 2016, 36, 3341–3345.

2. A. Hosono, Y. Masubuchi, T. Endo, S. Kikkawa, "Molten $BaCN_2$ for the sintering and crystal growth of dielectric oxynitride perovskites $Sr_{1-x}Ba_xTaO_2N$ ($x = 0.04 – 0.23$)", *Dalton Trans.*, 2017, 46, 16837–16844.

3. A. Hosono, Y. Masubuchi, Y. Nagamine, T. Shibahara, S. Kikkawa, "Piezoresponse and microstructure of $BaTaO_2N$ ceramics", *J. Eur. Ceram. Soc.*, 2018, 38, 3478–3482.

4. A. Hosono, R. P. Stoffel, Y. Masubuchi, R. Dronskowski, S. Kikkawa, "Melting Behavior of Alkaline-Earth Metal Carbodiimides and Their Thermochemistry from First-Principles", *Inorg. Chem.*, 2019, 58, 8938–8942.

5. A. Hosono, Y. Masubuchi, S. Yasui, M. Takesada, T. Endo, M. Higuchi, M. Itoh, S. Kikkawa, "Ferroelectric $BaTaO_2N$ Crystals Grown in a $BaCN_2$ Flux", *Inorg. Chem.*, 2019, 58, 16752–16760.

6. A. Hosono, M. Inoguchi, Y. Masubuchi, K. Murayama, M. Iha, M. Higuchi, S. Kikkawa, "Spark Plasma Sintering of Dielectric $BaTaO_2N$ close to the Melting Point of the $BaCN_2$ Additive", *J. Eur. Ceram. Soc.*, 2020, 40, 2317–2322.

Other papers

1. A. Hosono, Y. Masubuchi, S. Kikkawa, "Sintering behavior of dielectric $SrTaO_2N$ under high pressure of nitrogen", *Ceram. Int.*, 2017, 43, 2737–2742.

2. S. Kikkawa, A. Hosono, Y. Masubuchi, "Remarkable effects of local structure in tantalum and niobium oxynitrides", *Prog. Solid State Chem.*, 2018, 51, 71–80.

3. Y. Masubuchi, S. Nishitani, A. Hosono, Y. Kitagawa, J. Ueda, S. Tanabe, H. Yamane, M. Higuchi, and S. Kikkawa, "Red-emission over a wide range of wavelengths at

various temperatures from tetragonal $BaCN_2$:Eu^{2+}", *J. Mater. Chem. C*, 2018, 6, 6370–6377.

4. H. Yamane, R. Yagi, <u>A. Hosono</u>, Y. Masubuchi, "Synthesis, crystal structure and properties of a quaternary oxide with a new structure type, $BiGaTi_4O_{11}$", *Acta Cryst.*, 2019, C75, 702–706.

Presentations
Presentations on the achievements related to the present thesis

1. <u>A. Hosono</u>, Y. Masubuchi, S. Kikkawa, "Sintering of perovskite-type $SrTaO_2N$ using $SrCN_2$", CSJ Chemical Festival, Tokyo, Japan (October 2015).

2. <u>A. Hosono</u>, Y. Masubuchi, T. Motohashi, S. Kikkawa, "Sintering of $SrTaO_2N$ oxynitride perovskite by using $SrCN_2$ sintering aid", The 2015 International Chemical Congress of Pacific Basin Societies (PACIFICHEM 2015), Honolulu, USA (December 2015).

3. Y. Masubuchi, <u>A. Hosono</u>, S. -K. Sun, D. Chen, S. Kikkawa, "Thermal stability and densification of perovskite type dielectric oxynitrides, ATaO$_2$N (A = Sr, Ba)", The 13th International Conference on Ceramic Processing Science (ICCPS-13), Nara, Japan (May 2016).

4. <u>A. Hosono</u>, Y. Masubuchi, S. Kikkawa, "Sintering and dielectricity of $BaTaO_2N$ perovskite oxynitride" Annual Meeting of the Chemical Society of Japan 2016, Hokkaido Branch, Muroran, Japan (July 2016).

5. <u>A. Hosono</u>, Y. Masubuchi, S. Kikkawa, "Additive sintering and post-annealing of dielectric $BaTaO_2N$ oxynitride perovskite", The 18th International Symposium on Eco-materials Processing and Design (ISEPD2017), Naha, Japan (February 2017).

6. Y. Masubuchi, D. Habu, S. -K. Sun, <u>A. Hosono</u>, S. Kikkawa, "Crystal structure and dielectric property of perovskite-type oxynitrides", The 18th International Symposium on Eco-materials Processing and Design (ISEPD2017), Naha, Japan (February 2017).

7. <u>A. Hosono</u>, Y. Masubuchi, Y. Nagamine, T. Shibahara, S. Kikkawa, "Thermal stability and dielectricity of perovskite oxynitride $BaTaO_2N$", Annual Meeting of the Ceramic Society of Japan 2017, Tokyo, Japan (March 2017).

8. <u>A. Hosono</u>, Y. Masubuchi, S. Kikkawa, "Flux Growth of $Sr_{1-x}Ba_xTaO_2N$ ($x = 0.05 \sim 0.25$) Oxynitride", The 9th International Symposium on Nitrides (ISNT2017), Sapporo, Japan (August 2017).

9. <u>A. Hosono</u>, Y. Masubuchi, M. Higuchi, S. Kikkawa, "Growth of perovskite-type oxynitride $BaTaO_2N$ small crystals in $BaCN_2$ melt", Annual Meeting of the Ceramic Society of Japan, Tokyo, Japan (March 2019).

10. <u>A. Hosono</u>, M. Inoguchi, Y. Masubuchi, K. Murayama, M. Iha, M. Higuchi, S. Kikkawa, "Spark Plasma Sintering of Dielectric $BaTaO_2N$ Using Molten $BaCN_2$ Additive", The 13th Pacific Rim Conference of Ceramic Societies (PACRIM13), Ginowan, Japan (October 2019).

11. <u>A. Hosono</u>, Y. Masubuchi, S. Yasui, M. Takesada, M. Higuchi, M. Itoh, S. Kikkawa, "Preparation of ferroelectric $BaTaO_2N$ perovskite microcrystals", Japan Society of Applied Physics Spring Meeting 2020, Tokyo, Japan (March 2020).

Other presentations
1. <u>A. Hosono</u>, Y. Masubuchi, S. Kikkawa, "The effect of hot isostatic pressing on the sintering behavior of dielectric $SrTaO_2N$", Annual Meeting of the Ceramic Society of Japan, Tohoku and Hokkaido Branch 2016, Sapporo, Japan (October 2016).

2. <u>A. Hosono</u>, Y. Masubuchi, M. Higuchi, S. Kikkawa, "Preparation of $BaTaO_2N$ crystals using $BaCN_2$ melt", Annual Meeting of the Ceramic Society of Japan 2018, Sendai, Japan (March 2018).

3. R. Yagi, T. Yamada, H. Yamane, <u>A. Hosono</u>, Y. Masubuchi, "Synthesis, crystal structure and properties of novel compounds $BiGaTi_4O_{11}$ and $(Bi_{1-x}Ga_x)_{2-\delta}Ti_2O_{7-3\delta/2}$", Annual Meeting of the Ceramic Society of Japan, Touhoku and Hokkaido Branch 2018, Koriyama, Japan (November 2018).